Synthesis And Study Of Physical Properties Of Binary Oxide Nanostructures, Thin Films And Devices

Thesis submitted for the degree of

Doctor of Philosophy (Science)

In

Nanoscience and Nanotechnology

By

Samik Roy Moulik

Centre for Research in Nanoscience and Nanotechnology

University of Calcutta

September 2018

..........................To my parents

Acknowledgement

*It has been a long wonderful journey for the past six years at this prestigious institute "**S. N. Bose National Centre for Basic Sciences**", Kolkata, India, named after the world-famous scientist and National Professor **S. N. Bose Sir**. At the end of this journey, it is always cherishing to recollect those old memories and thank all of them who are part of this journey and helped me directly or indirectly to complete this dissertation. Though pages will fall short to express my sincere gratitude to all my near and dear ones, I would like to mention some of those people, without acknowledging them this dissertation will remain unaccomplished.*

*First and foremost, I owe my sincere respect and gratitude to my supervisor **Dr. Barnali Ghosh (Saha)** for her unparalleled guidance, inspiration, and motivation throughout the entire span of my research work. I found myself very fortunate as I work under her supervision who not only gave me complete freedom to explore science on my own way and but also stood by my side for fruitful suggestions to overcome the odds as and when I approached her. Her efforts, determination, support helped me to, sustain under difficult situations and learn how to take care of small tiny things for completion of this dissertation.*

*I express my deep and sincere gratitude to **Prof. A. K. Raychaudhuri** for his versatile in-depth knowledge about science, the way of learning and untiring enthusiasm which helped me a lot to complete this research dissertation. He always inspires us to become a knowledgeable person instead of an informative one.*

I wish to express my sincere thanks to Prof. Kalyan Mandal, Prof, P. K. Mukhopadhyay and others for providing me an easy way to learn physics as well as the experimental science during Ph.D. coursework. I would like to thank Dr. Manik Pradhan and Mr. Abhijit Maity for providing me an opportunity to learn and utilize high precision laser spectroscopy tools of their lab as a part of my research work.

TEM analysis of this thesis work was not possible without the active involvement of Ankita di (Dr. Ankita Ghatak). My collaboration with her started with discussing some TEM results which finally converted into some concrete and crucial part of this thesis. Her enthusiasm towards research work always motivated me to carry out my research work.

Mr. Prabir Basu Thakur) for his initiative about regarding my Ph.D. enrollment. Special thanks to Nirmal Sir (Mr. Nirmal Chakraborty) from ICON Analytical for his unconditional support and motivation to finish this dissertation. I always cherish the moments I have spent with Rahul da, Arindam da, Debashish da, Sohom da, Dipankar from ICON in this span for their support and help whenever I am in need.

I feel fortunate to have good friends since my childhood and take this opportunity to recall few of those friends Rahul (Rahul Lasker) Shuddha (Dr. Shuddha Sankar Dasgupta), Kaustav (Kaustav Bose), Sudeshna (Dr. Sudeshna Bhattacharjya), who helped me a lot during this Ph.D. span. I still remember those discussions Shudhha and I had in 2011-12 before starting our Ph.D. journey and our strong determination and motivation afterward to till date made this dream successful. I will always remember our long conversations about copping our obstacles in reaching our goals over the phone, sittings thousands of miles apart, as an encouragement. Thanks to Kaustav, Sudeshna for doing the most boring job of proof checking of my thesis patiently managing time from your busy work schedule. I am also thankful to my childhood friend) for inspiring and motivating me to pursue the career in science.

I wish to express my sincere gratitude to all my respected teachers from my school days to till date. I am thankful to Arinban da (Mr. Anirban Paul) for teaching me Physics in my high school days and enriched me with his skills and passion for learning Physics. I am also thankful to Mr. Durgadas Sir and Soumendra Prasad Sir for enriching me with their knowledge during my school days. Without their support, inspiration, and guidance it was not possible for me to achieve my success.

Finally, most importantly, none of this would have been possible without the love, patience, support of my parents since I take my first breath in this world. They always stood beside me at all the ups and downs I faced till date. Their consideration and sacrifice during this entire Ph.D. work span are inexpressible. I owe this thesis to them.

Lastly, I thank God for making my journey so fascinating.......

Samik Roy Moulik
S. N. Bose National Centre for Basic Sciences,
Kolkata, India
September, 2018

List of Publication and Patent applications

List of Publication in peer-review journal

1. **Samik Roy Moulik,** Ankita Ghatak, Barnali Ghosh, *"Study of surface chemistry and microstructure of TiO_2 nanostructures on Pt(111)/Si wafer and FTO glass substrates: a comparative approach"*, **Surface Science 651, 175–181, 2016.***

2. **Samik Roy Moulik,** Sudeshna Samanta, Barnali Ghosh, *"Photoresponse in thin film of WO_3 grown by pulse laser deposition"*, **Appl. Phys. Lett. 104 (23), 232107, 2014.***

3. Ankita Ghatak, **Samik Roy Moulik**, Barnali Ghosh *"Pulsed laser assisted growth of aligned nanowires of WO_3: role of interface with substrate"*, **RSC Adv. 6, 31705–31716, 2016.***

4. **Samik Roy Moulik**, Abhijit Maity, Prosenjit Chakraborty, Manik Pradhan and Barnali Ghosh, *"Isotopic enrichment of CO_2 gas in WO_3 nanostructures enabled by physical processes studied using Cavity Enhanced Absorption Spectroscopy (CEAS)"*, **Submitted.***

List of Patent application (Indian)

1. **Samik Roy Moulik**, Abhijit Maity, Mithun Pal, Manik Pradhan and Barnali Ghosh *"Advancement in Methodology and System to Control Isotopic Fractionations in Carbon Containing Gases"*, **Indian Patent Filed No. 201731017087 dated: 16/05/2017*.**

Present thesis is based on publications marked with *****

List of Abbreviation

1D: One dimensional
PLD: Pulsed Laser Deposition
NWs: Nanowires
XRD: X-Ray Diffraction
E$_g$: Band gap
RF: Radio frequency: RF
QC: Quantum confinement
UV: Ultraviolet
FET: Field Effect Transistor
PC: Photocurrent
PPC: Persistent photo current
HS: Hollow sphere
SEM: Scanning Electron Microscope
FESEM: Field Emission Scanning Electron Microscope
TEM: Transmission Electron Microscope
HRTEM: High resolution TEM
EELS: Electron Energy Loss Spectroscopy
EFTEM: Energy Filtered TEM
EDX: Energy Dispersive X-ray spectrometry
CVD: Chemical Vapour Deposition
MBE: Molecular Beam Epitaxy
X-TEM: Cross sectional TEM
FTO: Fluorine doped tin oxide
DI: Deionized water
SE: Secondary electron
BSE: Back scattered electron
ETD: Everhart-Thornley detector
FEG: Field Emission Gun
LMIS: Liquid Metal Ion Source
GIS: Gas Injection Source
X-TEM: Cross sectional TEM
FIB: Focused Ion Beam
BF: Bright field
DF: Dark Field
ED: Electron Diffraction
SAED: Selective Area Electron Diffraction
CCD: Charge couple device
STEM: Scanning TEM
ADF: Annular Dark Field Detector
HAADF: High Angle Annular Dark Field Detector

STEM-EDX: STEM- Energy Dispersive X-ray spectrometry
GIF: Gatan Imaging Filter
ZLP: Zero Loss Peak
PVD: Physical vapour deposition
VS: Vapour Solid
VLS: Vapour Liquid Solid
PIN: Preferential Interface Nucleation
ROI: Region of interest
CCS: Cleaning cross section
NRs: Nanorods
I: Current
V: Applied Bias
G: Photoconductive gain
λ: wavelength
V: Volt
μm: Micrometer
nm: Nanometer
A: Ampere
R: Sample Resistance
T: Temperature
t: time
h: Plank's Constant
K or K$_B$ or k: Boltzmann Constant
d: Diameter
CEAS: Cavity Enhanced Absorption Spectroscopy
FET: Field Effect Transistor
PMMA: Polymethyl methacrylate
EDL: Electric Double Layer
V$_g$: Gate voltage
V$_{ds}$: Source-drain Voltage
I$_{ds}$: Source-Drain current
PEO: Polyethylene Oxide
LiClO$_4$: Lithium perchlorate
BET: Brunauer–Emmett–Teller
IRMS: Isotope-Ratio Mass Spectrometry

Contents

List of figures

xiv

List of tables

Chapter 1

Introduction

This thesis provides information about synthesis and physical property study of binary oxide nanostructures (e.g WO$_3$, TiO$_2$). Binary oxide nanostructure has been at the center of attention in last 4-5 decades due to its versatile nanostructure and various synthesis techniques, due to which one might be able to control/modify its physical properties. This control over physical properties has drawn attention due to the wide applications of metal binary oxides in the field of nanotechnology especially optical, energy, gas sensing and electrical etc. [1-9]. This thesis focuses on these aspect and underlying physics behind this. The main motivation of this thesis work involves growth of aligned one dimensional (1D) metal binary oxide nanostructures in physical vapour deposition (e.g. Pulse Laser Deposition (PLD)), hydrothermal (wet chemistry) techniques and porous 1D nanostructure by hydrothermal method controlling the growth parameters. Further, the physics behind the growth of these nanostructures has been investigated by interface physics study using spatially resolved tools and techniques. In this thesis, analysis has also been carried out to investigate the effect of size, shape and morphology tuning of metal binary oxide nanostructures (e.g.WO$_3$) on the physical properties (e.g. opto-electrical, gas transport). A brief review about the crystal structure, interesting physical properties of these metal binary oxides have been provided in this chapter. Lastly an overall outline of the thesis has been presented in this chapter to highlight the main research works of this thesis.

1.1 Introduction to binary oxides

One of the most promising field in the scientific and engineering communities is synthesis of binary oxide thin films and nanostructures (e.g. nanowires (NWs)), nanorods, nanobelts and nanotubes) for their potential advanced technological applications as nanoscale devices and also in the domain of basic nanoscience research [1,3,6-7,9]. Study on synthesis and physical properties of binary oxide nanostructure will provide information about the effect of size reduction, shape and morphology modification upon physical properties (e.g. optical, opto-electrical, electrical transport and gas transport etc.) [10-11].

Among all the binary oxides, metal binary oxides (e.g. WO_3, TiO_2 etc.) are much more promising in terms of application in nanoscale regimes. Especially tungsten and titanium oxides are widely studied in last few decades for their synthesis of different types of nanostructures and devices followed by a wide variety of applications in energy harvesting like solar cell, environmental hygiene, harmful gas sensing devices etc. It has also been observed that at nanoscale level metal binary oxides show modified as well as novel physical properties compared to their bulk version [1, 3-7, 12].

In earlier reports research has been carried out on different metal binary oxide nanostructures synthesis, properties and applications [4-5,12-17], but effect of size, shape tailoring upon physical properties and its outcome was less studied due to difficulties in device fabrication with homogenous composition, controlled shape and size of the nanostructure. Also the possible mechanism behind size, shape tailoring and growth was less studied considering the requirement of spatially resolved tools and techniques. Thus the control of growth parameter, interface physics behind growth of nanostructures on different substrates and the possible mechanism for different physical properties are still an open field for research.

This thesis has concentrated on the synthesis of metal binary oxide thin film and nanostructures by controlling the growth parameters in different growth techniques (e.g. Pulse laser deposition (PLD)), Wet chemistry synthesis (Hydrothermal method) etc. The growth of aligned nanowires starting from thin film is a non-trivial growth method in PLD, which has been achieved in this thesis by tuning the growth parameters. To the best of our knowledge, it has not been reported earlier. In hydrothermal route, synthesis of vertically aligned nanorods, and one dimensional (1D) porous nanostructure were also another development achieved in this thesis work.

The understanding of the growth dynamics has been successfully provided in detail by investigation on interface physics at the substrate and nanostructure interface down to tens of nanometer level and surface chemistry analysis in this thesis. This study was possible by utilizing spatially resolved sample preparation and characterization tools and techniques. This kind of interface physics study for understanding growth mechanism of aligned nanowires using the spatially resolved tools was not reported earlier.

In this thesis, the grown binary oxide nanostructures (e.g. WO_3) have been utilized in fabrication of devices for the analysis of effect of size, shape and morphology tuning on physical properties (e.g. Opto-electrical, gas transport). The size, shape and morphology tuning of nanostructure was a non-trivial process and involves greater knowledge about the growth dynamics of the material, which in turns provides information about the origin of different physical properties and its modification.

Previously the interaction of gas with binary oxides was mainly analyzed using the electrical response of those materials under different gas environments [18-20]. In this thesis, the study of diffusion/transport of gases through 1D porous metal binary oxide nanostructures (e.g. WO_3) (nanowires, nanotubes) was performed using spatially resolved laser spectroscopy analysis and the interesting new phenomena of isotopic selective gas transport through the porous nanostructure has been observed.

1.2   Fundamental properties of binary oxides

This section provides a review about fundamental properties like, crystal structure, phase, physical and chemical properties (e.g. optical, electrical, gas sensing and electrochromism etc.) of binary oxides. This thesis mainly focuses on metal binary oxides among those further studies on growth of tungsten oxide (WO_3), titanium oxide (TiO_2) and physical property study on WO_3 nanostructures have been performed. Hence, the review of fundamental properties will be focused on those two binary oxides.

1.2.1 Crystal structure and phase of binary oxides

Metal Binary oxides are most widely used material from its bulk or nano form due to its versatile nanostructures and properties. In this section further information will be provided on nanostructured WO_3 and TiO_2 as they are extensively studied in past few decades considering

wide variety of physical properties (e.g. optical, electrical, electrochromic, photocatalytic, and solar cell) [5-7, 13-16].

a) *Crystal structures and phases of Tungsten Oxide (WO₃):*

Tungsten oxide (WO_3) is a metal binary oxide having simplest cubic structure like ReO_3, formed by corner sharing of regular octahedrons of WO_6 octahedra. As a function of temperature different phases of WO_3 are: monoclinic II (ϵ -WO_3) <-43°C, triclinic (δ -WO_3) from -43°C to 17°C, monoclinic I (γ -WO_3) from 17°C to 330°C, orthorhombic (β -WO_3) from 330°C to 740°C, tetragonal (α -WO_3) > 740°C [21-23]. The structural model of all the structures was 1st provided by P. Roussel in 2000 and recently provided by F. Wang et.al in 2011 (Fig. 1.1(a-f)) that also supported in review research work by H. Zheng group in 2011 and Ting Guo group in 2015 [4, 20-24]. In another recent work by S. Pokhrel et.al [25] provided a clear relation between different crystals (e.g. monoclinic (m), orthorhombic (O) and tetragonal (t)). The lattice parameters are related by this relation: $a_m \approx a_o \approx (a_t - b_t)$; $b_m \approx c_o \approx (a_t + b_t)$; $c_m \approx b_o \approx c_t$. There is a mention of another stable structure of WO_3 being hexagonal WO_3 (h-WO_3), first reported by Gerand et.al in 1979, [26] and which was further confirmed by other research works by different groups [27-30]. Fig. 1.2 represents the schematic hexagonal WO_3 structure obtained from WO_6 octahedra. In the ab plane three and six- membered rings are present. This three and six member rings from trigonal cavity appearance and hexagonal windows respectively [30]. Although the hexagonal structure is also metastable above 400°C and annealing exceeding that temperature transforms it into monoclinic structure [31-33]. The phase transition behaviour in case of nanostructured WO_3 or WO_x is completely dominated by the synthesis process and the precursor used for that synthesis. The size reduction of WO_x crystallites increases the surface energy and reduces the melting and sublimation temperatures, as proposed from the Gibbs-Thomson expression [34, 35]. Therefore phase transition of WO_x nanostructures occurred at lower annealing temperature compared to bulk WO_3 [35]. In a report of Boulova and Liu et.al [33, 35-38] using in situ Raman spectroscopy for WO_3 nanoparticles (2-500nm), phase transition was observed at lower temperatures compared to its bulk counterpart as mentioned earlier. The Raman spectroscopy result for 60nm particle confirmed the phase transformation from γ to β WO_3 at 270ºC and to α WO_3 at 670ºC. Few recent works also stated about the stability of orthorhombic phase provided post annealing done on the as prepared nanostructures [37, 39].
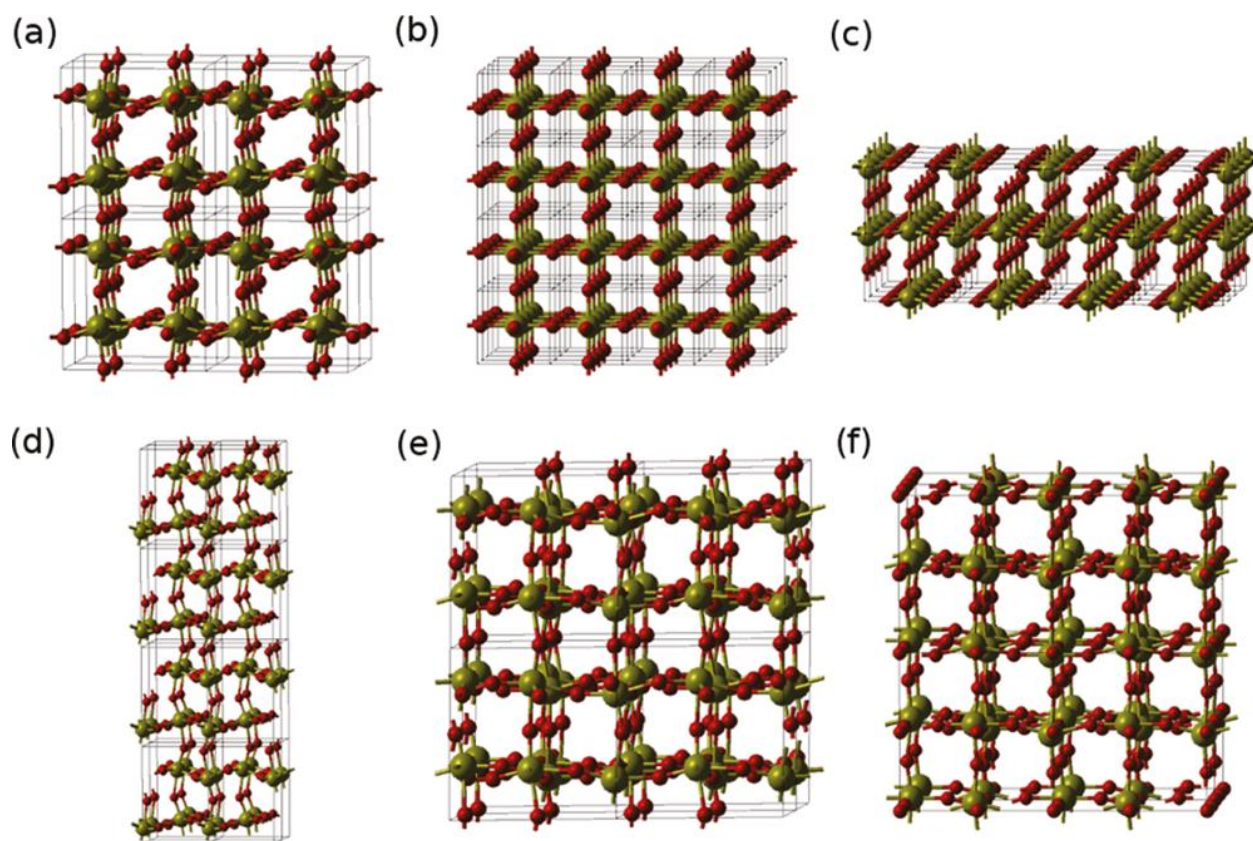
Figure 1.1: *Structural models of WO$_3$ structures (a) room temperature monoclinic (γ–WO$_3$), (b) simple cubic, (c) tetragonal (α–WO$_3$), (d) low temperature monoclinic (ε–WO$_3$), (e) triclinic (δ–WO$_3$) and (f) orthorhombic (β–WO$_3$). Spheres represent W (green balls) and O (red balls) atoms. All the models shown contain 256 atoms. Reprinted with permission © 2011, ACS Publication [21].*
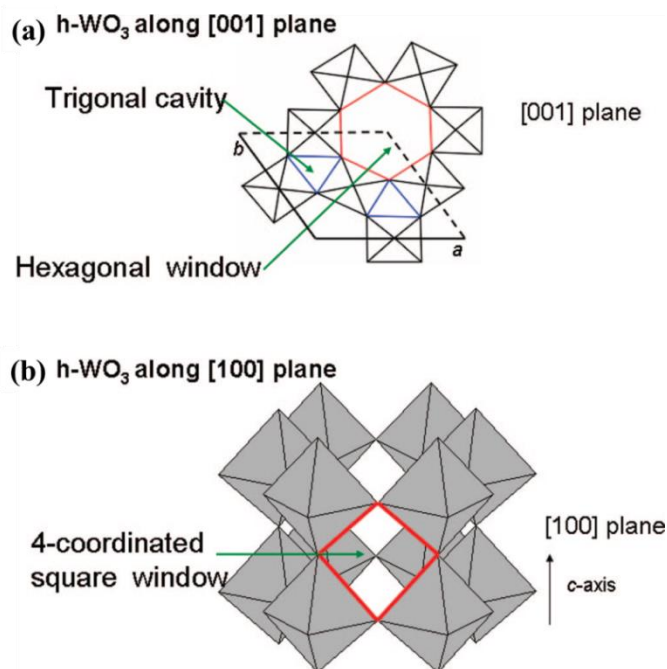
Figure 1.2: *The hexagonal-WO$_3$ structure along (a) [001] plane, (b) [100] plane. Reprinted with permission © 2009, ACS Publications [30].*

This thesis provided information about controlling the crystal structure of 1D nanostructure in PLD synthesis and effect of tuning of parameters on the same which was not well studied in this context. WO$_3$ is a transition metal oxide and consists of perovskite units, which supports non-stoichiometric properties as the lattice can withstand significant amount of oxygen deficiency [40, 41]. It was also reported that the electronic band structure (or conductivity) of WO$_3$ could be modified by a large amount with a small deficiency in oxygen [41, 42]. Few commonly known WO$_x$ compositions are W$_{20}$O$_{58}$, W$_{18}$O$_{49}$, W$_{24}$O$_{68}$ formed by corner sharing of WO$_6$ partially at the edge, alternating the octahedra. This change in structure was due to oxygen reduction [40, 41]. The reduction, elimination of oxygen takes place due to crystal shear mechanism [40, 41].

b) *Crystal structures and phases of Titanium Oxide (TiO$_2$):*

Titanium Oxides (TiO$_2$) have been the commonly used metal oxides since early twentieth century for its application in pigmentation, painting technology etc. It has two known and stable structure: rutile, anatase and one rare structure: brookite. In TiO$_2$ structureTi^{4+} ions are surrounded by an octahedron of six O^{2-} ions to configure chains of TiO$_6$ octahedra which form these three crystal structures of TiO$_2$ [43-45] [Fig. 1.3]. In a recent report it has been

observed that as prepared TiO_2 nanostructures shows amorphous nature which under heat treatment modifies it from amorphous to rutile and anatase structure [46]. The two stable crystal structures differ in two points (i) distortion of the octahedron, (ii) octahedron chain assembly pattern.
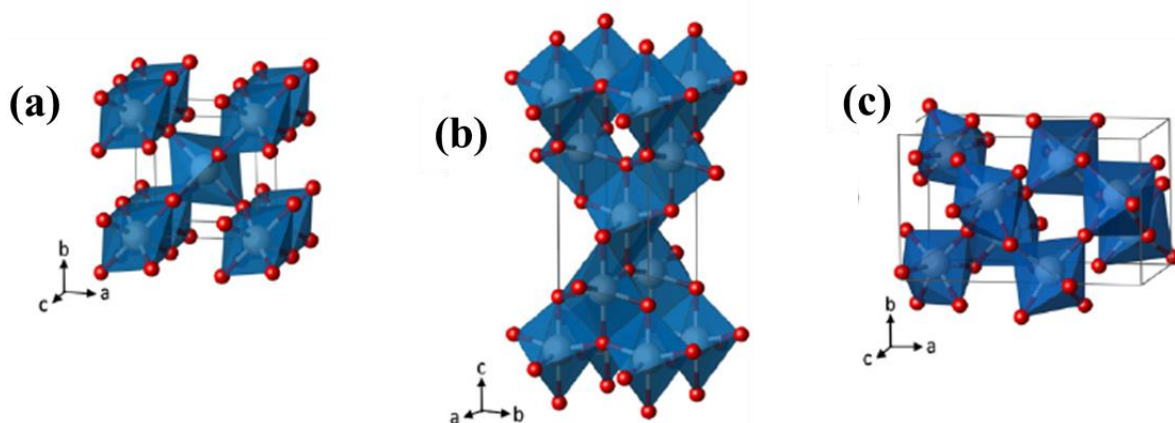
Figure 1.3: *Crystal structures schematic diagram of TiO_2 (a) rutile, (b) anatase, and (c) brookite; Ti (Blue), O (Red). Reprinted with permission © 2012, IOP Publishing [44].*

The overall differences between rutile and anatase crystals of TiO_2 are sum up in Table 1.1.

Table 1.1: *Comparison between Rutile and Anatase TiO_2 crystal phases*

Rutile TiO_2	Anatase TiO_2
• Octahedron shows slight Orthorhombic distortion	• Octahedron shows distortion to lose the orthorhombic symmetry
• Ti-Ti bond length is large.	• Ti-Ti bond length is small.
• Octahedron surrounded by 10 neighbor octahedron	• Octahedron Surrounded by 8 neighbor octahedron

Fig. 1.4 shows X-Ray Diffraction (XRD) patterns of TiO_2 nanoparticles having different crystal structures. It has also been reported that as the peaks get narrower the size becomes larger for nanoparticles [47-52]. Although in case of nanorods the growth direction was confirmed by the sharp peak at that orientation. Zhang et.al showed in their report about the sharp peak along [004] direction and broader peak in all other directions. This report was confirmed by many other reports [47, 52-54].

This thesis provides information about 1D TiO_2 nanostructure growth with high crystallinity along with understanding on effect of substrate surface chemistry and growth parameters on crystal structure and surface morphology.
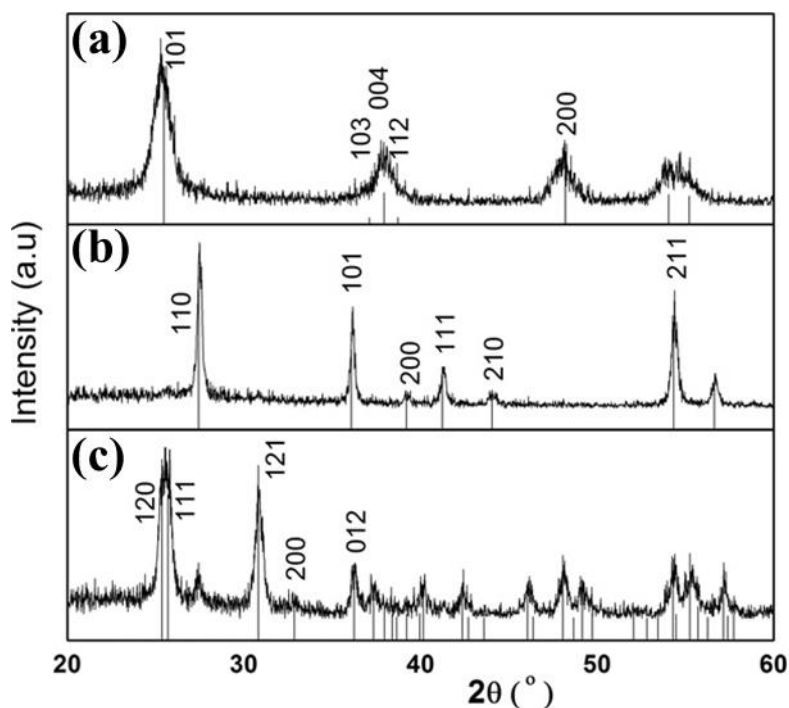
Figure 1.4: XRD patterns of TiO_2 nanoparticles prepared by hydrothermal treatment (a) anatase: 1.5 M acetic acid, 6 h 200^oC, (b) rutile: 4 M HCl, 8 h, 200^oC, (c) brookite: 3 M HCl, 7 h, 175^oC. The reference line patterns correspond to the JCPDS: No 21-1272 (a), No 21-1276 (b) and No 29-1360 (c), respectively. Reprinted with permission © 2008, IOP Publishing [48].

1.2.2 Optical and electrochromic properties of binary oxides

Among different physical properties of binary oxide optical properties are studied for last 5-6 decades due to potential applications in solar cell technology, optical sensors and other optical devices. In recent times Zinc oxide (ZnO) has been studied the most [8-9] in view of its optical property. In this thesis interest in other metal binary oxides (e.g. WO_3,) having similar properties has been shown. In this section optical properties of WO_3 will be discussed. Tungsten oxide, a n-type wide band gap semiconductor where the valance band is formed by O 2p orbital and the conduction band formed by W 5d orbital [41, 54]. The electronic band gap between these two bands is E_g. Earlier reports and analysis confirmed that the band gap of amorphous WO_3 is much higher (3.25eV) compared to crystal phase WO_3 (Monoclinic E_g = 2.62 eV) [41]. In case of nanostructured WO_3, it has been reported that with the reduction in grain size of the nanostructure, the band gap reduces [54] and this was experimentally

confirmed from the blue shift in the Ultraviolet (UV)-Visible spectra of those nanostructure having different grain size [55]. This shift is well defined using Quantum Confinement (QC) [54, 56], which is broadly divided into two regimes; strong QC found in materials with size smaller than its Bohr radius ($WO_3 \approx 3nm$ radius) affecting electron wave function hence E_g [57]. The other one is weak QC found in materials with larger size than its Bohr radius which showed stable modification of E_g by indirect perturbation of electron wave function due to coulomb effect [56].

In a report by Gullapalli et.al [54] they had synthesized WO_3 nanostructures of different size (9-50nm) by Radio Frequency (RF) sputtering at temperature range (100-500°C) and observed the transmission spectroscopy and confirmed that due to reduction in crystal size blue shift takes place and the band gap widened Fig. 1.5(a). It has also been observed that γ-WO_3 grown at temperature 300-500°C have wider band gap compared to its bulk counterpart (E_g = 2.62eV), which supports the weak QC effect. It has been further confirmed that the phase transformation due to increase in temperature also plays an important role in modification of E_g (Fig. 1.5(b)) [54].
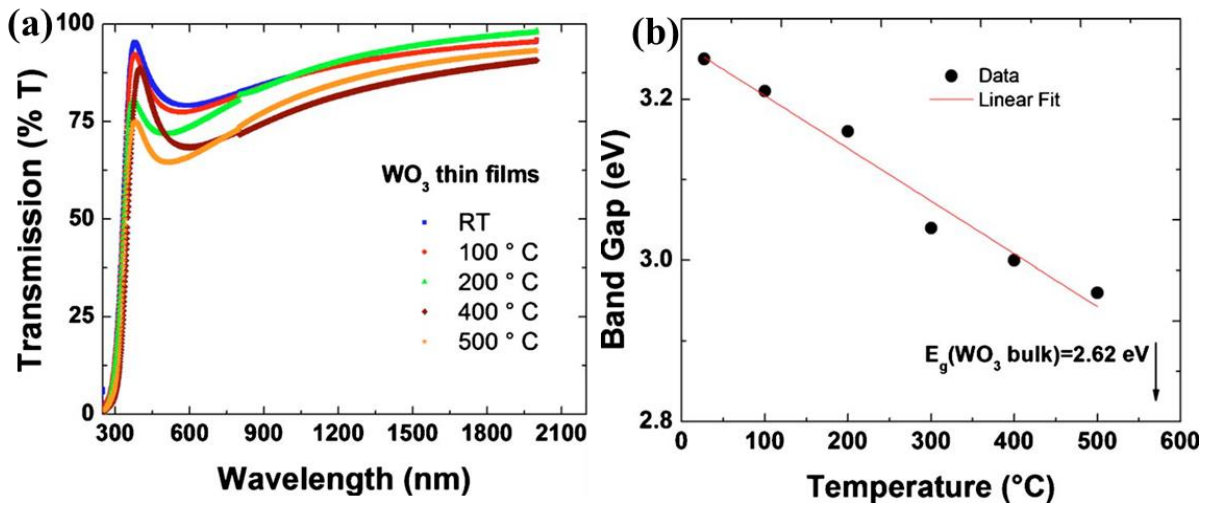
Figure 1.5*: The RF-sputtered WO_3 thin films (a) Transmittance spectra at different substrate temperatures, (b) T_s–E_g relationship; Reprinted with permission © 2010, American Institute of Physics [54].*

An optical property of a material is determined by absorption wavelength which is actually governed by energy bandgap. As mentioned earlier from different reports and studies typical bandgap for WO_3 is 2.60-3.25eV with a blue shift from bulk to nanostructure [54-55, 58-59]. WO_3 was reported to be typically transparent to light in the visible region. The absorption of

light in case of light (Photon) energy is higher than the band gap energy and may be approximated using the equation 1.1: [55]

$$\varepsilon \ \alpha \ (\varepsilon\text{-}E_g)^{\eta}\ldots\ldots\ldots\ldots(1.1)$$

Where, ε = the photon energy and η =2 considering indirect transitions in case of WO_3. In Fig. 1.5(a) transmission spectra of WO_3 material, showed absorption edge from UV to blue wavelength [54]. In case of nonstoichiometric tungsten oxide (WO_x, typically found in light green colour) the transmission edge in blue-green region observed with a broad absorption peak in red to infrared region. Reports confirmed that this happens due to electron transfer from W^{6+} to W^{5+} [59]. Other important parameters for optical devices are refractive index which in case of WO_3 is around 2-2.5 [60]. The effect of surface morphology tuning on optical response modification was not explored in detail which has been highlighted in this thesis.

Beside optical properties WO_3 also showed response in terms of colour change due to electrochemical reaction, known as electrochromic effect. In this reaction injection of positive ions (x) and equal quantity of electron (e⁻) takes place following equation 1.2:

$$WO_3 + xM+ + x\text{-}M_xWO_3\ldots\ldots\ldots\ldots\ldots\ldots(1.2)$$

Where, M = Li, H and Na, and x stands for stoichiometric quantity. Earlier studies provided information about this reaction and also showed that this electrochemical response arises also due to crystal structure of WO_3. Amorphous and crystalline WO_3 gives different electrochromic response [61-65]. In the visible region absorption peak was observed in case of amorphous WO_3 corresponding to polaron absorption, whereas crystalline WO_3 had smaller absorption response under different wavelength. In case of amorphous films, electrons are localized in the W^{5+} sites induces lattice vibration by polarizing their surroundings [66, 67]. The inserted cation (M+) was spatially separated from electrons either sitting in the centre of the perovskite or chemically bounding with electrons and creates polarons [68, 69]. In case of crystalline films those electrons follow Drude model followed by scattering due to impurities [69]. This promotes metallic nature of the film and at infrared wavelengths reflectivity increases along with higher absorption at all wavelength. This lowers the chromic response of the films [70].

Electric Double Layer Field Effect Transistor (EDL-FET) characteristics will be studied using WO_3 thin film as channel. But, due to electrochromic effect lithium tungstate was formed by reaction of WO_3 with the gate material (mixture of $LiClO_4$ and PEO) and the

initially obtained response was not reproducible more than 1-2 times. The results and explanation are provided in appendix in this thesis.

1.2.3 Opto-electrical property of binary oxides

Electrical conductivity (in presence or absence of light) is mainly dominated by the number of free electrons present in the conduction band in case of n-type metal oxide semiconductor materials. The stoichiometric defects like oxygen vacancies play an important role for controlling generation of free electrons in the conduction band [71].

Opto-electrical response was studied for few decades in WO_3 thin film and nanostructures mainly for photo electrochemical (e.g. water splitting) and other applications. Many reports are found in case ZnO nanostructure for opto-electrical property analysis in recent few years [72-73]. In last one decade WO_3 also creates much more attention as an opto-electrical device. In Yang et.al report they have shown photoresponse in WO_3 nanostructured film by sol-gel method [74]. Another report by Huang et.al provided information about a large photoreponse along on a single WO_3 nanowire in vacuum and air [1]. The photo current decays very quickly once the device was put in atmospheric condition from vacuum, after illumination was turned off, as shown in Fig.1.6 (a). Also the response was increase very rapidly when it was exposed to UV light as shown in Fig. 1.6 (b) (explained in section 1.2.2). This response actually described about the Persistence Photocurrent (PPC) after removal of illumination. This was earlier observed in case of ZnO nanostructured film by another group [75]. In this thesis further investigation has been carried out to observe how one can tune opto-electrical response of WO_3 films and nanostructures by tailoring the surface morphology, which has not been explored in great detail earlier.
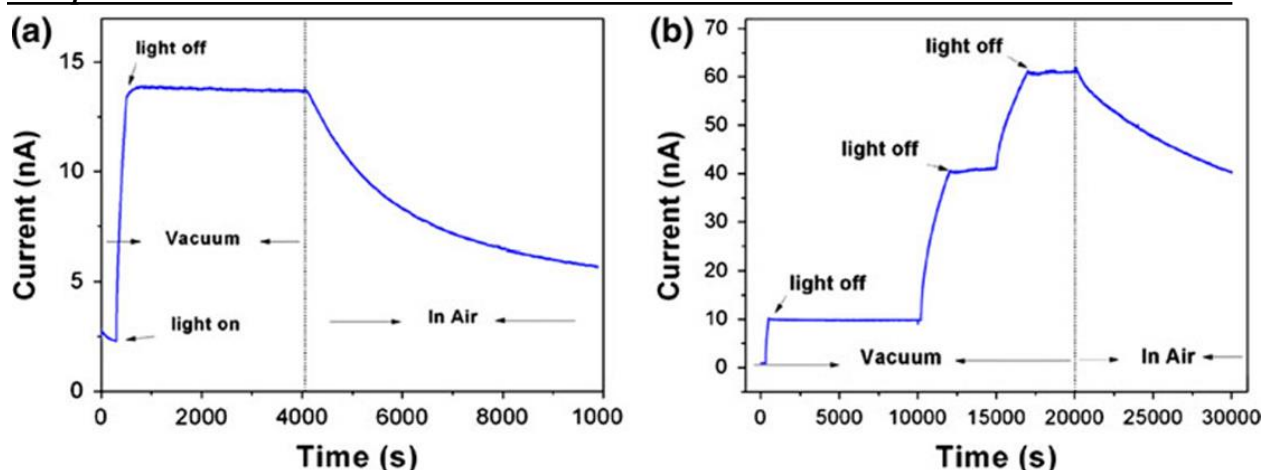
Figure 1.6: (a) The persistent photoconductivity of the WO₃ nanowire device under vacuum and in air conditions, (b) The persistent photoconductivity under discontinuous UV illumination. All the biases are 0.1 V. Reprinted with permission © 2011, Springer open [1].

1.2.4 Gas transport property of porous binary oxides

Another important physical property of metal oxides semiconductors was observed in 6-7 decades ago, of its ability to respond in presence of different gases [76].

Among them, WO_3 grabs more attention due its wide band gap and n-type nature. In last 2 decades mainly porous 1D metal oxide nanomaterial (having large surface aspect ratio, length: diameter) has garnered more attention due to their higher ability to interact with gases. This interaction not only occurs at the surface but also inside the bulk [77]. This leads to synthesis of various porous metal oxide films and nanostructures (e.g. nanowires, nanotubes, nanoplates, nanoneedles, nanorods and nanoparticles etc.) [78-84], for analysis of gas transport/diffusion property. Till date reports regarding interaction of gases with binary oxide nanostructures has been mainly reported as changes in electrical property for gases like NO, NO_2, H_2, H_2S [84-86], as well as for volatile organic gas compounds like ethanol, acetone [79, 87]. Also in last few decades it has been observed that to increase the sensitivity and selectivity of gas interaction, various materials coating or decoration (e.g. Pd, Pt, and Au) have been used [81-82, 87-88]. Very recently J. Li et.al provided a comparative study on gas sensing by hydrothermally synthesized self-assembled hierarchical tungsten oxide hollow sphere (HS) [89]. The Study provided information about higher sensitivity of NO_2 gas over other gases like H_2, CO, C_2H_5OH etc. In Fig. 1.7 Field Emission Scanning Electron Microscope (FESEM) image of hollow sphere annealed at different temperature which also improves the gas sensing in terms of change in resistivity and Fig. 1.8 its NO_2 gas sensing

response along with other gases has been shown. The response was studied at different temperature based on the change in resistance of the nanomaterial.

The study of gas transport property also includes analysis regarding the mechanism behind the gas sensitivity. In the two last decades few reports provided information about the sensing mechanism from the gas diffusion aspect and for which, additionally except the size, shape and morphology of nanostructure, porosity along with large aspect ratio was considered for better sensitivity of gases in metal binary oxides [77, 90].
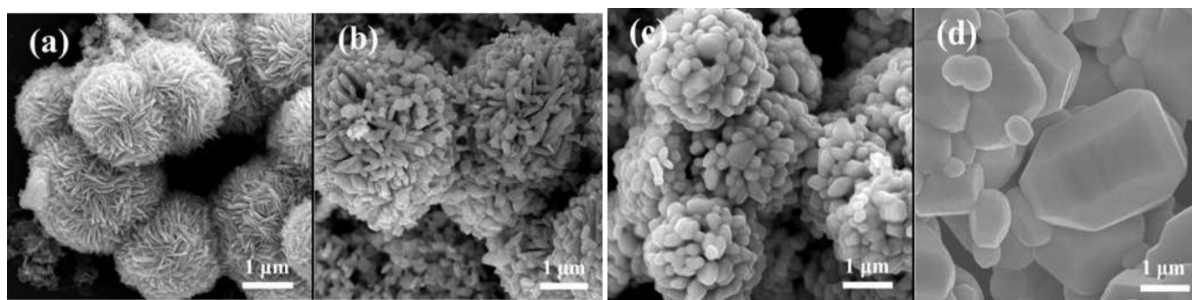
Figure 1.7: *FESEM images of the WO$_3$·H$_2$O products annealed at (a) 400°C, (b) 500°C, (c) 600°C and (d) 700°C in air for 1 h. Reprinted with permission © 2015,ACS Publication [89].*
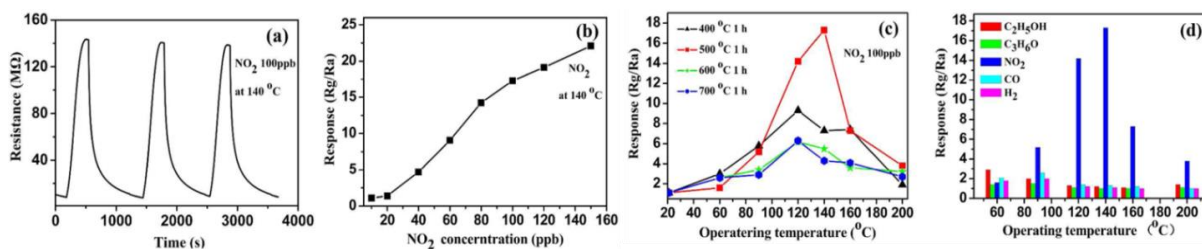
Figure 1.8: *The hierarchical WO$_3$ HS (a) Response and recovery curves for 100 ppb NO$_2$ after 3 cycles of gas on and off at 140°C, (b) Response curve to different concentrations of NO$_2$ ranging from 10 to 150 ppb and measured at 140°C; Responses of WO$_3$ material (c) annealed at different temperatures to 100 ppb NO$_2$ at different operating temperatures, (d) Responses to various gases at different operating temperatures. Reprinted with permission © 2015, ACS Publication, [89].*

Porous structure and large aspect ratio is possible for nanowires, nanotubes and nanosheets which shows better gas sensitivity [77, 91]. Guo et.al developed highly porous CdO nanowires and showed that it provides better gas sensitivity due to large surface area for better gas diffusion inside the nanowires [90].

In Fig.1.9 (a) shows High Resolution Transmission Electron Microscope (HR-TEM) images of those nanowires and in Fig. 1.9 (b) gas sensing response at different concentration of NO$_x$.

It has been observed from the gas sensing response that the device fabricated using porous CdO nanowires possess good response time, high signal to noise ratio with sensitivity down to 1ppm of NO_x [90].
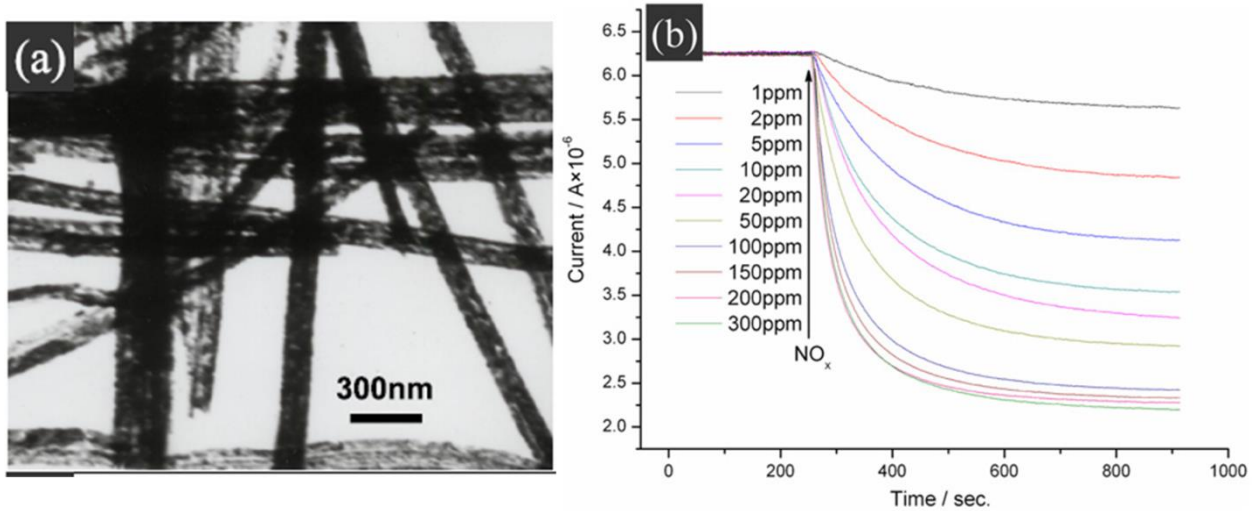
Figure 1.9*: (a) High-Resolution TEM image of porous CdO nanowires, (b) real-time response of the sensor device upon exposure to different concentrations of NO_x with the device bias fixed at 0.1 V. Reprinted with permission © 2008, IOP Publishing [90].*

The gas diffusion through porous 1D nanostructure of binary oxide (e.g. WO_3) has been shown in this thesis and interestingly it has been observed that during diffusion of a gas, separation of isotopes of that gas occurs (e.g. $^{12}CO_2$, $^{13}CO_2$) [92]. It is a new observation and was not reported before. The details analysis and discussion of results have been provided in this thesis.

1.3 Synthesis techniques of binary oxide thin films and nanostructures

Binary oxide synthesis was done using different techniques such as Physical Vapour Deposition (PVD) and Wet Chemistry etc. techniques for the last 5-6 decades and very few reports are available about tuning morphology of binary oxides during synthesis. Among different growth techniques for thin film and nanostructures of binary oxides few of the common techniques which had been used extensively for growth engineering are sputtering, thermal evaporation, spray pyrolysis, template, hydrothermal, sol-gel method, Chemical Vapour Deposition (CVD) and Pulse Laser Deposition (PLD, a type of PVD) techniques mainly for thin films growth [93-98]. In these different growth techniques different structures like 0-D (nanoparticles) to 3-D (polyhedrons) and other hierarchical structures were grown.

Though synthesis of binary oxides (e.g WO_3, ferrites, ZnO) nanostructures like nanoparticles [99], nanorods on different substrate [100] doped nanorods [101], catalyst free nanorod [102-103], nanorods arrays [104-106] and nanoplates [107] etc. using PLD and wet chemistry (hydrothermal) technique have been reported earlier but detailed characterization, growth mechanism analysis was not performed. Fig. 1.10 shows SEM images of doped and undoped ferrite nanorods grown in PLD [102].
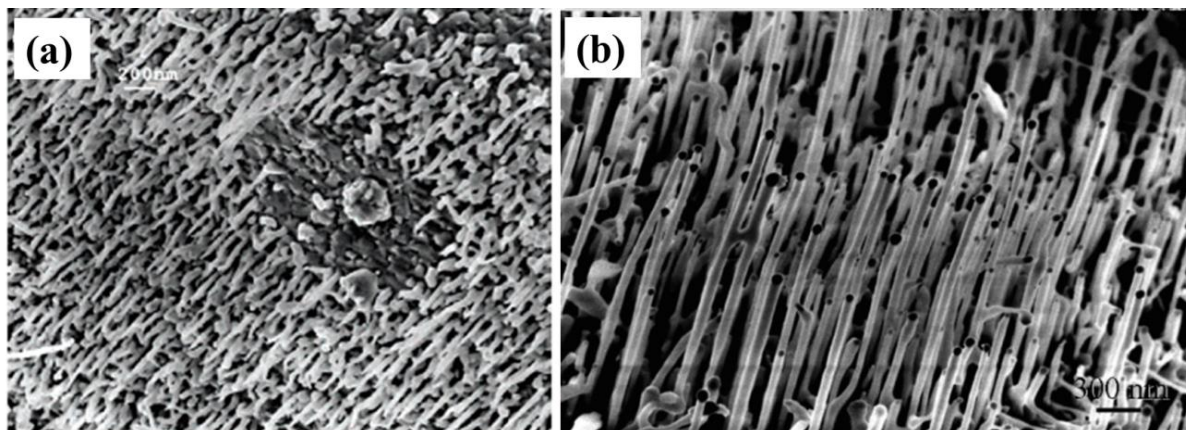
Figure 1.10*: (a) SEM image showing synthesized iron oxide nanorods, (b) Higher magnification SEM image showing aligned Mg-doped iron oxide nanorods. Reprinted with permission © 2006, ACS Publication [101].*

In Fig. 1.11 shows SEM images of WO_x nanostructures on Tungsten (W) substrate which are not vertically aligned, smaller in size grown in PLD [100]. Fig. 1.12 (a) shows FESEM image and (b-c) TEM images of WO_3 nanoplates having monoclinic structure, side length 100–170 nm thickness 30–50 nm grown in hydrothermal method [107]. In Fig 1.13 (a-d) shows FESEM images and cross sectional view of hydrothermally synthesized dopped and undopped TiO_2 nanorod arrays which are very small in length (500nm) [105].
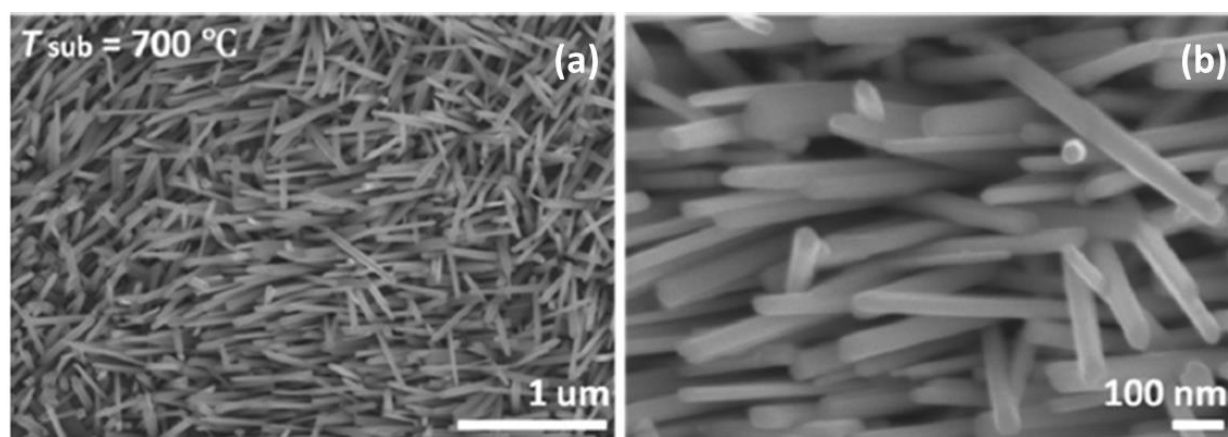
Figure 1.11: *SEM images of WO$_x$ nanorods on W substrate (a) Low magnification (b) High resolution. Reprinted with permission © 2014, The Royal Society of Chemistry [100].*
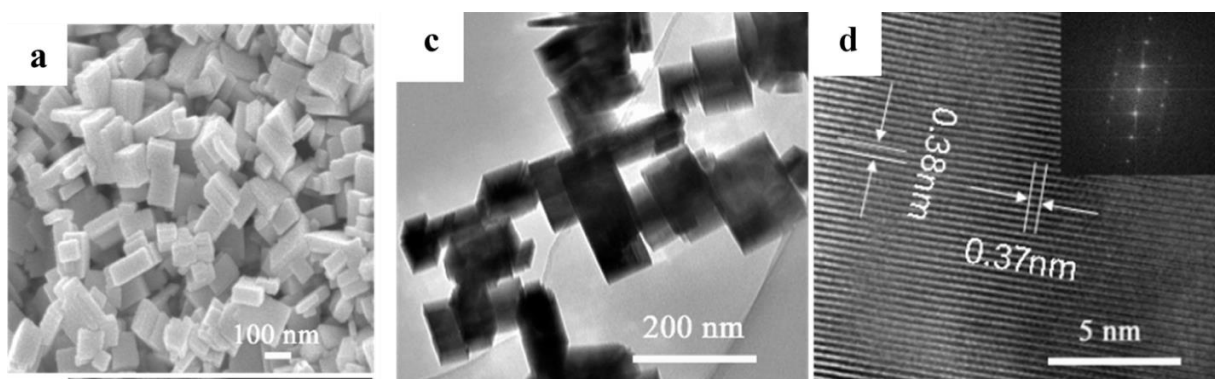
Figure 1.12: *WO$_3$ nanoplates (a) low magnification SEM image, (b) TEM image and (c) HRTEM image (The inset in (c) is the FFT pattern) of the as-obtained m-WO$_3$ nanoplates. Reprinted with permission © 2014, Elsevier B.V [108].*
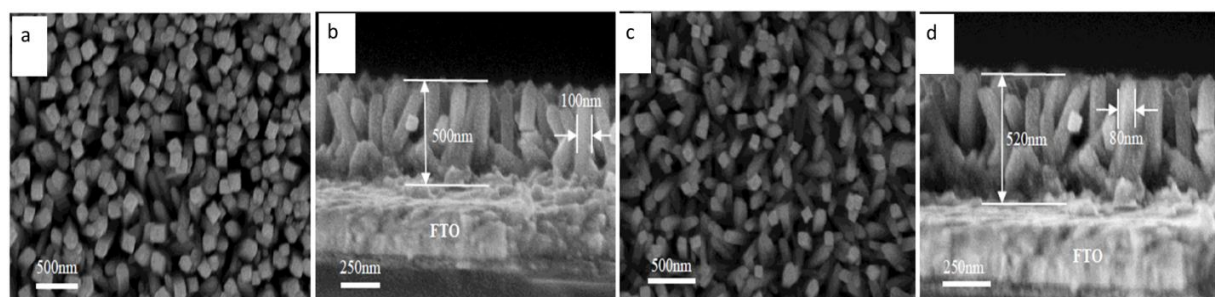
Figure 1.13: *FESEM images of (a) non-doped TiO$_2$ array, (b) Cross sectional view of non-doped TiO$_2$ array, (c) Doped TiO$_2$ array and (d) Cross sectional view doped TiO$_2$ array. Reprinted with permission © 2016, Elsevier Ltd. [105].*

In this thesis tuning of growth parameter in PLD and wet chemistry to tailor the shape, size, morphology, composition of nanostructures to standardize growth of vertically aligned

nanowires/nanorods staring from thin film, using seeding layer respectively and microstructural, interface physics and chemical analysis to understand growth mechanism has been provided in detail. Also role of substrate surface, crystal structure for growth of different nanostructure has been explained using spatially resolved tools and techniques. Information about growth of binary oxide nanostructures using different growth techniques and parameter tuning and controlling are still an open field of research, which has been explored in this thesis. No approach has been made earlier regarding growth method of nanowires starting from the bulk sample. Also the effect of such tuning on the physical property of the material requires greater investigation to explore physics behind the growth. This thesis emphasizes on this issues in detail.

1.4 Interface physics analysis of binary oxide nanostructures

In last 3 decades along with the study on material synthesis process using different techniques, microstructural analysis has grabbed a lot of attention for the understanding of growth mechanism, physical properties of nanostructure materials. Initially SEM and HRTEM provided morphological and structural information about materials. Still that investigation was incomplete when samples are grown as bottom up technique on a substrate. The substrate not only supports the material but also provides base to grow interesting nanostructure device for different applications. The mechanism and physics behind that growth was unknown till microstructural study was performed on a cross section of the whole material. This study provides information about the substrate and the growing material at the interface (e.g. modification or attachment in interface down to nanometer level). Y. Yoshimoto et.al report in 1995 about growth of CeO_2 thin film on Si (111) substrate using Molecular Beam Epitaxy (MBE) technique [108]. The cross sectional TEM analysis was performed at the interface and it gave information about the exact crystallographic orientation of the CeO_2 film on Si substrate (Fig. 1.14). It was also confirmed from the analysis that no amorphous layer was formed at the interface. Hence it was an epitaxial growth of CeO_2 thin film. This study actually gave insight about the growth of thin film with atomically sharp interface.
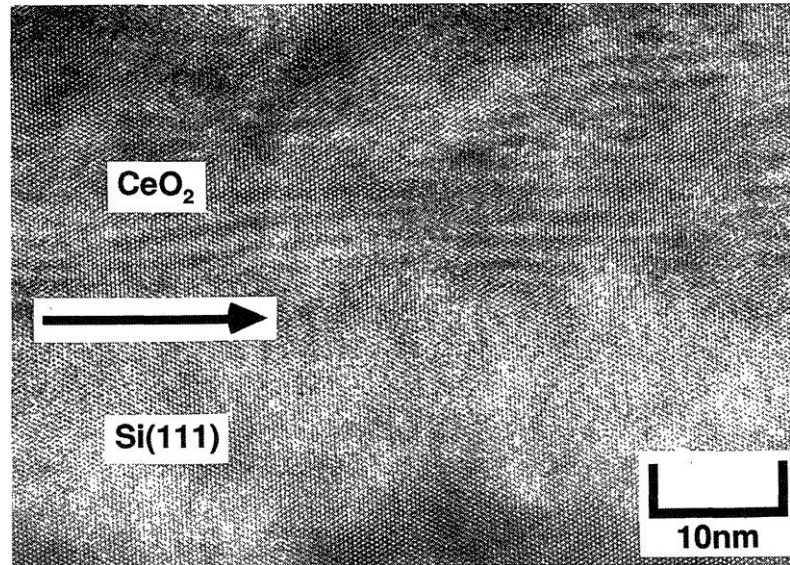
Figure 1.14*: Cross sectional lattice image at the interface observed form the [110] direction on CeO_2 film grown on Si (111) at 20^oC. Arrow indicates the interface. Reprinted with permission © 1995, Japan society of applied physics [108].*

Earlier in another report by T. Inoue et.al showed that the growth method and condition plays and important role for the formation of amorphous oxide layer in case of CeO_2 film on Si(111) [109]. This was confirmed using the cross sectional TEM analysis as shown in Fig. 1.15.
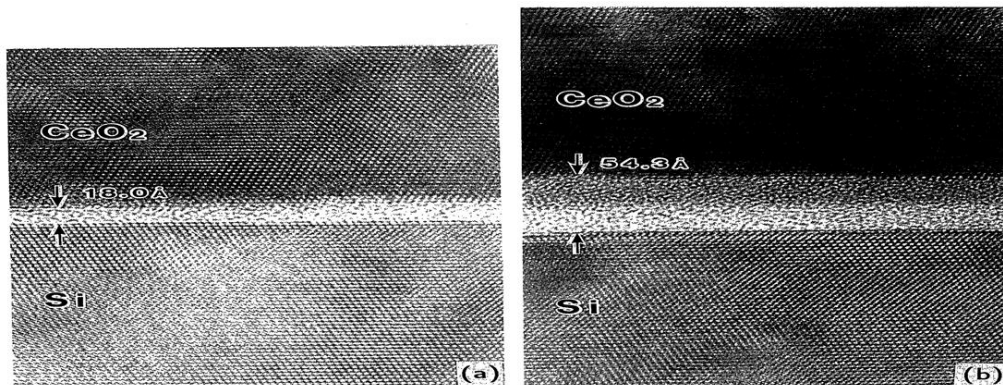
Figure: 1.15*: Cross sectional HRTEM image of CeO_2/Si(111) structure grown at (a) 200^oC, (b) 800^oC. Reprinted with permission © 1993, Japan society of applied physics[109].*

J. An et.al showed X-TEM analysis to give an insight about the development of Solid Oxide Fuel Cell consisting of Yttrium Doped Ceria (YDC) and Yttrium Stabilized Zirconia (YSZ) [110]. The microstructural and chemical analysis in TEM depicts the homogeneity at the interface level along with absence of intermixing in those layers (Fig. 1.16).
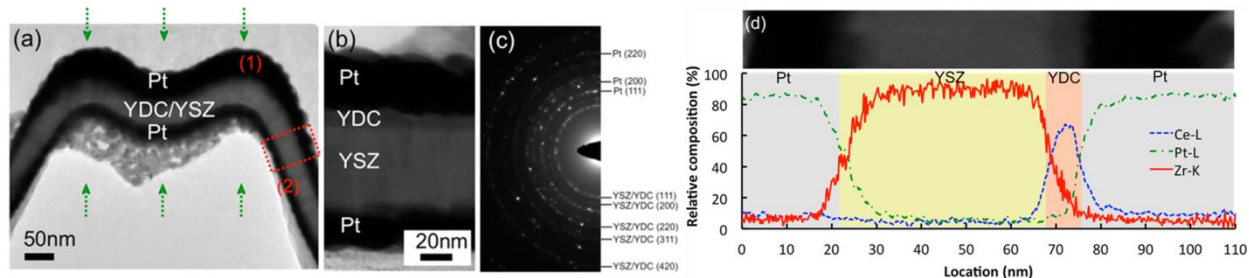
Figure 1.16: TEM images with diffraction and EDS (a) Bright field TEM image of the cross-section of the freestanding Membrane Electrode Assembly (MEA). The green-dotted lines represent the direction of the Pt sputtering, (b) Zoomed-in STEM image of the red-dotted area (slanted wall) in (a), (c) SAED pattern of the area shown in (b), (d) STEM-EDS elemental line profiles across the MEA. The image of the analyzed area is on top of the profile. Reprinted with permission © 2013, ACS Publication [110].

There are other reports where this cross sectional method was utilized to know the structure of the grown material and changes lead by electrical transport [111, 112].

As it has been possible to grow more complex nanostructure in last one decade for different applications, these make it very interesting to know the physics behind the same using this Cross Sectional TEM (X-TEM) technique.

In this thesis Cross Sectional samples have been prepared with advanced tools and techniques from binary oxide nanostructures (e.g. WO_3) like nanowires, thin films on a substrate and interface physics analysis has been carried out to understand possible growth mechanism, which was yet not explored in past times.

1.5 Motivation of the thesis work

- Size reduction of a material to nanometric size from bulk produces different nanostructures having 0-dimesion (0D) to 1, 2 or 3-dimension (1D, 2D or 3D). Different types of nanostructures have been synthesized and studied through theory and experimental investigations till date are nanoparticles (0D), nanowires, nanotubes and nanorods (1D) etc. Growth of binary oxides nanostructures (e.g. WO_3, TiO_2) in different shapes, sizes and morphology has grown in more importance in last 4-5 decades due to its potential for application in different fields. Still, growth method and controlled tuning of such parameters like size, shape, morphology, composition tailoring and synthesis of highly oriented crystalline binary oxide nanostructures with atomically sharp interface over a large surface area remains a challenge and is a very interesting field to work on. It

19

remains to a great extent an unexplored field. In this thesis emphasis has been given on this aspect.

- One of the pertinent questions that have been investigated in this thesis is the effect of modification of growth techniques and parameters that can tailor size, shape, morphology, crystallinity, and homogeneity of binary oxide nanostructures. Added to it the question of how the tailoring of size, shape, morphology and crystallinity of binary oxide nanostructures can tune the physical properties found in bulk counterpart of binary oxides. In this thesis the main interest is to study the above issues and also to standardize different synthesis techniques to synthesize vertically aligned 1D binary oxide nanostructures, 1D porous binary oxide nanostructure and understand possible physics behind the growth dynamics.

- Growth dynamics analysis demands study of interface physics, surface chemistry on a very good quality, highly crystalline nanostructured material with stoichiometric composition, crystallographic phase. The difficulties still remain related to the study on interface physics; surface chemistry at nanostructure and substrate interface as these involve spatially resolved analysis tools for cross sectional sample preparation and analysis on it.

- Spatially resolved tools for developing cross sectional sample and analysis has provided the information that lies at the interface has been analyzed in this thesis. The tuning of growth parameters and methods has an impact on substrate nanostructures interface and surface chemistry which required special analysis to establish the physics behind it. Spatially resolved tools based on Dual Beam Scanning Electron Microscope for Cross Sectional lamella preparation and Transmission Electron Microscope with Energy Dispersive X-ray spectrometry/Gatan Imaging Filter for microstructural as well as chemical compositional analysis has been utilized at substrate and nanostructure interface. The motivation has been depicted in Fig 1.17 which shows growth of different nanostructures starting from the bulk binary oxide.
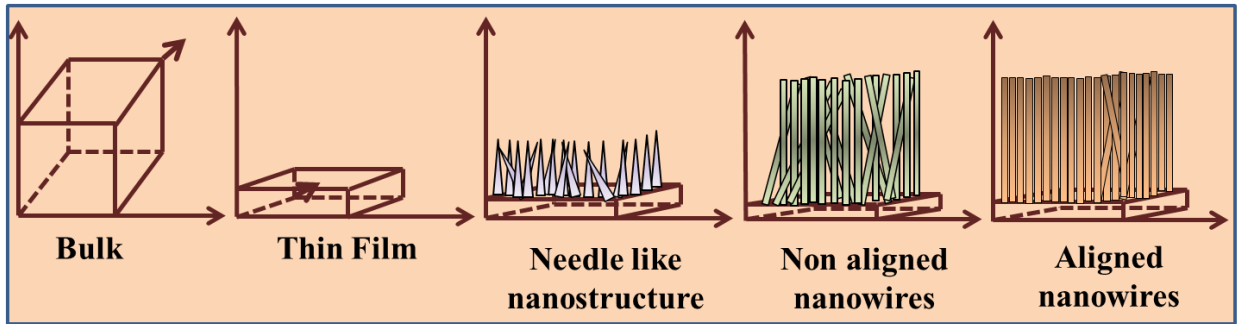
Figure 1.17*: Schematic diagram of tuning of the structure from bulk to Nano dimension.*

- Many reports are available on different physical properties of binary oxides having different nanostructure, however no reports were found on the modification/tuning of growth parameters and technique to control size, shape, morphology and stoichiometry of binary oxide nanostructures which might effect, modify or enhance physical property of those materials. Tuning of nanostructure and effect of it on physical property (e.g. Opto-electrical, gas transport) has been shown in this thesis. Study on these aspects will explore some interesting physics behind it. The study of opto-electrical response provides information about the modification of response with different surface morphologies. The gas transport property gave us a new direction to control greenhouse gas emission by gas diffusion using 1D porous nanostructure grown by this control growth technique, which opens up an advanced phenomenon (isotopic fractionation) and provides a platform to explore the science hidden in it. It is an interesting approach in the field of nano-device application as well as nanoscience, which has been explored to some extent in this thesis work too.

1.6   Layout of the thesis

This thesis is based on the following works: (1) Synthesis of binary oxide (WO_3, TiO_2) nanostructures (thin film, nanowires, nanorods, nanotubes) and their structural characterizations, (2) Study of interface physics of substrate and nanostructures, surface chemistry for understanding the growth mechanism using advance tools and techniques (3) Study on morphology dependent opto-electrical property of binary oxide thin film and nanostructures, (4) Analysis of transport of gases in porous 1D binary oxide nanostructures. This thesis has been divided into 5 main chapters along with summary listed as below:

1. In this present chapter, a brief overview of binary oxide structure, physical properties, synthesis route and the related study and review on it has been presented. This chapter also includes the necessary literature of the work in the field of binary oxide nanostructures synthesis and physical property and main motivation and objective of the present work.

2. The 2nd chapter gives a description of synthesis of binary oxide nanostructures by tuning different growth methods (PLD, Wet Chemistry), parameters and characterization along with brief details of the characterization tools/set-up.

3. The 3rd chapter provides detail about the study on growth mechanism by the understanding of interface physics of substrate and nanostructures interface using spatially resolved tools for the growth of 1D vertically aligned and partially aligned binary oxide nanostructures in Pulse Laser deposition (PLD), hydrothermal method and proposed possible mechanism to control the growth of binary oxide nanostructures and tailoring of size, shape, and morphology for the same. The surface chemistry analysis using Energy Filter Transmission Electron Microscopy/Electron Energy Loss Spectrometry (EFTEM/EELS) has been provided to check the material composition, homogeneity and also to understand the growth mechanism of binary oxide nanostructure in wet chemistry (hydrothermal) route.

4. The 4th chapter describes an important observation about the morphology dependent photoresponse/opto-electrical property measurement on binary oxide (WO_3) thin film and nanostructures with different surface morphology. The opto-electical response modified completely due to tuning of surface morphology of the binary oxide from film to nanostructured film. The wavelength dependency of the photoresponse has also been pointed out. Hence, this chapter will provides information about effect of morphology tuning upon physical property, which has not been reported so far.

5. The 5th chapter describes about the gas diffusion/transport property in one dimensional (1D) porous binary nanostructure (WO_3). The transport/diffusion showed isotope selectivity which was a very interesting and new approach to open up new dimension in the field of diffusion of gases in porous binary oxide nanostructures. The interesting

physics behind this isotope's selective diffusion property has also been pointed out in greater detail considering the large surface aspect ratio (length: diameter) of the porous nanostructure. This kind of new work along with the analysis has not been reported so far.

6. In the last chapter the summary and concluding remarks of this thesis work has been provided along with main achievements of the thesis work and future challenges.

Finally this thesis ends up with appendix providing a very brief approach to electric double layer gate device opto-electrical response of WO_3 thin film grown in PLD and the limitation in that measurement due to electrochromic effect of WO_3.

Bibliography

1. K. Huang, Q. Zhang, Nanoscale Res. Lett., 6, 52, 2011.

2. P. P. González-Borrero, F. Sato, A. N. Medina, M. L. Baesso, A. C. Bento Appl. Phys. Lett., 96, 061909, 2010.

3. Z. He, Q. Liu, H. Hou, F. Gao, B. Tang, and W. Yang, ACS Appl. Mater. Interfaces, 27, 10878−10885, 2015.

4. H. Zheng, J. Z. Ou, M. S. Strano, R. B. Kaner, A. Mitchell, and K. Kalantar-zadeh, Adv. Funct. Mater. 21, 2175–2196, 2011.

5. M. Kapilashrami, Y. Zhang, Y. Liu, A. Hagfeldt, and J. Guo, Chem. Rev., 114, 9662−9707, 2014.

6. L. Li, Y. Zhang, X. Fang, T. Zhai, M. Liao, X. Sun, Y. Koide, Y. Bandoa and D. Golberg, J. Mater. Chem., 21, 6525−653, 2011.

7. H. Kim, J. Lee, N. Yantara, P. P. Boix, S. A. Kulkarni, S. Mhaisalkar, M. Grätzel, and N. Park, Nano Lett., 13, 2412−2417, 2013.

8. S. Mondal, R. R. Ghimire, and A. K. Raychaudhuri, App. Phys. Lett. 103, 231105, 2013.

9. R. R. Ghimire, S. Mondal, A. K. Raychaudhuri, J. App. Phys., 117, 10, 105705, 2015.

10. A. P. Alivisatos J. Phys. Chem. 1996, 100, 13226-13239.

11. M. A. Boles, D. Ling, T. Hyeon, and D. V. Talapin1, 5 Nat. mater., 15, 141-153, 2016.

12. X. Chen, S. S. Mao, Chem. Rev., 107, 2891-2959, 2007.

13. G. Xi, Y. Yan, Q. Ma, J. Li, H. Yang, X. Lu, and C. Wang, Chem. Eur. J., 18, 44, 13949-13953, 2012.

14. C. Wang, R. Sun, X. Li, Y. Sun, P. Sun, F. Liu, G. Lu, Sen. Act. B, 204, 224–230, 2014.

15. K. Nakata, A. Fujishima, and Photobio. C: J. Photochem. Rev. 13 169– 189, 2012.

16. C. Wang, X. Li, C. Feng, Y. Sun, G. Lu, Sen. Act. B, 210 75–81, 2015.

17. J. Tian, Z. Zhao, A. Kumar, R. I. Boughton and H. Liu, Chem. Soc. Rev., 43, 6920, 2014.

18. S. S. Shendagea, V. L. Patilb, S. A. Vanalakarb, S. P. Patila, N. S. Haralea, J. L. Bhosaled, J. H. Kim, P. S. Patil, 240, 426-433, 2017.

19. N. L. Xiaoqing, G. C. Yang, F. X. J. W. X, Su, 223, 743-749, 2016.

20. Z. Zhanga, M. Haqa, Z. Wena, Z. Yea, L. Zhua, App. Surf. Sci. 434 891–897, 2018.

21. F. Wang, C. D. Valentin, and G. Pacchioni, J. Phys. Chem. C, 115, 8345–8353, 2011.

22. P. Roussel, P. Labbe and D. Groult, Acta Crystallogr., Sect. B: Struct. Sci, 56, 377, 2000.

23. T. Guo, M. S. Yao, Y.H Lin, and C. W. Nan Cryst. Eng. Comm., 17, 3551–3585, 2015.

24. E. K. H. Salje, S. Rehmann, F. Pobell, D. Morris, K. S. Knightk, T. Herrmannsdorfer and M. T. Dove, J. Phys.: Condens. Matter 9 6563–6577, 1997.

25. S. Pokhrel, J. Birkenstock, A. Dianat, J. Zimmermann,M. Schowalter, A. Rosenauer, L. C. Ciacchi and L. Madler, Cryst. Eng. Comm., 17, 6985–6998, 2015.

26. B. Gerand, G. Nowogrocki, J. Guenot, and M. Figlarz, J. Solid State Chem., 29,429434, 1979.

27. R. Huang, Y. Shen, L. Zhao, M. Yan, Adv. Powder Tech., 23, 211–214, 2012.

28. Z. Chen, Y. Peng, F. Liu, Z. Le, J. Zhu, G. Shen, D. Zhang, M. Wen, S. Xiao, C. P. Liu, Y. Lu, and H. Li, Nano Lett, 15, 6802−6808, 2015.

29. X. Wang, H. Zhang, L. Liu, W. Li, P. Cao Mat. Letters, 130, 248–251, 2014.

30. S. Balaji, Y. Djaoued, A. S. Albert, R. Z. Ferguson, and R. Bruning, Chem. Mater., 21, 1381–1389, 2009.

31. I. M. Szilagyi, J. Madarasz, G. Pokol, P. Kiraly, G. Tarkanyi, S. Saukko, J. Mizsei, A. L. Toth, A. Szabo, and K. Varga-Josepovits, Chem. Mater., 20, 4116–4125, 2008.

32. M. Breedon, P. Spizzirri, M. Taylor, J. du Plessis, D. McCulloch, J. Zhu, L. Yu, Z. Z. Hu, C. Rix, W. Wlodarski, and K. Kalantar-zadeh, Crys. Growth & Design, 10, 1, 2010.

33. D. Y. Lu , J. Chen , H. J. Chen , L. Gong , S. Z. Deng , N. S. Xu , Y. L. Liu , Appl. Phys. Lett., 90, 041919, 2007.

34. P. J. Desre, Nanostruct. Mater., 8 , 687, 1997.

35. M. Boulova, G. Lucazeau, J. Solid State Chem., 167, 425-434, 2002.

36. M. Righettoni, S. E. Pratsinis M. Res. Bultn. 59, 199–204, 2014.

37. C. Ng, C. Ye, Y. H. Ng, and R. Amal, Crys. Growth & Design, 10, 8, 2010.

38. A. Polaczekt, M. Pqkatai and Z. Obuszko, J. Phys., Condens. Matter 6, 7909-7919, 1994.

39. J. Song, Z. F. Huang, L. Pan, J. J. Zou, X. Zhang, and L. Wang, ACS Catalyst., 5, 6594−6599, 2015.

40. V. O. Makarov & M. Tronteljb J. Euro. Ceram. Soc., 16, 791-794, 1996.

41. M. Gillet a, K. Aguir , C. Lemirea , E. Gillet , K. Schierbaumb, Thin Solid Films, 467, 239–246, 2004.

42. M. Gerosa, C. Di. Valentin, G. Onida, C. E. Bottani, and G. Pacchioni J. Phys. Chem. C 120, 11716−11726, 2016.

43. M. Landmann, E. Rauls and W. G. Schmidt, J. Phys., Condens. Matter, 24, 195503, 2012.

44. O. Carp, C.L. Huisman, A. Reller, Progress in Solid State Chem., 32, 33–177, 2004.

45. M. Cargnello, T. R. Gordon, and C. B. Murray, Chem. Rev., 114, 9319−9345, 2014.

46. F. Ninga, Y. B. Hea, B. Li, H. Dua, D. Zhai, F. Kanga, J. Alloys and Comp. 513, 524–529, 2012.

47. D. Reyes-Coronado, G. Rodrıguez-Gattorno, M. E. Espinosa-Pesqueira, C. Cab, R. de Coss, and G. Oskam, Nanotech. 19, 145605, 2008.

48. M. Niederberger, M. H. Bartl, and G. D. Stucky, Chem. Mater., 14, 4364-4370, 2002.

49. Z. Zhang, X. Zhong, S. Liu, Dongfei Li, and Mingyong Han, Angew. Chem., 117, 3532–3536, 2005.

50. X. Han, Q. Kuang, M. Jin, Z. Xie, and L. Zheng, J. Am. Chem. Soc., 9, 131, 3152–3153, 2009.

51. Q. Zhang, S. J. Liu and S. H. Yu, J. Mater. Chem., 19, 191–207, 2009.

52. J. Joo, S. G. Kwon, T. Yu, M. Cho, J. Lee, J. Yoon, and T. Hyeon, J. Phys. Chem. B, 109, 15297-15302, 2005.

53. C. S. Kima , B. K. Moonb, J. H. Parka, B. C. Choib , H. J. Seob, J. Cryst., Growth, 257, 309–315, 2003.

54. S. K. Gullapalli, R. S. Vemuri, and C. V. Ramana, Appl. Phys. Lett. 96, 171903, 2010.

55. A. Hjelm , C. G. Granqvist , J. M. Wills, Phys. Rev. B, 54, 2436, 1996.

56. A. D. Yoffe, Adv. Phys., 42, 173, 1993.

57. R. A. May, L. Kondrachova, B. P. Hahn, and K. J. Stevenson, J. Phys. Chem. C, 111, 18251-18257, 2007.

58. M. T. Chang, L. J. Chou, Y. L Chueh, Y. C. Lee, C. H. Hsieh, C. D. Chen, Y. W. Lan, and L. J. Chen, Small, 3, 4, 658–664, 2007.

59. P. M. Woodward, A. W. Sleight , T. Vogt, J. Solid State Chem.,131, 9, 1997.

60. D. Davazoglou, A. Donnadieu, Thin Solid Films, 147, 131, 1987.

61. R. B. Goldner , P. Norton, K. Wong, G. Foley, E. L. Goldner, G. Seward , R. Chapman, Appl. Phys. Lett., 47 , 536, 1985.

62. W. Wang, A. Janotti, and Chris G. V. d. Walle, J. Mater. Chem. C, 4, 6641-6648, 2016

63. K. Thummavichai, Y. Xia, Y. Zhu, Prog. Mat. Sci., 88, 281–324, 2017.

64. F. O. Arntz, R. B. Goldner, B. Morel, T. E. Hass, K. K. Wong, J. Appl. Phys., 67, 3177, 1990.

65. H. Kamal, A. A. Akl, K. Abdel-Hady, Physica B, Condens. Mat., 349, 192, 2004.

66. C. G. Granqvist, Sol. Energ. Mater. Sol. C, 32, 369, 1994.

67. T. Nanba, M. Ishikawa, Y. Sakai, Y. Miura, Thin Solid Films, 445, 175, 2003.

68. D. Dini, F. Decker, E. Masetti, J. Appl. Electrochem., 26, 647, 1996.

69. C. G. Granqvist, Sol. Ener. Mat. & Sol. Cells, 60, 201, 262, 2000.

70. T. Yoshimura, J. Appl. Phys., 57, 3, 1985.

71. K. Aguir, C. Lemire, D.B.B. Lollman, Sens. Act., B, 84, 1–5, 2002.

72. R. R. Ghimire and A. K. Raychaudhuri, Appl. Phys. Lett., 110, 052105, 2017.

73. W. Wang, X. Pan, W. Dai, Y. Zeng and Z. Ye, RSC. Adv., 6, 32715-32720, 2016.

74. B. Yang, P. R. F. Barnes, W. Bertrama and V. Luca, J. Mater. Chem., 17, 2722–2729, 2007.

75. S. Hullavarad, N. Hullavarad, D. Look, B. Claflin, Nanoscale Res Lett., 4, 1421–1427, 2009.

76. L. You, Y. F. Sun, J. Ma, Y. Guan, J.M. Sun, Y. Du, G.Y. Lu, Sens. Act., B, 157, 401-407, 2011.

77. Y. F. Sun, S. B Liu, F. L. Meng, J.Y. Liu, Z. Jin, L. T Kong and J. H. Liu, Sensors, 12, 2610-2631, 2012.

78. H. G. Moon, Y. S. Shim, D.H. Kim, H.Y. Jeong, M. Jeong, J.Y. Jung, Sci. Rep., 2, 588, 2012.

79. M. Ahsan, M.Z. Ahmad, T. Tesfamichael, J. Bell, W. Wlodarski, N. Motta, , Sens. Act. B, 173, 789-796, 2012.

80. S. Vallejos, T. Stoycheva, P. Umek, C. Navio, R. Snyders, C. Bittencourt, et al., Chem. Commun, 47, 565-567, 2011.

81. S. Vallejos, P. Umek, T. Stoycheva, F. Annanouch, E. Llobet, X. Correig, et al., Adv. Funct. Mater., 23, 1313-1322, 2013.

82. S. Kim, S. Park, S. Park, C. Lee, Sens. Act. B, 209, 180-185, 2015.

83. W. Yan, M. Hu, P. Zeng, S. Ma, M. Li, Appl. Surf. Sci., 292, 551-555, 2014.

84. L. Saadi, C.L. Mauriat, V. Oison, H. Ouali, R. Hayn, Appl. Surf. Sci., 293, 76-79, 2014.

85. Y. Li, W. Luo, N. Qin, J. Dong, J. Wei, W. Li, et al., Angew. Chem. Int. Edit., 53, 9035-9040, 2014.

86. T.A. Ho, T.S. Jun, Y.S. Kim, Sens. Act. B, 185, 523-529, 2013.

87. S. Luo, G. Fu, H. Chen, Z. Liu, Q. Hong, Solid State Electron., 51, 913- 919, 2007.

88. H. Xia, Y. Wang, F. Kong, S. Wang, B. Zhu, X. Guo, Sens. Act. B, 134, 133-139, 2008.

89. J. Li, X. Liu, J. Cui, and J. Sun, ACS Appl. Mater. Interfaces, 7, 10108−10114, 2015.

90. Z. Guo, M. Li, and J. Liu, Nanotech, 19, 245611, 2008.

91. J. H. Lee, Sen. Act. B, 140, 319–336, 2009.

92. S. Roy Moulik, A. Maity, M. Pal, M. Pradhan and B. Ghosh, Indian Patent Filed No. 201731017087 dated: 16/05/2017

93. Y. T. Hsieh, M. W. Huang, C. C. Chang, U. S. Chen, H. C. Shih, Thin Solid Films, 519, 1668–1672, 2010.

94. Yoon Ho Choa, Yun Chan Kang b, Jong-Heun Leea, Sen. and Act. B, 176, 971–977, 2013.

95. C. C. Chena, C. H. Cheng, C. K. Lin, Ceram. Int., 39, 6631–6636, 2013.

96. Z. Jiao, X. W. Sun, J. Wang, L. Ke, and H. V. Demir, J. Phys. D: Appl. Phys., 43, 285501, 2010.

97. F. D. Maggio, M. Ling, A. Tsang, J. Covington, J. Saffell, and C. Blackman, J. Sens. Sens. Syst., 3, 325–330, 2014.

98. M. C. Rao, J. Non-Oxide Glas. Vol. 5, No. 1, 2013.

99. S. Shuklaa, S. Chaudhary A. Umar, G. R. Chaudharya, S. K. Mehta, Sens. Act. B, 196, 231–237, 2014.

100. P. Huang, M. M. Ali Kalyar, R. F. Webster, D. Cherns, and M. N. R. Ashfold, Nanoscale, 6, 13586, 2014.

101. J. R. Morber, Y. Ding, M. S. Haluska, Y. Li, J. P. Liu, Z. L. Wang, and R. L. Snyder, J. Phys. Chem. B, 110, 21672-21679, 2006.

102. Y. Sun, G. M. Fuge, M. N. R. Ashfold, Chem. Phys. Lettrs., 396, 21–26, 2004.

103. S. Weia, J. Lianb, H. Wua, Mat. Charact., 61, 1239–1244, 2010.

104. Q. Suna, F. Xiaoa, S. Renb, Z. Donga, J. Wanga, X. Sua, Ceram. Intn., 40, 11447–11451, 2014.

105. Y. Li, Y. Guo, Y. Li, X. Zhou, Electrochem. Acta , 200, 29-36, 2016.

106. I. Ahmed, A. Fakharuddin, Q. Wali, A. R. B. Zainun, J. Ismail, R. Jose, Nanotech., 26, 105401– 10540, 2015.

107. H. Zhanga, J. Yang, D. Li, W. Guo, Q. Qin, L. Zhu, W. Zheng, Appl. Surf. Sci., 305, 274–280, 2014.

108. M. Yoshimoto, K. Shimozono, T. Maeda, T. Ohnishi, M. Kumaga, Jpn. J. Appl. Phys., 34 L688, 1995.

109. T. Inoue, T. Ohsuna, Y. Obara, Y. Yamamoto, M. Satoh and Y. Sakurai, Jpn. J. Appl. Phys. 32 1765, 1993.

110. J. An, Y. B. Kim, J. Park T. M. Gür, and F. B. Prinz, Nano Lett., 13, 4551−4555, 2013.

111. B. Ghosh, K. Das, and A. K. Raychaudhuri, J. Appl. Phys. 109, 083934, 2011.

112. H. Lv, X. Xu, H. Liu, R. Liu, Q. Liu, W. Banerjee, H. Sun, S. Long, L. Li & M. Liu, Sci. Rep., 5, 7764, 2015.

Chapter 2

Synthesis and characterization of binary oxide thin films and nanostructures

In this chapter, a detailed description on the procedures for synthesis of binary oxide (e.g. WO_3, TiO_2) thin film and nanostructures (nanorods (NRs), nanowires (NWs) and nanotubes) along with their characterization has been provided. Binary oxide thin film and nanostructures were synthesized using Pulsed Laser Deposition (PLD) and Wet chemistry synthesis (hydrothermal) techniques. The PLD targets of binary oxides were prepared by conventional solid state synthesis method. The as prepared nanostructured samples of binary oxides were characterized using X-ray Diffraction (XRD), Scanning Electron Microscope (SEM), Transmission Electron Microscope (TEM) for structural and morphological analysis. Energy Filter TEM (EFTEM), Electron Energy Loss Spectrometry (EELS)/Energy dispersive X-ray Spectrometry (EDS) were used for chemical compositional characterization. The details of the techniques and characterization tools along with characterization results have also been provided in this chapter.

2.1 Introduction

Binary oxides are among the important materials in the field of physics, chemistry and material science for their various applications [1-6]. One can synthesize and fabricate large diversified binary oxide nanostructures, thin films, devices using different synthesis techniques. Binary oxide nanostructures are studied for their optical, electrical, gasochromic properties [4, 7-8] and energy harvesting applications (like solar cell) [9]. The way to achieve the application efficiency of these materials is to synthesize highly crystalline, atomically sharp interface nanostructures. The quality of nanomaterial not only depends on its crystallinity and crystal structure but also upon the chemical composition, size, shape, phase purity and fabrication of the device. Till date many techniques have been used for binary oxide nanostructure synthesis like template-assisted [10-11], chemical [12], seed [13], hydrothermal [14] growth, Pulsed Laser Deposition (PLD) [15] and anodic oxidation method [16]. Among all these synthesis methods, the wet chemistry (hydrothermal) method and PLD have shown outstanding performance in obtaining highly ordered nanostructured materials with controllable dimensions and stoichiometry. In this thesis PLD method and hydrothermal method were used as a tool for the synthesis of binary oxides (WO_3, TiO_2) thin film and vertically aligned nanowires/nanorods and nanostructures.

This thesis mainly focused on the synthesis, modification of synthesis and study of physical properties of low dimensional nanostructures of the binary oxide materials like TiO_2, WO_3, etc. Among the unique properties of these materials, the movement of electrons and holes in these semiconductors are primarily governed by the well-known quantum confinement, and the transport properties related to phonons and photons that are largely affected by the size and geometry of the materials [17-20]. Thus in this thesis a way to synthesize, a large surface area for these materials, was performed in such a way that it is beneficial in facilitating interaction between the devices and the interacting media, which strongly depends on the surface area of the material. A number of studies have demonstrated that the performance of oxide nanostructures can be improved by alternating the structural and dimensional parameters of the binary oxide [21-22]. This thesis also provides interesting information about how to modify size, shape, crystal structure and surface morphology of binary oxide and how it affects the physical properties of the materials under study.

2.2   Synthesis of binary oxide thin film and nanostructures

Synthesis of binary Oxide (WO$_3$, TiO$_2$) thin film and nanostructures was done using Pulsed Laser Deposition technique (PLD) and hydrothermal method. The effect of tuning of growth parameters and crystallographic structures of substrate on the size, shape, crystal structure and morphology tailoring of binary oxide has been investigated.

2.2.1 Solid state synthesis: making of target for Pulse Laser Deposition (PLD)

One of the oldest and conventional methods used to prepare the bulk polycrystalline target (pellet) material of oxide samples for PLD is solid state synthesis [23]. In this synthesis method the solid chemicals are well mixed, pressed to form pellet and kept at high temperature for solid state reaction to take place.

To prepare the tungsten oxide target the starting material was Tungsten oxide (WO$_3$) powder (> 99% pure, Sigma Aldrich). The powder was mixed and crushed in Agate mortar and pestle using an organic solvent (e.g acetone, alcohol) followed by annealing at 300°C for 6hrs. Afterwards the powder was pressed at high pressure (50 Pascal) to form pellet followed by sintering at 1100°C for 10hrs.

2.2.2 Pulsed Laser Deposition (PLD)

Pulsed Laser Deposition (PLD) is an established technique for thin film deposition [24]. High quality thin films can be grown with required size considering application using Radio Frequency (RF)-magnetron Sputtering [25], Plasma process [26], Chemical Vapor Deposition (CVD) [27], Sol-gel method [28], Electro-chemical process [29], Molecular Beam Epitaxy (MBE) [30] etc. Thin films of WO$_3$ on different substrates (e.g. Silicon Oxide (SiO$_2$/Si (SO)), SrTiO$_3$ (STO) etc.) using PLD technique has been prepared in this thesis. In PLD high intensity pulsed laser beam has been ablated (interact) on the material surface of the rotating target to evaporate and ionize it. In this process a high intensity plasma plume is produced over a small area near the target but away from the target surface. This plasma plume got condensed as it reached the substrate placed at 180^0 to the target and produced thin films. The depositions were carried out in presence of background gas such as Oxygen, Argon or in

ultrahigh vacuum, depending upon the requirement [24]. Fig. 2.1 shows the schematic diagram of PLD instrument. Sample crystallinity, surface morphology and composition of the deposited film depend on the rate of deposition of the target material.
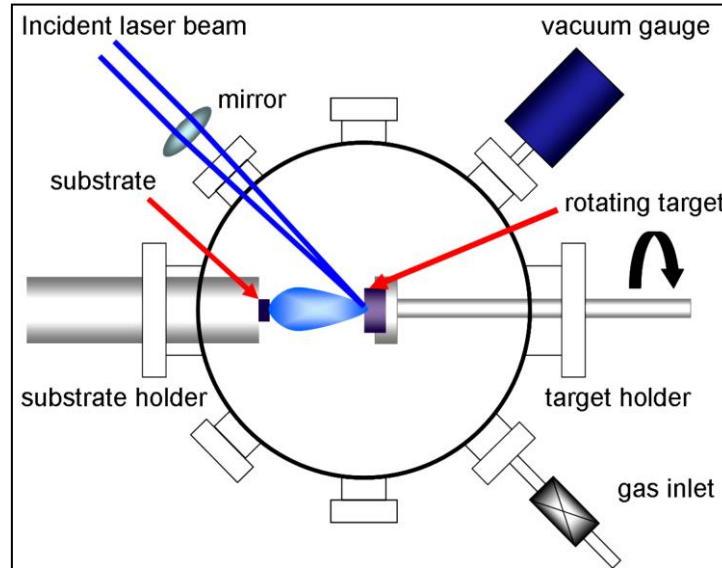
Figure 2.1: *Schematic diagram of a PLD instrument set up. Source Ref. [31].*

In PLD the deposition process depends on few important parameters. Those are:

(a) Substrate temperature (T_S):

Substrate temperature during and after the deposition of the film plays an important role in thin film growth as it is related to the nucleation density of the material. High temperature increases the nucleation density whereas low temperature decreases it, however after deposition; temperature controls the film stoichiometry and homogeneity.

(b) Background pressure:

After obtaining the high vacuum and before deposition a background pressure is created using Argon for inert atmosphere or Oxygen to maintain oxygen stoichiometry for oxide samples.

(c) Target-substrate distance:

Substrate to target distance is usually kept at 5-6cm for growing standard thin film; however one can adjust it to grow desirable nanostructured thin film or nanorods arrays.

(d) Substrate type:

Lattice mismatch between target material and substrate plays an important role on the surface morphology and nucleation of the target material.

(e) Laser energy:

Depending upon the laser energy or Laser fluence (Joule/Cm^2), laser pulse time, duration of laser deposition, the quality, thickness and stoichiometry of the thin films varies. The growth of thin film in PLD occurs in three steps;

1. Interaction between the laser pulses and the target material leads to formation of molten target material, which gets vaporized and gives a highly forward directed plasma plume.
2. Interaction of forward directed plasma plume with the ambient gas (both physically and chemically).
3. Condensation of the plume onto a substrate where the thin film is nucleated and growth occurs.

Although PLD is well known for thin film deposition, in this thesis it has been utilized and standardized for non-trivial synthesis of nanostructures of desired shape and size, like nanowire/nanotube etc. along with thin film deposition.

2.2.2.1　*WO₃ thin film synthesis in PLD*

In this thesis work WO_3 thin films were grown on Silicon Oxide/Silicon (SiO_2/Si (SO)) and $SrTiO_3$ (STO) substrates using our lab PLD set up of 248nm wavelength KrF excimer laser (Fig. 2.2).
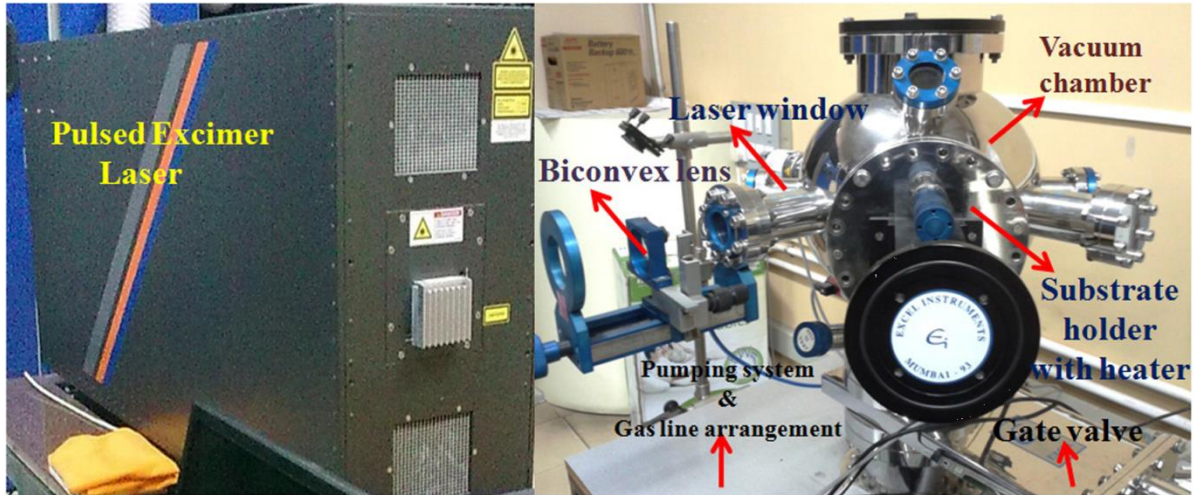
Figure 2.2: *PLD setup in our lab. Source ref. [32].*

The laser parameters (Viz. Laser Fluence, repetition rate, deposition time) were tuned keeping background oxygen pressure at 30 Pascal's and substrate temperature at 500- 600°C. The growth parameters for those films deposition are provided in Table 2.1[33]:

Table 2.1: *PLD parameters for WO₃ thin films deposition*

Substrates	*SO, STO*
Laser Fluence	*2-4J/cm²*
Oxygen Partial Pressure	*30pascals*
Laser Frequency	*1-3Hz*
Deposition Time	*30min*

The Field Emission Scanning Electron Microscope (FESEM) image of nanocrystalline thin film and needle like structure film are shown in Fig. 2.3. The grain size for thin film on SO is very small (10-20nm) whereas, in case of STO film becomes needle like structure [33].
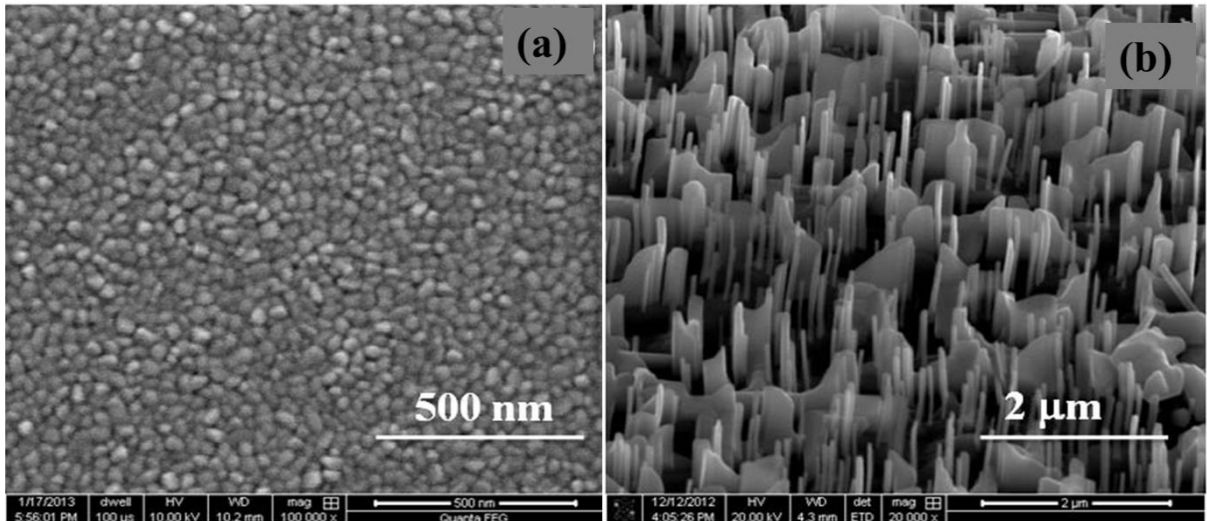
Figure 2.3: *FESEM images of WO₃ (a) nanocrystalline film on Si/SiO₂ substrate, (b) needle like structured film on SrTiO₃.*

X-ray Diffraction (XRD) analysis shows monoclinic structure of the film grown on SO (a= 5.4Å) (Fig. 2.4(a)), monoclinic structure with orientation along (100) plane for needle like structure grown on STO (a= 3.905A°) (Fig. 2.4(b)), and possible due to very close lattice matching with WO₃ (a = 3.81A°) [33].
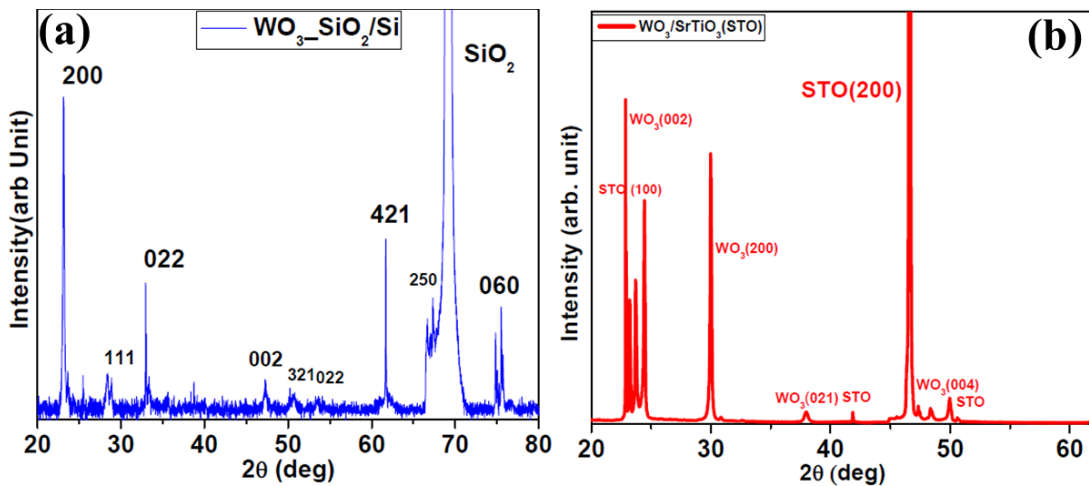
Figure 2.4: *X-ray Diffraction pattern of (a) nanocrystalline film on SO (b) needle like structured film on STO.*

Thus controlling of PLD parameter and choice of substrate to tune the surface morphology as well as crystal structure has been standardized in this thesis work. Further analysis on effect of surface morphology modification upon physical property of binary oxide nanostructure has been explored and will be discussed along with probable explanation in chapter 4.

2.2.2.2 *WO₃ nanowires synthesis in PLD*

Nanowires (NWs) of binary oxide were grown by different methods starting from chemical route, hydrothermal, solvothermal route etc. till date [34-36]. PLD is well known for thin film deposition; but growth of vertically aligned nanowires by PLD is a non-trivial method. This type of growth has been standardized and discussed in details in this thesis chapter and the growth mechanism discussed in chapter 3. There are reports, on the growth of binary oxide (ZnO, WO_3) nanowires in last 2 decades [37-38], but no detailed analysis about interface physics study using spatially resolve tools and techniques to understand the possible growth mechanism has been performed, till date except ours.

In this thesis work the growth technique was optimized exploiting PLD method, to grow vertically aligned nanowires (NWs), which is a well-known technique for thin film growth only. The growth parameters in PLD are optimized to grow vertically aligned nanowires of binary oxide (e.g. WO_3) on platinized silicon (Pt/SiO_2/Si (Pt/Si)) substrate. The general PLD parameters are given below in Table 2.2 for nanowires growth [39].

Table 2.2: *PLD parameters for growth of WO₃ nanowires on Pt/SiO₂/Si (Pt/Si)*

Laser Energy	110-200mJ
Laser Fluence	2-4J/cm^2
Oxygen Partial Pressure	30-150pascals
Substrate Temperature	600-700°C
Deposition Time	20-30min

FESEM images shows that with the change of PLD laser energy (110-200mJ) surface morphology of nanostructure grown on Pt/Si changes from thin film (110mJ) (Fig. 2.5(a)) to partially/non-aligned nanowires (Fig. 2.5(b)) and finally vertically aligned nanowires (200mJ) (Fig. 2.5(c)) [39]. XRD pattern of thin film (Fig. 2.6(a)), partially/non-aligned nanowires (Fig. 2.6(b)) and vertically aligned nanowires (Fig. 2.6(c)) has been shown, which depicts change in crystal structure from monoclinic (thin film) to orthorhombic (partially/non-aligned nanowires) and finally oriented orthorhombic (vertically aligned nanowires) along (002) plane [39]
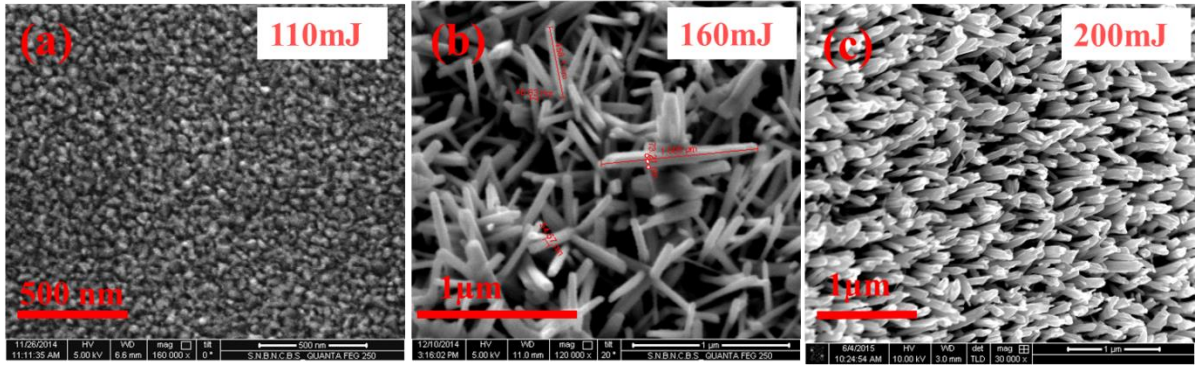
Figure 2.5: *FESEM images show the changes in the morphology of WO₃ with the increase in the laser energy (a) nanocrystalline thin film, (b) partially/non-aligned nanowires, and (c) vertically aligned nanowires.*
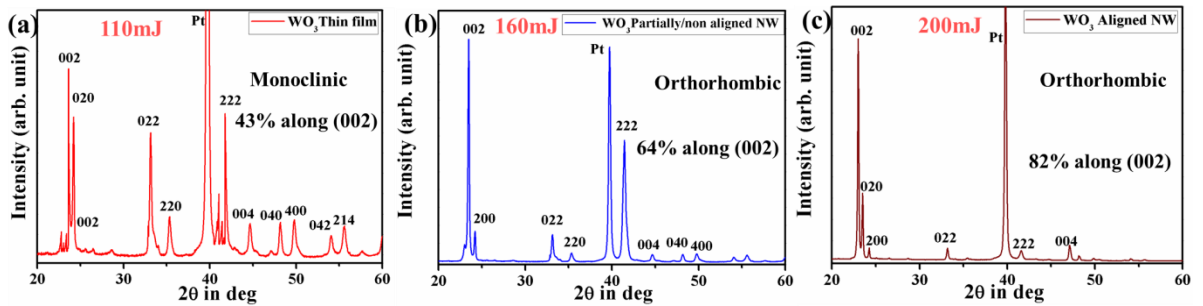
Figure 2.6: *XRD pattern of WO₃ grown Pt/Si substrate (a) thin films, (b) partially/non-aligned nanowires and (c) vertically aligned nanowires.*

The degree of orientation (f_{hkl}) has been calculated from equation (2.1) [40]. Here I_{hkl} is relative intensity of the (002) plane.

$$f_{hkl}(\%) = \frac{I_{hkl}}{\sum I_{hkl}} \times 100 \ldots \ldots \ldots \ldots \ldots (2.1)$$

In case of nanocrystalline thin film (110mJ) the crystal structure is monoclinic with only 43% orientation along (002) plane (Fig. 2.6(a)), whereas for partially/non-aligned NWs (160mJ) crystal structure changes to orthorhombic with 64% orientation along (002) plane (Fig. 2.6(b)). Finally for vertically aligned NWs (200mJ) although the crystal structure remains orthorhombic but NWs become highly oriented (83%) along (002), which is clear from the increased intensity of the XRD peak (Fig. 2.6(c)).

There are reports [41-42] on modification of crystal structure with variation of growth/or post annealing temperature, but in this thesis, laser fluence/energy has been considered as an important parameter for growth of vertically aligned nanowires instead of growth temperature. Thus from the above observation one can say, that laser energy can also effect

the crystal phase and degree of orientation of WO_3 nanostructure. Once the growth technique was standardized for vertically aligned nanowires, analysis for the understanding of underlying physics behind this type of growth mechanism has been done using cross sectional Transmission Electron Microscopy (X-TEM) study. X-TEM study of interface physics and microstructure will be discussed in Chapter 3 section 3.2.

2.2.3 Wet chemistry (hydrothermal) synthesis of binary oxide nanostructures:

Hydrothermal method is a one-step synthesis process to grow mainly nano-materials of different chemical compounds in aqueous solutions at pressure higher than 1atm kept in sealed thick walled stainless steel cylinders, called autoclave, which can withstand high temperature and pressures for prolonged period of time. The synthesis of binary oxide nanostructures are performed in the autoclave consisting of a steel vessel with Teflon beaker kept inside it (Fig. 2.7).

Figure 2.7: *Autoclave with Teflon beaker*

The reaction time, temperature, pressure, and pH level of the solution can be controlled as desired. The Autoclave can withstand highly corrosive solvents at high temperature and pressure for a longer reaction. In this thesis work (i) Titanium Oxide (TiO_2) nanorods on

fluorine doped tin oxide coated glass substrate (FTO) and Pt/Si (ii) Tungsten oxide (WO_3) nanotubes assembly were grown using hydrothermal synthesis route.

2.2.3.1 *Hydrothermal synthesis of TiO_2 nanowires*

TiO_2 nanorods (TiO_2 NRs) on Fluorine Doped Tin Oxide coated glass (FTO) and Pt(111)/SiO_2/Si (Pt(111)/Si) substrate by hydrothermal method using autoclave have been synthesized in this thesis. Initially a solution of DI water, Hydrochloric acid (35-40 Vol. %) and Titanium 4-butaoxide in a ratio 1:1:0.03 has been taken and stirred to get a clear homogeneous solution. Then the solution was transferred to a Teflon linear autoclave and the substrates (FTO, Pt/Si) separately was placed at 45° degree angle inside it and sealed. The autoclave was kept at 150^oC for 20hrs and after cooling it the synthesized nanorods (NRs) were cleaned in Deionized (DI) water [43]. Also to provide better nucleation site for the growth of TiO_2 NRs, a very thin TiO_2 seed layers was grown on both substrates (FTO, Pt/ Si) using PLD (parameters provided in table 2.3) before the hydrothermal synthesis. The grown NRs were characterized using FESEM and XRD which shows NRs were grown in FTO whereas nanoflowers like structure grown on Pt/Si.

Table 2.3: *PLD parameters for seeding layer of TiO_2 growth on FTO and Pt(111)/Si*

Laser Fluence	2-3J/cm^2
Oxygen Partial Pressure	30 pascals
Substrate Temperature	200-300^oC
Deposition Time	10-15min
Laser frequency (repetition rate)	2-3Hz

FESEM image in Fig. 2.8(a) shows that dense, vertically aligned NRs grown on TiO_2seeded/FTO. The cross sectional view (vertical view of the substrate with NRs) in FESEM shows that the TiO_2 NRs are vertically aligned on TiO_2 seeded/FTO substrates are tetragonal in shape with a square top surface and the average dia~100-200nm and length ~6-8μm (Fig. 2.8 (b)) [43]. The adhesion with the FTO substrate was possible due to the seeding layer and the small lattice mismatching of rutile TiO_2 (a = b = 4.593 Å) [44] and the tetragonal FTO (a = b = 4.687 Å) [45], which provide epitaxial nucleation and pure rutile TiO_2 growth.
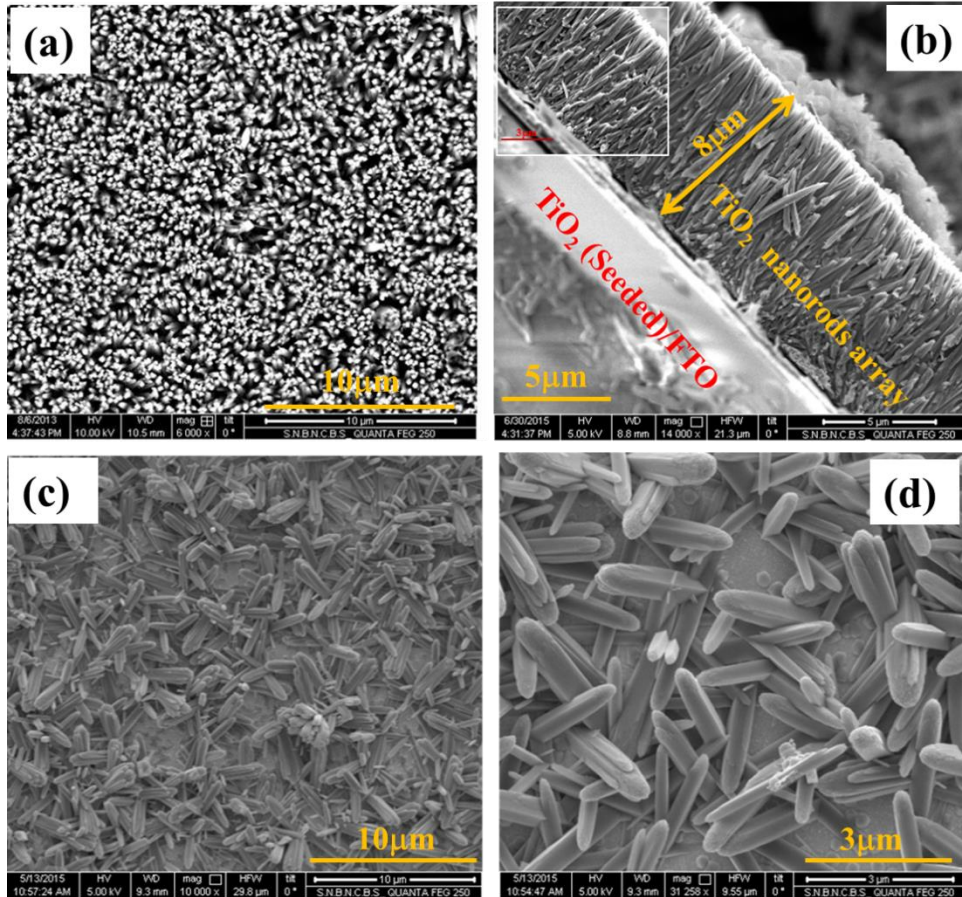
Figure 2.8: *TiO$_2$ nanorod array grown on TiO$_2$seeded/FTO substrate (a) FESEM image top view, (b) Cross sectional view (inset: enlarge view of the nanorod/substrate interface); TiO$_2$ nanorods grown on TiO$_2$seeded/Pt(111)/Si substrate (c) FESEM images Top view and (d) High magnification FESEM image of the nanorods .*

In Fig. 2.8(c) and (d) shows FESEM images of TiO$_2$ NRs on Pt/Si with an average diameter of ~3 μm having numerous flowerlike aggregates composed of broad and thin single nanoribbons with different orientations. Although seeding layer of TiO$_2$ was present on Pt/Si but no strong adhesion was observed in grown NRs due to strong lattice mismatch and structural change of substrate (Pt, Cubic, a = 3.9 Å) [43]. XRD pattern in Fig. 2.9(a) for NRs on TiO$_2$ seeded/FTO confirms pure rutile phase and tetragonal structure (a = b = 4.593 Å, c = 2.961 Å, ICSD Ref: 01-070-7347 21-1276) [44]. The degree of orientation as derived from equation (2.1) shows NRs are partially (40%) oriented along (002) plane. XRD pattern in Fig. 2.9(b) of the NRs on TiO$_2$seeded/Pt(111)/Si substrate shows polycrystalline nature along with a mixture of anatase (A) (33%) and rutile (R) (67%) phases (ICSD Ref: 01-070-7347 21-1276, 01-070-6826 21-1272) [43].
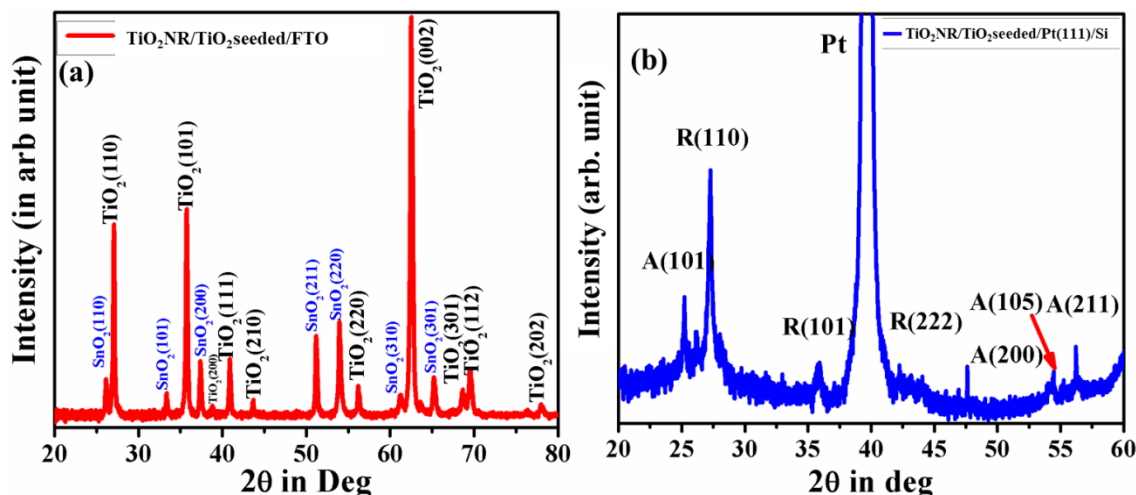
Figure 2.9: *XRD pattern of TiO_2 nanorods on (a) TiO_2 seeded/FTO (b) TiO_2 seeded/Pt(111)/Si.*

The percentage of phase content was calculated using equation (2.2), where P stands for phase and P_r and P_a are rutile and anatase phase respectively [40].

$$P = \frac{I_{hkl}}{\sum I_{hkl}(P_r + P_a)} \times 100\% \ldots\ldots\ldots\ldots\ldots\ldots..(2.2)$$

The growth of NRs was accelerated due to presence of seeding layer but, the huge lattice mismatch and structural change (Pt, Cubic, a = 3.9 Å) of substrate (Pt(111)/Si) results in growth of mixed phase (anatase, rutile) of TiO_2.

Further microstructural analysis has been performed in TEM. The surface chemistry analysis to understand the possible growth dynamics and propose a probable growth mechanism behind these different growths of NRs on two conducting substrates has been performed using spatially resolved chemical analysis technique. The TEM and surface chemistry analysis will be explained in chapter 3 section 3.3.

2.2.3.2 *Hydrothermal synthesis of WO₃ nanotubes*

WO₃ nanotubes assembly has been synthesized using hydrothermal method. Sodium tungstate (Na_2WO_4, $2H_2O$) powder (0.99 g) and 1.2 gm of Sodium bisulfate ($NaHSO_4$, H_2O) powder were dissolved in a 40 ml of deionized water by stirring the mixture vigorously for 1 hour in room temperature till the solution become clear. The obtained solution then transferred into teflon-lined autoclave and heated to 180° C for 36 hours followed by natural cooling to room temperature. The as prepared product was filtered and washed sequentially

by DI water and ethanol, then dried overnight in air. In Fig. 2.10(a) FESEM image shows WO_3 nanotubes are grown as assemble and Fig. 2.10(b) shows FESEM image of single WO_3 nanotube having a diameter ~100-200nm and length~ 2-3mm. XRD pattern in Fig. 2.10(c) shows hexagonal crystal structure of the grown nanotubes. Further microstructural analysis and investigation on gas transport property was carried out with these nanotubes, which will be discussed in chapter 5.
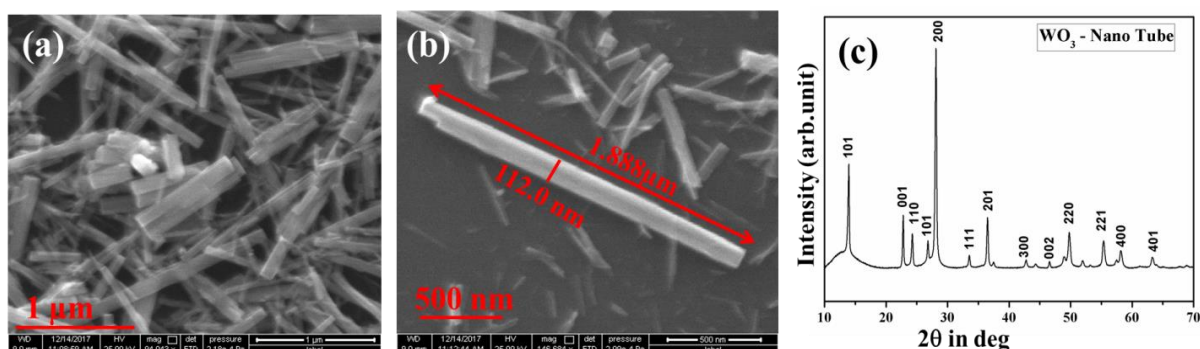
Figure 2.10: *FESEM images (a) WO_3 nanotubes assembly, (b) Single WO_3 nanotubes, and (c) XRD pattern of WO_3 nanotubes.*

2.3   Characterization tools and techniques

The synthesized samples are characterized using X-ray Diffraction (XRD), Scanning Electron Microscope (SEM), and Transmission Electron Microscope (TEM) for structural and morphological characterization. The Film and substrate interface was characterized in TEM using Cross Sectional lamella preparation technique (will be discussed in Chapter 3). In this section different characterization tools and techniques along with the basic principle of the techniques will be discussed.

2.3.1 Structural and surface morphology characterization tools and techniques

The crystal structures of the synthesized samples were studied using XRD technique. Surface morphology and atomic structure imaging was done using SEM and TEM respectively.

2.3.1.1 *X-ray Diffraction (XRD) technique*

X-ray Diffraction is a commonly used technique to understand the crystallographic structure and phase of a material. The X-rays are generated using the cathode ray generation technique and it is filtered and collimated to focus on the sample. The interaction between the sample and the X-ray beam produces constructive interference satisfying the well-known Bragg's Law, Eq. 2.3 (Fig 2.11(a)) [46].

$$2dsin\theta = n\lambda .... (2.3)$$

Where θ = angle of incidence of the X-ray beam, d = Distance between two layer of atoms, λ= Wave length of the X-ray, n =integer, the equation can be well explained with using schematic diagram in Fig. 2.11(a).
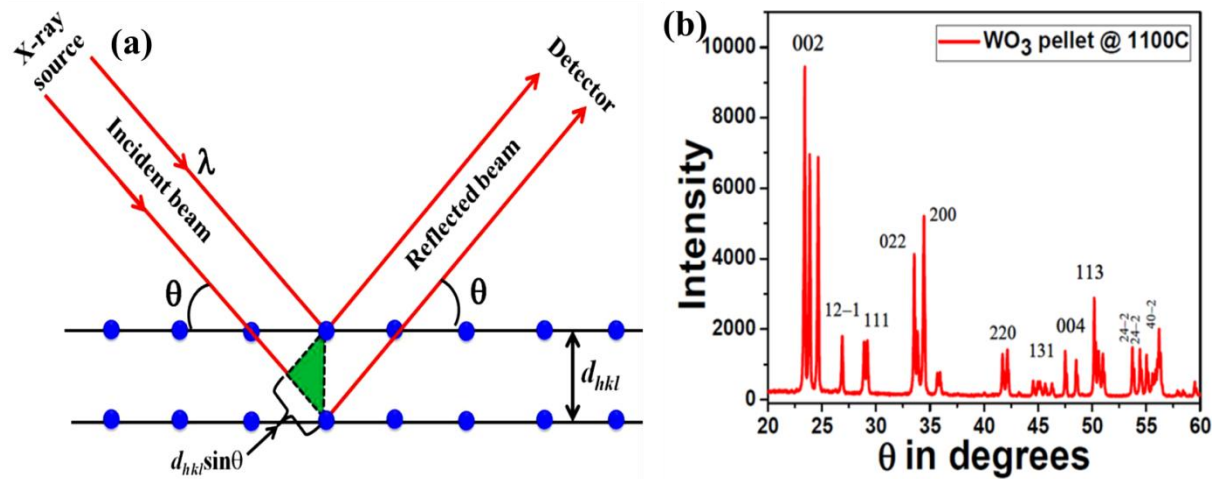
Figure 2.11: *(a) Bragg's Law schematic diagram. Source ref. [46], (b) XRD data of WO$_3$ pellet sintered @1100°C.*

To know the crystallographic orientation and phase formed of synthesized samples, experimental data are compared with standard JCPDS (Joint Committee on Powder Diffraction Standard) or ICSD (Inorganic Crystal structure database), which provides the crystallographic plane indices (h, k, l) [48].

In this thesis work Panalytical X'PertPro XRD instrument having Cu$_{K\alpha1}$ source with wavelength 1.5405 Å at an accelerating voltage of 45 kV and 40 mA current has been used for analysis. This system follows the Bragg-Brentano geometry *(θ-2θ)* i.e. the sample holding stage is fixed while the X –ray tube rotates at -θ^o/min and the detector rotates at a +θ^o/min. The X−rays have sufficient energy to penetrate the solid sample and provide information

about their crystallographic structures. The detector used in this system is PIXEL detector, which has quite a low signal to noise ratio [49]. In Fig 2.11(b) we have shown the XRD pattern of WO_3 pellet (PLD target).

2.3.1.2 *Scanning Electron Microscope (SEM)*

One of the finest advancement in the field of microscopy is the invention of Scanning Electron Microscope (SEM), which not only provides magnified, high resolution image of a sample but also gives information about the surface topology, shape, size, size distribution and nature of the sample down to sub micrometer level [50].

The basic working principal of SEM involves the generation of electron beam either thermionically or by field effect emission from the electron source and it is focused with the help of electrostatic and magnetic lenses inside an ultrahigh vacuum path (Fig. 2.12(a)). The generated electron beam is then moved over the sample following raster scanning technique. The interaction between the sample and the electron beam produces different signals (Fig. 2.12(b)) among which Secondary Electron (SE), Backscattered Electron (BSE) are collected by the corresponding detector placed inside the microscope sample chamber and produce images. The detector in SEM for the detection of secondary electrons is the Everhart-Thornley Detector (ETD) [50]. It consists of a Faraday cage which helps to accelerate the electrons towards a scintillator. The scintillator produces current due to falling electrons upon it and the current is amplified using photomultiplier for the read out. To avoid charging effect and possible sample damage during analysis of non-conducting samples, a thin gold coating is applied on the surface of the samples. X-rays generated during the electron beam and specimen interaction are also used for elemental composition analysis using the method Energy Dispersive X-ray (EDX) spectrometry and the most commonly used detector for it is EDAX. In this thesis work FEI Quanta 200 SEM and Quanta 250FEG, Field emission SEM (FESEM) has been used for sample analysis. Fig. 2.12(c) is the WO_3 pellet SEM image showing the grain size of the Pellet around 10-15μm.
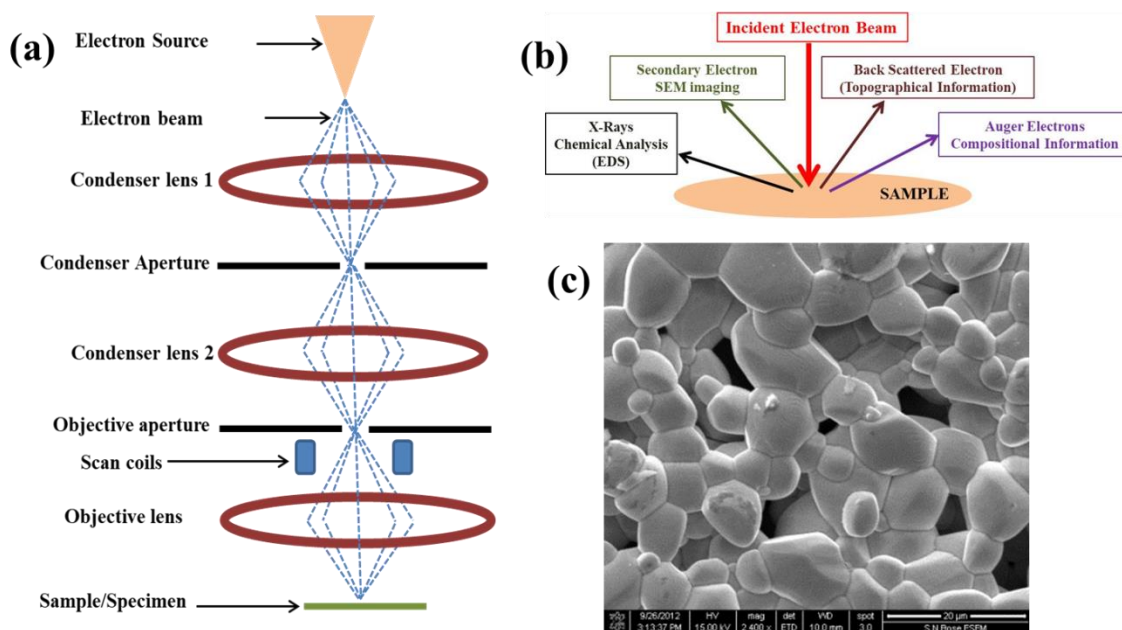
Figure 2.12: *(a) Schematic ray diagram of SEM instrument, (b) Schematic diagram of specimen and electron beam interaction inside SEM, and (c) SEM image of WO$_3$ pellet.*

2.3.1.3 *Dual Beam Focused Ion Beam – FESEM (FIB-FESEM)*

Dual Beam FIB- FESEM consists of Focused Ion Beam (FIB) as well as electron beam (e-beam) and both are capable of producing images of the samples like a SEM [51]. Apart from imaging, Dual Beam system mainly utilized for lithography for nano device fabrication and sample preparation (Cross Sectional lamella) for High Resolution TEM analysis with the help of other additional accessories. The essential component is same as standard FESEM. The FIB part consists of Liquid Metal Ion Source (LMIS) and electrostatic lenses. Other important accessories are Gas Injection System (GIS), Omniprobe needle [51]. Fig. 2.13(a) shows Helios 600 Dual beam instrument of our lab setup at our clean room and Fig. 2.13(b) shows the inside view of the sample chamber of that FIB-FESEM. While preparing the cross sectional lamella of WO$_3$/Pt/SiO$_2$/Si (WO$_3$/Pt/Si) thin film, vertically aligned and Partially/non-aligned nanowires arrays, FIB FESEM has been utilized and parameters were standardization to avoid possible damage and implantation of Gallium (Ga) ions on the lamellas. Cross Sectional lamella preparation using FIB-FESEM will be discussed in Chapter 3 section 3.2.1. A brief description of LMIS, GIS has been provided below.
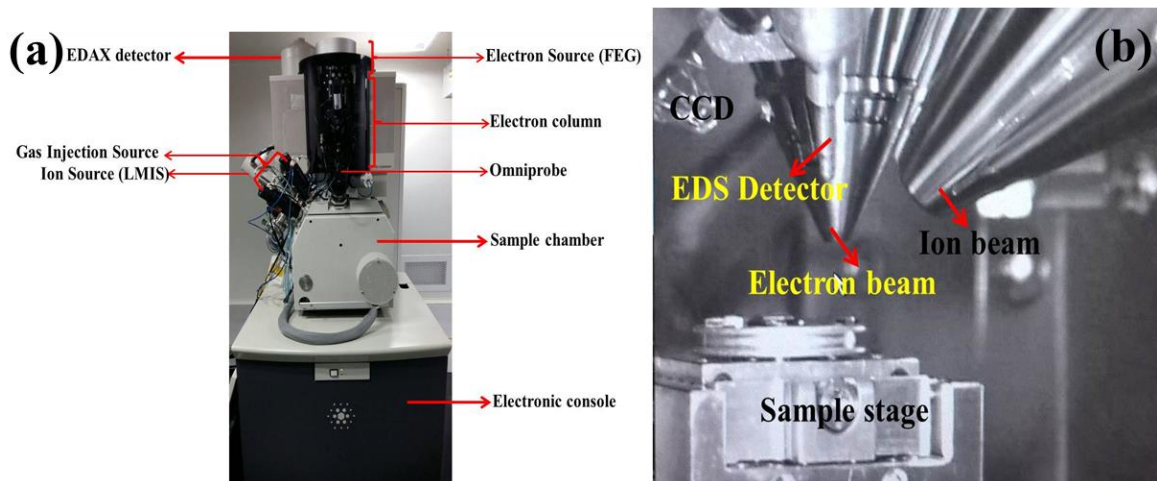
Figure 2.13: *(a) Helios 600 Dual beam FIB-FESEM System (lab set up) (b) Image of all the probes inside the FIB-FESEM sample chamber.*

I.   *Liquid Metal Ion Source (LMIS)*

Typically a LMIS consists of the liquid metal ion (Gallium) which upon heating (50-60ºC) comes out through the needle tip of the source as gallium ions which interacts with the nanowires (samples) [51]. Ion source is mainly used for etching, patterning, deposition and imaging in FIB.

All the uses of the ion source were possible with the help of electrostatic lenses which controls the beam shape, focusing and formation of the beam.

The cutting/etching/milling of the $WO_3/Pt/Si$ sample from different angle, direction, and deposition of protective layer (mainly Pt in our case) during the lamella preparation was done using this Gallium LMIS FIB (will be discussed in Chapter 3 section 3.2).

II.   *Gas Injection Source (GIS)*

It is a non-volatile compound filled source which upon heating vaporizes the compound containing particular materials, which need to be deposited or used for etching like Platinum (Pt), Tungsten (W), Insulator (SiO_x) for deposition on different samples in nano regime [51]. It is one of the crucial accessories during cross sectional lamella preparation as it has been used for depositing a protective layer, welding purpose or sometimes for etching out the sample layer.

III. *Omniprobe needle (Omniprobe)*

A Typical Omniprobe needle is made of stainless steel material and the tip has to be sharpened using FIB as per the requirement during lamella lift off. It is specially used along with the GIS to lift off the lamella from the bulk $WO_3/Pt/Si$ and attaching it to the TEM-grid during cross sectional lamella preparation.

2.3.1.4 *Transmission Electron Microscope (TEM)*

The Transmission Electron Microscope (TEM) is the 1st generation development in electron microscopy. The schematic diagram of a standard TEM (ray optics) and image of (lab setup) shown in Fig. 2.14(a, b) respectively. The source for TEM is also same as SEM (described in section 2.3.1.2). The voltage applied for the generation of the electron beam is 200kV or 300kV. The beam generated has been focused using a set of electromagnetic condenser lenses (C1, C2) and corresponding apertures. The image was formed with the help of objective lenses and aperture, finally the image is projected on to the Charge couple device camera (CCD)/Fluorescent screen using projector and intermediate lenses [52].

The sample used for TEM analysis must be thin ($< 200nm$) enough to pass the electron for the formation of image as the name suggests. Fig. 2.14(c) shows schematic diagram of the specimen-beam interaction in TEM, where the beam suffers three type of collision as it passes through the sample, a) Elastic collision, b) Inelastic collision, c) Transmitted beam and all this interaction follows the Bragg's law. The beam suffers elastic collision and the un-scattered beam (transmitted beam) is the source for the 2D image formation in TEM.

The image formed with both beams (elastic, inelastic) is called the **Bright Field image (BF)** and image formed only using the inelastically scattered beam (diffracted beam) is called the **Dark Field image (DF)**. The dark field imaging can only be used for crystalline samples as it gives information about crystal structure and defects.

During the beam specimen's interaction in accordance to Bragg's law the beam suffers diffraction after passing through the sample and this diffracted beam forms a pattern on the back focal plane just beneath the objective lens, which can give information about the atoms and crystal plane called electron diffraction Pattern (ED). The image formed using this pattern/beam at very high magnification is called **High Resolution TEM image (HRTEM image).**
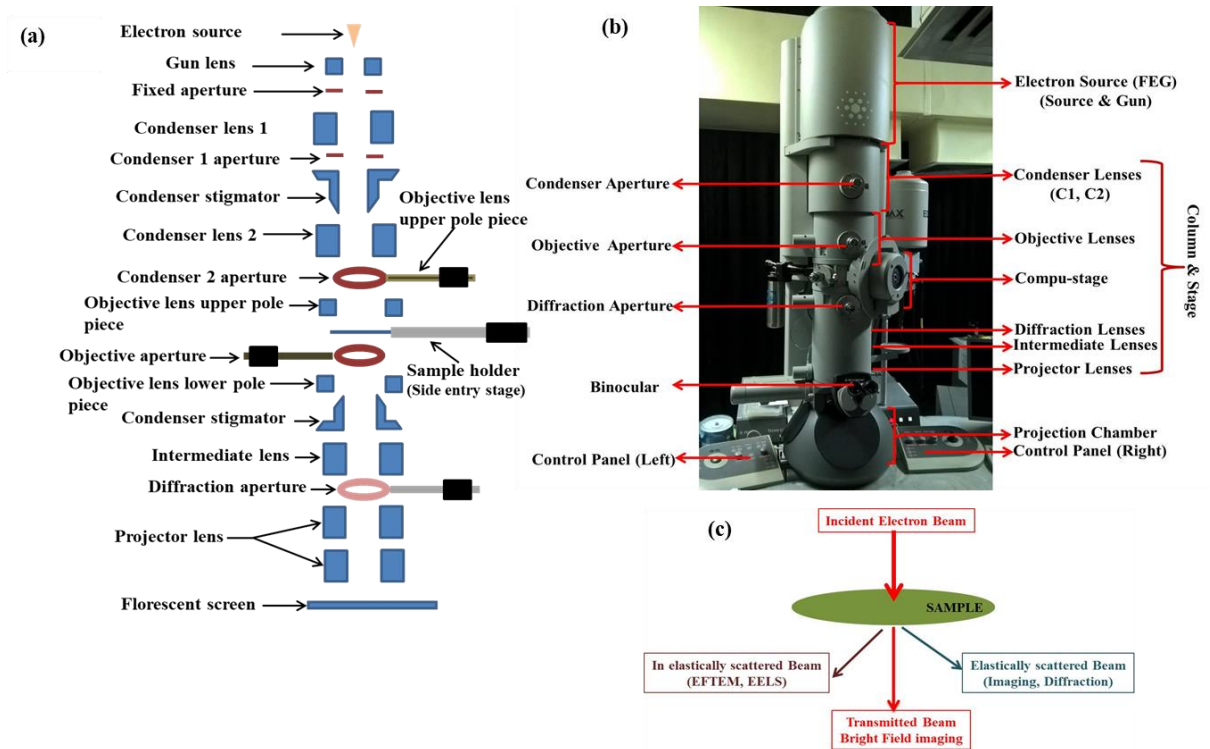
Figure 2.14: *(a) Schematic ray diagram of TEM instrument, (b) TEM setup in our lab (c) schematic diagram of specimen beam interaction in TEM.*

The ED pattern when taken selecting a specific area of the sample using diffraction aperture is called **Selective Area Electron Diffraction (SAED),** which gives information about the crystal plane orientation (h, k, l) of a sample. Also HRTEM image gives information about the inter-planer/interatomic spacing (d), which corresponds to specific (h, k, l)

In conventional TEM imaging, images were obtained using static electron beam passing through the sample and collected below the sample onto a charge couple device (CCD) camera. In the **Scanning TEM (STEM)** mode, using a set of deflecting coils just above the objective lens the beam was moved/scanned through the sample and the transmitted diffracted beam was collected using a special Annular Dark Field Detector (ADF). Fig. 2.15 shows the schematic ray diagram of STEM mode. The image obtained in this detector is a dark field STEM image. In this mode highly diffracted transmitted beam also gets collected using High Angle Annular Dark Field Detector (HAADF) and HAADF-STEM image obtained [52]. In our lab TEM, we have STEM with HAADF detector. The STEM mode was deployed for understanding interface physics of vertically aligned WO_3 nanowires grown in non-trivial PLD technique will be discussed in Chapter 3 section 3.2.2.
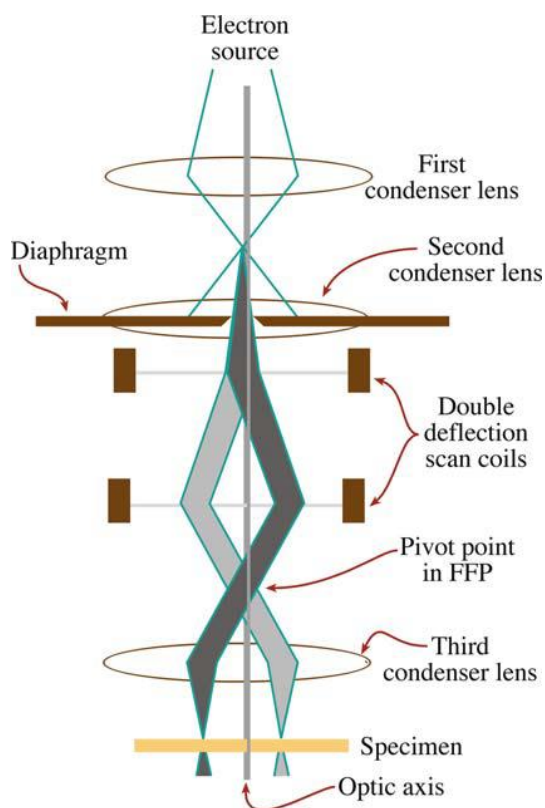
Figure 2.15: *Schematic ray diagram of STEM mode in TEM. Source ref. [52].*

The TEM images taken of our samples are prepared with two different methods (a) TEM sample preparation on Cu-grid (b) Cross Sectional TEM (X-TEM) sample preparation.

(a) TEM sample preparation on Cu-grid

In this method the sample (powder samples) are dispersed in Methanol, ethanol, toluene, benzene, water etc. and 100-200µl of the dispersed solution is drop casted on top of a carbon coated Cu-grid, and dried overnight. The Cu-grid is a Cu made mesh within 3.05mm diameter with typically 200-400 mesh in it with a thin layer of carbon (10-20nm thickness).

(b) Cross sectional TEM sample preparation (X-TEM sample)

In this method bulk sample materials, thin films on substrates which are not prepared in powder form are cut into 3mm disk and the center portion of the sample are made thin using ion beam milling technique. Dual beam technique will be utilized to cut the samples in slices

vertically top to down direction using Helios 600 dual beam (will be discussed in chapter 3 section 3.2.1).

In this thesis TEM images were taken using 200 kV Tecnai G^2 TF-20 ST instrument. Fig. 2.16(a) shows TEM bright field image of a nanorod of TiO_2 (diameter ~ 100 nm) grown in hydrothermal method on FTO (discussed in section 2.2.3.1). Fig. 2.16(b) shows the SAED pattern and Fig. 2.16(c) shows the HRTEM image and the lattice spacing measured from both the images found to be 3.2Å which well matched with TiO_2 tetragonal crystal structure.
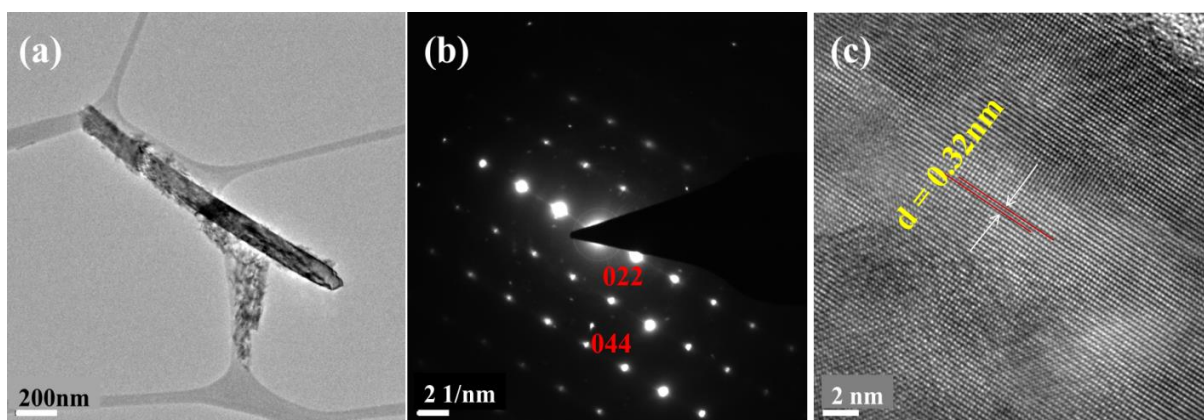
Figure 2.16: *TiO$_2$ nanorod (a) TEM Bright Field image, (b) SAED pattern, (c) HRTEM image showing lattice planes.*

2.3.2 Elemental compositional analysis techniques

To study the compositional homogeneity, stoichiometry, quantification of the element of the grown thin films and nanostructures we have used several spatially resolved tools and techniques like Energy dispersive X-ray (EDX) spectrometry, Energy TEM (EFTEM), Electron Energy Loss Spectrometry (EELS). With the help of these advanced chemical analysis tools the elemental composition of our samples down to nanometer level was analyzed.

2.3.2.1 *Energy Dispersive X-ray (EDX) spectrometry*

Energy-dispersive X-ray (EDX) spectrometry analysis is done with the sample inside a SEM or TEM [52].

In this technique characteristic X–rays are generated during specimen and high energy electron beam (30keV, 200keV etc.) interaction (Fig. 2.14(c)) due to excitation of an inner

shell electron of the sample to a vacant higher energy. The emitted X-rays are denoted by the transition to shell viz. K, L and M lines.

In EDX analysis, localized information about the elemental composition of the sample can be obtained and it is possible to map the elements on that small region to form an image having particular compositional element (EDX-mapping) (will be discussed in detail in chapter 3). Here EDAX make EDX detector attached to FESEM and TEM/STEM have been utilized for compositional analysis. In Fig. 2.17 shows the EDX data of TiO_2 nanorods grown in hydrothermal route. The spectrum confirms absence of impurity in the nanorods.
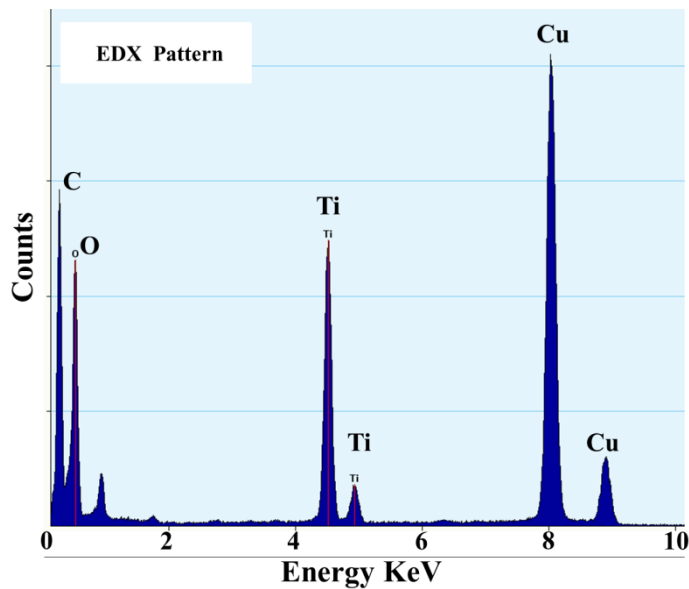
Figure 2.17: *TEM-EDX spectrum of TiO_2 nanorods grown by hydrothermal synthesis method.*

2.3.2.2 *Gatan Imaging Filter (GIF)*

Gatan Imaging Filter (GIF) is specially designed detector capable of splitting (using magnetic prism) the transmitted (through thin (thickness ≤ 100 nm) specimen) electron beam as per the energy in a TEM (100-300keV energy) and producing spectrum as well as image from a sample. The spectrum produced by GIF using the inelastically scattered electron is called Electron Energy Loss spectrometry (EELS) and the image formed using the same is called Energy Filtered TEM (EFTEM) Image [52-54]. In Fig. 2.18 schematic diagram of GIF operation and modes are shown [54]. GIF in general works in two mode (a) Spectroscopy or EELS mode and (b) Imaging or EFTEM mode. In EFTEM mode information about the

stoichiometry of the nanorod elements was observed and in EELS mode the oxygen deficiency and the effect of it on samples was also analyzed.
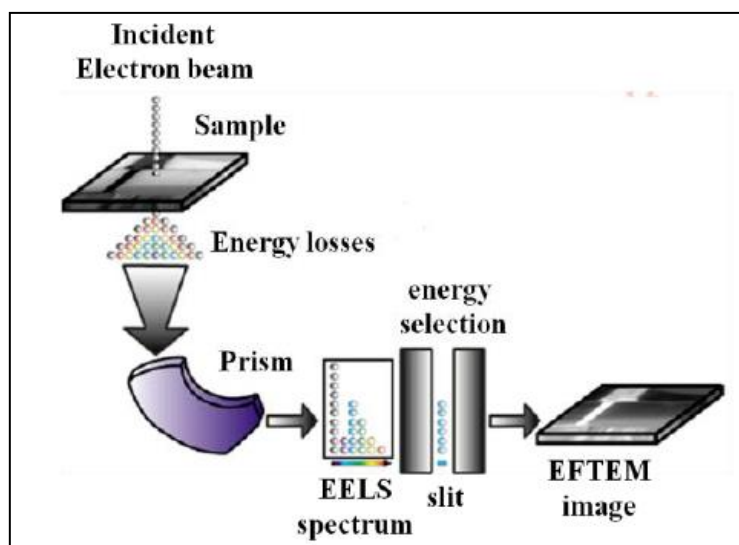
Figure 2.18: *Schematic diagram of a GIF detector. Source Ref. [54].*

A. *Electron Energy Loss Spectroscopy (EELS):*

Electron energy loss spectroscopy (EELS) is one of the advanced techniques used for chemical analysis of TEM samples, which also provide information about valance state of the elements present in the compound [52, 54-55]. In EELS, the energy distribution of inelastically scattered electrons was measured.

A typical EEL spectrum consists of three parts: (i) *Zero-loss peak at 0 eV, (ii) Low-loss region (Plasmon Peaks) (< 100eV), (iii) High-Loss region or core loss region (>100eV).*

In Fig. 2.19 (a, b) all three regions of EEL spectrum taken on a single nanorod of TiO_2, grown by hydrothermal method (discussed in section 2.2.3.1), has been shown. In high loss region a specific minimum energy must be transferred from the incident electron to the expelled inner-shell electron for the ionization of atoms, which leads to ionization edges in the spectrum due to energy losses that are characteristic for an element. Compared to the Plasmon generation, the inner-shell ionization is much less probable process, leading to a low intensity of the peaks. The representation of the high-loss region is often strongly enhanced

due to the low intensity. The background noise effects high loss region which need to be taken care to maintain better signal to noise ratio in EELS.
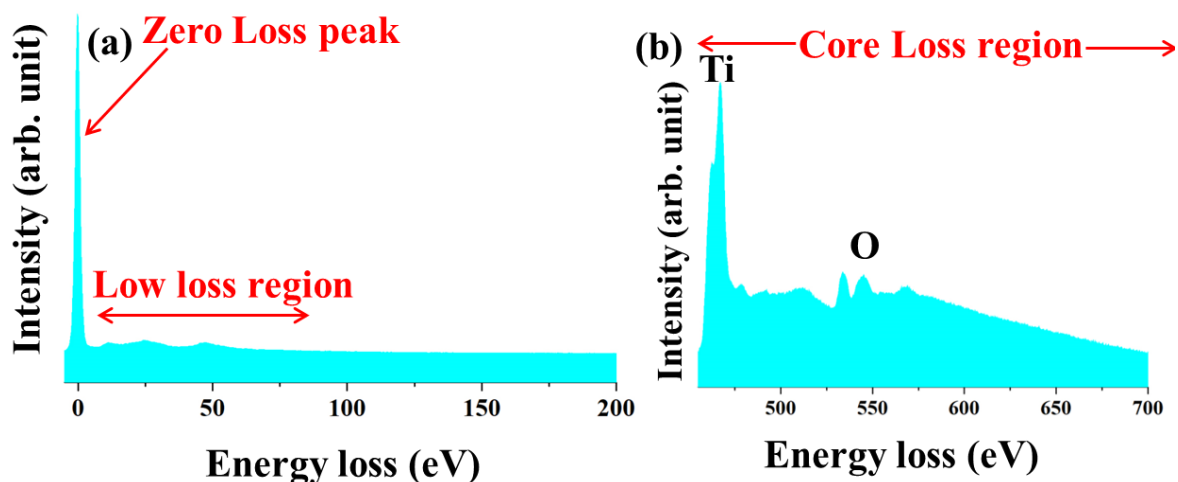
Figure 2.19: *EEL Spectrum (taken on a TiO₂ nanorod) (a) Zero loss peak and low loss region, (b) Core loss region*

To cope up with the background signal a specially designed lacey carbon coated TEM grid was also utilized to minimize interference of carbon signal as a noise in the EELS signal. EELS have been utilized to understand role of surface chemistry in hydro thermally synthesized TiO_2 nanorods (discussed in section 2.2.3.1) and will be discussed in Chapter 3 section 3.3.

B. *Energy Filter TEM (EFTEM):*

In EFTEM mode images are produced from elastically scattered electrons of elements for providing information about the distribution of elements in the sample over the selected area (Region of interest). In this mode images formed only considering elastically scattered electrons called **Filtered image** (elastic image) which helps to discard contribution of highly scattered electrons and enhances image contrast. Image collected using elastic and inelastic signals is called **Unfiltered image**. To study the homogeneity of the elements present in the sample, an energy selecting slit is placed just after the magnetic prism to select specific core loss energy (for element) and project it on to the CCD camera to form the images (Fig. 2.18). The image aberrations are corrected using quadrupole and sextupole lenses (focusing and aberration correctors) in the GIF spectrometer [53]. GIF detector provides energy resolution (0.8eV) two order higher than EDX. The Gatan Quantum 963 GIF detector along with ultra-

high speed CCD camera was deployed for all the analysis of TiO_2 nanorods using HRTEM to understand the growth dynamics and will be discussed in chapter 3 section 3.3.

In Fig. 2.20 shows EFTEM images and elemental mapping taken on a single TiO_2 nanorod grown by hydrothermal synthesis (discussed in section 2.2.3.1) has been shown.
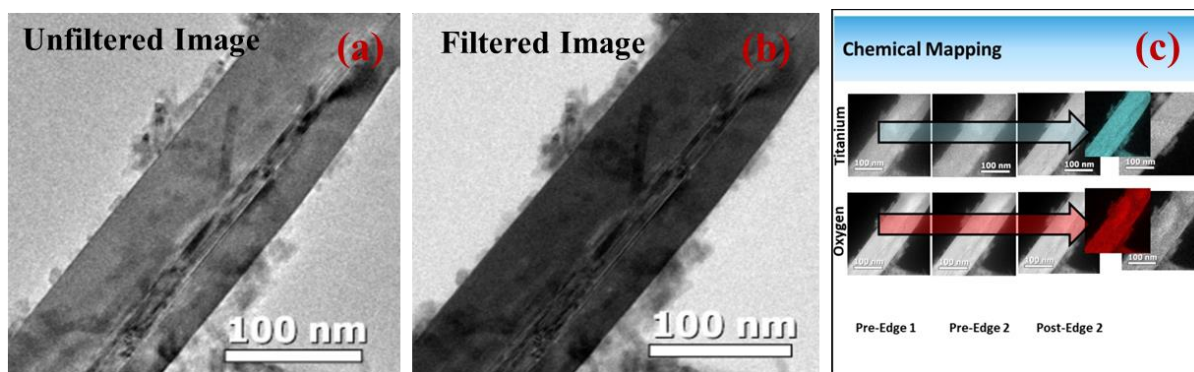
Figure 2.20: *EFTEM imaging and mapping taken on single TiO_2 nanorod grown by hydrothermal synthesis (a) Unfiltered image, (b) Filtered image, and (c) Chemical mapping.*

2.4 Conclusion

In this thesis chapter, demonstration about the synthesis of thin film and nanostructures of binary oxides (WO_3, TiO_2) has been provided. PLD and hydrothermal route has been used for the synthesis and growth parameters have been standardized to tune the size, shape, morphology of those binary oxides. Most importantly, PLD technique has been employed to grow vertically aligned nanowires of binary oxides though it is a well-known technique for thin film growth only.

All the characterization was done using advanced techniques/tools like XRD, SEM. The analysis provided information about the phase purity, high crystallinity, and surface morphology of the samples. The growth dynamics and possible growth mechanism further will be investigated using spatially resolved tools and technique in chapter 3.

Also the effect of modification of the size, shape and crystal structure on different physical property of binary oxides will be investigated in chapter 4 and 5 to provide new dimension to the application of binary oxide nanostructures.

Bibliography:

1. V. Oison, L. Saadi, C. L. Mauriat, R. Hayn, Sens. and Actuators B: Chem., 160, 505-510, 2011.

2. R. R. Ghimire and A. K. Raychaudhuri, Appl. Phys. Lett., 110, 052105, 2017.

3. J. Joo, S. G. Kwon, T. Yu, M. Cho, J. Lee, J. Yoon, and T. Hyeon, J. Phys. Chem. B, 109, 15297-15302, 2005.

4. Z. He, Q. Liu, H. Hou, F. Gao, B. Tang, and W. Yang, ACS Appl. Mater. Interfaces, 7, 20, 10878−10885, 2015.

5. M. Kapilashrami, Y. Zhang, Y. Liu, A. Hagfeldt, and J. Guo, Chem. Rev., 114, 9662−9707, 2014.

6. K. Thummavichai, Y. Xia, Y. Zhu, Progress in Mat. Sci., 88, 281–324, 2017.

7. W. Wu, J. Wu, and J. Chen, ACS Appl. Mater. Interfaces, 3, 2616–2621, 2011.

8. M. D'Arienzo, L. Armelao, C. Maria Mari, S. Polizzi, R. Ruffo, R. Scotti, and F. Morazzoni, J. Am. Chem. Soc., 133, 5296–5304, 2011.

9. H. Kim, J. Lee, N. Yantara, P. P. Boix, S. A. Kulkarni, S. Mhaisalkar, M. Grätzel, and N. Park, Nano Lett., 13, 2412−2417, 2013.

10. A. S. Attar, M. S. Ghamsari, F. Hajiesmaeilbaigi, Sh. Mirdamadi, K. Katagiri, K. Koumoto, J. Mat. Sc., 43, 17, 5924-5929, 2008.

11. R. Ganesan and A. Gedanken, Nanotech., 19, 025702. 2008.

12. T. Kasuga, M. Hiramatsu, A. Hoson, T. Sekino, K. Niihara, Langmuir, 14, 3160, 1998.

13. J. Song and S. Lim, J. Phys. Chem. C, 2, 111, 596–600, 2007.

14. Z. Jiao, X. Wei Sun, J. Wang, L. Ke and H. V. Demir, J. Phys. D: Appl. Phys., 43, 285501, 2010.

15. F. Mitsugi, E. Hiraiwa, T. Ikegami, K. Ebihara and R.K. Thareja, Jpn. J. Appl. Phys., 41, 5372-5375, 2002.

16. D. Gong, C.A. Grimes, O. K. Varghese, W. Hu, R. S. Singh, Z. Chen, E. C. Dickey, J. Mater. Res., 16, 3331, 2001.

17. A. P. Alivisatos, J. Phys. Chem., 100, 31, 13226-13239, 1996.

18. A. P. Alivisatos, Science, 271, 5251, 933-937, 1996.

19. C. Burda, X. Chen, R. Narayanan, M.A. El-Sayed, Chem. Rev., 105, 1025, 2005.

20. C. B. Murray, C. R. Kagan, M. G. Bawendi, Annu. Rev. Mater. Sci., 30, 545, 2000.

21. Y. Djaoued, S. Balaji and R. Bruning, J. Nanomater., 7, 674168, 2012.

22. H. Zheng, J. Z. Ou, M. S. Strano, R. B. Kaner, A. Mitchell and K. Kalantar-zadeh, Adv. Funct. Mater 21, 2175–2196, 2011.

23. C. V. Ramana, S. Utsunomiya, R. C. Ewing, C. M. Julien, and U. Becker, J. Phys. Chem. B, 110, 10430-10435, 2006.

24. Douglas B. Chrisey and Graham K. Hubler, "Pulsed Laser Deposition of Thin Films", John Wiley & Sons, 1994.

25. M. D. Giulio, D. Manno, G. Micocci, A. Serra, and A. Tepore, J. Phys. D:Appl. Phys., 30, 3211, 1997.

26. H. Kawasaki, T. Matsunaga, W. Guan, T. Ohshima, Y. Yagyu, and Y. Suda, J. Plasma Fusion Res., 8, 1431, 2009.

27. C. E. Tracy and D. K. Benson, J. Vac. Sci. Technol., A 4, 2377, 1986.

28. C. Santato, M. Odziemkowski, M. Ulmann, and J. Augustynski. J. Am. Chem. Soc., 123, 10639, 2001.

29. M. Deepa, A. K. Srivastava, and S. A. Agnihotry, Acta Mater., 54, 4583, 2006.

30. Haeni, J., Theis, C. and Schlom, D., J. of Electroceram., 4, 385, 2000.

31. K. Wang, "Laser Based Fabrication of Graphene" (Chapter-4), Mahmood Aliofkhazraei (Ed.), "Advances in Graphene Science", INTECH open science, 77-95, 2013.

32. R. Nath, "Investigation of novel electrical and magnetic properties of perovskite oxides", thesis submitted to University of Calcutta, 2015.

33. S. Roy Moulik, S. Samanta, and B. Ghosh, Appl. Phys. Lett., 104, 232107, 2014

34. J. Su, X. Feng, J. D. Sloppy, L. Guo, and C. A. Grimes, Nano Lett., 11, 203–208, 2011.

35. H. Wang, Y. Bai, Q. Wu, W. Zhou, H. Zhang, J. Li and L. Guo Phys. Chem. Chem. Phys., 13, 7008–7013, 2011.

36. H. G. Choi, Y. H. Jung, and D. K. Kim, J. Am. Ceram. Soc., 88, 6, 1684–1686, 2005.

37. Ye Sun, Gareth M. Fuge, Michael N.R. Ashfold, Chem. Phys. Lett., 396, 21–26, 2004.

38. P. Huang, M. M. Ali Kalyar, R. F. Webster, D. Cherns, and M. N. R. Ashfold, Nanoscale, 6, 13586, 2014.

39. A. Ghatak, S. Roy Moulik, B. Ghosh, RSC Adv., 6, 31705–31716, 2016.

40. A. Bose, T. Maity, S. Bysakh, A. Seal, S. Sen, Appl. Surf. Sci., 256, 6205, 2010.

41. T. Yanagida, T. Kanki, B. Vilquin, H. Tanaka and T. Kawai, J. Appl. Phys., 99, 053908, 2006.

42. S. B. Sun, Y. M. Zhao, Y. D. Xia, Z. D. Zou, G. H. Min and Y. Q. Zhu, Nanotech., 19, 305709, 2008.

43. S. Roy Moulik, A. Ghatak, B. Ghosh, Surf. Sci., 651, 175–181, 2016.

44. C.J. Howard, T.M. Sabine, F. Dickson, Acta Cryst., B, 47,462, 1991.

45. M. Abd-Lefdil, R. Diaz, H. Bihri, M. Ait Aouaj, F. Rueda, Eur. Phys. J. Appl. Phys., 38, 217, 2007.

46. B. D. Cullity, S. R. Stock, "Elements of X-ray Diffraction", Prentice Hall, 2001.

47. R. Basori, "Investigation of Growth, Electrical and Opto-electronic Transport in Nanowires of Charge Transfer Complexes", Thesis submitted to University of Calcutta, 2015.

48. http://www.icdd.com

49. PANanalytical B. V. Lelyweg, 1, 7602 EA Almelo, The Netherlands.

50. R. F. Egerton, "Physical Principles of Electron Microscopy: An Introduction to TEM, SEM and AEM", Springer, 2005.

51. Operation manual Helios nanolab 600 dual beam FESEM (www.fei.com)

52. D. B. Williams, C. B. Carter "Transmission Electron Microscopy A Textbook for Materials Science", Springer, 2009.

53. GIF operation manual gatan Inc. (www.gatan.com)

54. R. F. Egerton, Electron Energy-Loss Spectroscopy in the Electron Microscope, Third Edition, Springer, 1996.

55. R. F. Egerton, Rep. Prog. Phys., 72, 016502, 2009.

Chapter 3

Interface physics and surface chemistry analysis using advanced characterization tools

This chapter has been mainly focused on the study of interface physics analysis of binary oxide nanostructure (WO₃). The role of interface in case of WO₃ nanostructure has been investigated using advanced cross sectional sample preparation technique in a Dual Beam Focused Ion Beam (FIB)-FESEM based lithography. In order to have a detailed chemical analysis of the interface, Scanning Transmission Electron Microscopy (S-TEM) along with Energy Dispersive X-ray spectrometry mapping (STEM-EDX) has been employed. The growth mechanism involved in Pulse Laser Deposition (a type of Physical Vapour Deposition) method has been proposed with a possible model in detail. Beside this, the surface chemistry and effect of substrate on the growth of TiO₂ nanostructures (grown using wet chemistry route) was also explored down to single nanowire level using Energy Filtered Transmission Electron Microscopy/Electron Energy Loss Spectrometry (EFTEM/EELS) attached to TEM. The growth mechanism involved in this wet chemistry method has also been proposed with possible model. The study enhances the knowledge based on the role of interface as well as surface chemistry in case of binary oxide nanostructures during the growth of samples by both Physical Vapour Deposition and wet chemistry synthesis route respectively.

3.1. Introduction

$\mathbf{I}$n search of nano dimensional binary oxides with novel properties, many interesting synthesis method have been developed in the last few decades. Among different metal binary oxides, WO_3 and TiO_2 nanostructures have large variety of application in opto electronics, selective catalysis, environmental engineering and pigment devices, environmental purification by photocatalysis and dielectric materials [1-11]. The one dimensional WO_3, TiO_2 nanostructures (nanowires/nanorods) are more attractive for nano device fabrication because of their large surface to volume ratio which helps to felicitate interaction between devices and interacting media. Hence the nano dimension of the binary oxides and the surface area of the fabricated device will play an important role for the optimum performance of the device [12]. These wide ranges of applications are controlled by the physical properties of these binary oxides, which mainly depend on the crystal structure, surface morphology, chemical composition, and phase stability of the resulting structures [13, 14]. According to recent study WO_3 and TiO_2 nanostructures are grown using different growth techniques e.g. sputtering [15], sol-gel [16], evaporation [17], hydrothermal [18-20] etc. in assembled and array form. But the growth of highly crystalline, oriented and vertically aligned nanostructures growth over large surface area is still an open interesting area to explore.

Moreover, understanding of interesting physics arising out of the effect of nanostructure, substrate interface and surface chemistry on the growth process has been explored in detail in this chapter. This thesis chapter mainly on focused understanding of the vertically aligned WO_3 nanowires growth dynamics and a brief analysis on vertically aligned TiO_2 nanorods growth dynamics have also been provided. The chapter is aligned into two parts by explaining the role of interface as well as surface on the growth dynamics. In the first part the understanding of growth dynamics of the nanostructures of binary oxides (WO_3) has been carried out using Cross Sectional Transmission Electron Microscopy (X-TEM) analysis technique where role of nanostructure and substrate interface was observed. The X-TEM microscopic analysis was done on X-TEM sample (lamella), of the vertically aligned WO_3 and interface (nanowires and substrate interface), which was prepared using Dual Beam Focused Ion Beam –Field Emission Scanning Electron Microscope (FIB-FESEM). In the second part of the chapter the role of surface chemistry has been explored in case of TiO_2 nanostructures using Scanning-Transmission Electron Microscopy (STEM) along with Electron energy loss spectroscopy (EELS) study.

3.2. Interface physics analysis of WO$_3$ nanowires on Pt/SiO$_2$/Si

Pulsed laser deposition (PLD) technique, which is generally well known for thin film deposition was used to synthesize the WO$_3$ nanowires on Pt/SiO$_2$/Si (Pt/Si) substrates using different parameters (details described in chapter 2, section 2.2.2.2) [21]. Growth of nanowires using PLD is very rare and non–trivial. Growth of nanostructures of WO$_3$ using PLD and the study of nanowires and substrate using X-TEM study was not reported before. The growth parameters were controlled to standardize the technique to grow vertically aligned nanowires on substrate (details described in chapter 2, section 2.2.2.2). It has been observed that the increase in laser fluence modified the surface morphology of WO$_3$ from nanocrystalline thin film to highly oriented vertically aligned nanowires (NWs) has also been shown. The details of all the growth parameters in PLD during this synthesis have been provided in Table 3.1 below.

Table 3.1: <u>*PLD parameters for synthesis of WO$_3$ film and nanowires*</u>

PLD parameters	Nanocrystalline film	Partially/Non-aligned NW	Vertically aligned NW
Laser energy	110 mJ	160 mJ	200 mJ
Laser fluence	2 J cm^{-2}	3 J cm^{-2}	4 J cm^{-2}
Gas used	High purity oxygen (9	High purity oxygen (99.7%)	High purity oxygen (99.7%)
Oxygen partial pressure	30 pascal	30 pascal	30 pascal
Substrate temperature	600 °C	600 °C	600 °C
Post annealing	600 °C for 30 min	600 °C for 30 min	600 °C for 30 min
Laser shots	20 min	20 min	20 min
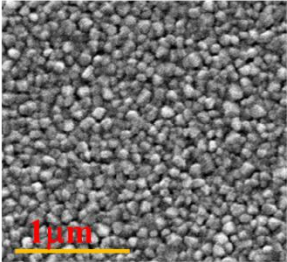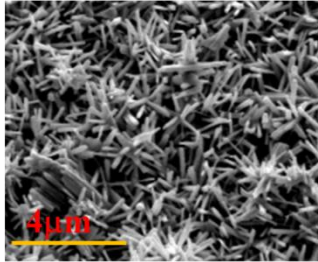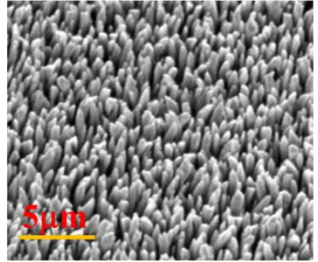
The reason behind the growth and the growth mechanism will be investigated in this chapter. This chapter is mainly focused on the growth mechanism and the study of interface between WO$_3$ nanowires and Pt/Si substrate.

The growth of nanostructures of WO$_3$ was done using PLD technique which is one of the Physical Vapour Deposition (PVD) techniques. Generally in PVD technique growth dynamics follows different growth modes like, *(i)Vapour solid (VS)*, (ii) *Vapour-liquid-solid (VLS) or (iii) Preferential Interface Nucleation (PIN)* [22-26].

The growth of nanowire/film by PVD method depends on thermodynamic parameters: super saturation (D_s) and substrate temperature (T_s) given by equation 3.1 [21]

$$D_s = KT_s \ ln \ (R/R_e) \ ….. \ …………………………….(3.1)$$

Where R = Actual deposition rate and R_e = Equilibrium value, K = Boltzmann constant.

From Table 3.1, it is quite clear that with increase of laser fluence the nanocrystalline thin film (at 110mJ) changes to partially/non-aligned nanowire (at 160mJ) and finally vertically aligned nanowire (at 200mJ). The influence of different growth parameters on the phase and morphology of the material grown in PLD and their characterization have been explained earlier (chapter 2, section 2.2.2.2).

The growth dynamics for i) nanocrystalline thin film and ii) Partially/non-aligned nanowires could be explained from generally reported VS mode growth [22] where at lower laser energy formation of film like structure occurs and wire like structure formation starts with increase of laser fluence above a critical laser energy following same growth mode [21]. But, for vertically aligned nanowires, VLS mode growth is not possible, as the deposition temperature is not high enough to melt the catalyst and diffuse the vapour through the molten catalyst to grow nanowires. In that case, only PIN mode may be assigned which needs further understanding regarding the growth mechanism. In following sub sections below each growth dynamics has been explained in detail.

   (i)   Growth dynamics of WO$_3$ nanocrystalline thin film

When the laser energy is low R/R_e value is also less which lowers the value of D_s (equation 3.1) and hence large island like growth occurs which coalesce due to the presence of T_s and forms film like morphology. In Fig. 3.1(a) a schematic diagram of the proposed growth dynamics of WO$_3$ thin film has been depicted [21].

   (ii)   Growth dynamics of WO$_3$ nanowires (Partially/non-aligned)

In the VS growth mode the vapor from the ablated target in PLD gets deposited preferentially on the solid catalysts at moderate temperature forming a unidirectional growth. For the vapor-solid (V-S) mechanism that leads to the formation of one-dimensional nanostructures, the supersaturation ratio of the condensing species in the gas plays a key role. To enable anisotropic growth to form nanowires, the supersaturation ratio of the condensing species must be maintained below some critical value, above which two-dimensional or even isotropic growth occurs. That is, a low supersaturation ratio is required for anisotropic

growth, whereas a medium supersaturation ratio leads to growth of bulk crystals [22]. Fig. 3.1(b) shows schematic representation of VS mode growth.
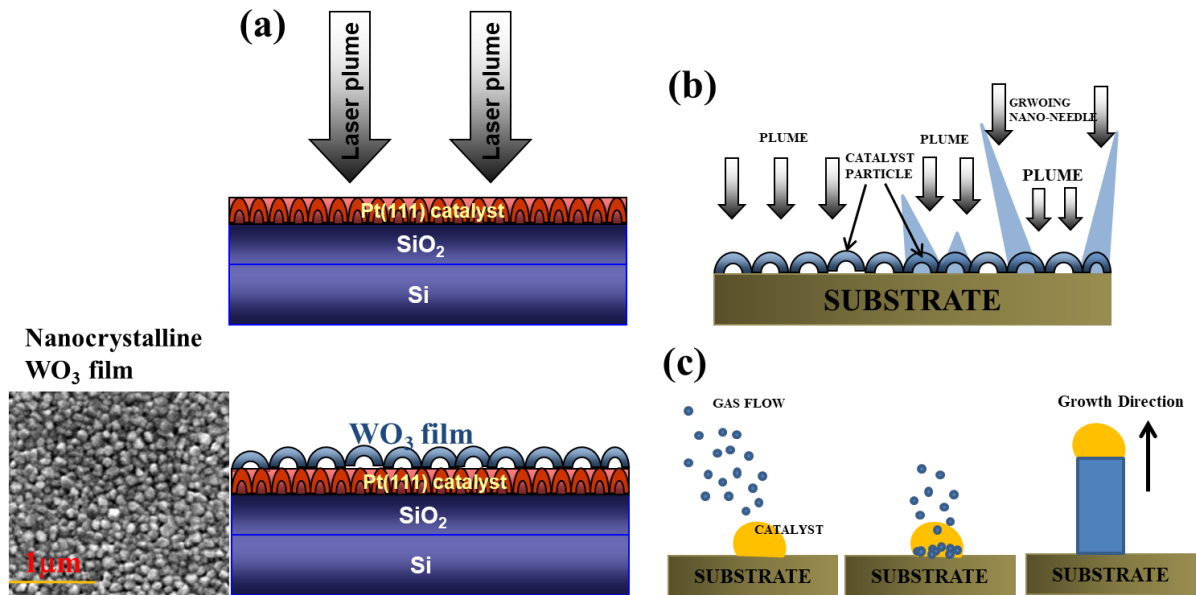
Figure 3.1: *Schematic diagram of (a) Growth dynamics of WO₃ thin film (Inset: FESEM image of nanocrystalline WO₃ thin film on Pt/Si); Schematic diagram of different growth mode in PVD (b) Vapour Solid (VS) growth (c) Vapour Liquid Solid (VLS) growth.*

In the VLS mode, vapors diffuse through the liquid catalyst (very high substrate temperature) and saturate on the substrates to form catalyst leading nanowires. The growth of a crystal through direct adsorption of a gas phase on to a solid surface is generally very slow. The VLS mechanism circumvents this by introducing a catalytic liquid alloy phase which can rapidly adsorb a vapor to supersaturation levels, and from which crystal growth can subsequently occur from nucleated seeds at the liquid–solid interface [23-25]. Fig. 3.1(c) shows schematic representation of VLS mode growth. The physical characteristics of nanowires grown in this manner depend, in a controllable way, upon the size and physical properties of the liquid alloy.

In case of WO₃ nanostructure synthesis in PLD, with the increase in the laser fluence (160 mJ) the deposition rate (R) increases that increase D_s and hence promotes wire like morphology over a critical value of laser fluence (equation 3.1). The nanowires are partially/non-aligned in this case and follows VS growth mode as deposition temperature is not reasonably high enough to melt Pt layer (600°C). It cannot support VLS growth mode as melting of catalyst is one of the prime conditions in VLS growth mode. But with further increase in the laser fluence it has been noticed that the nanowires become highly oriented as

well as vertically aligned. This leads to the possibility of finding another mechanism that has not been explored largely in case of growth of nanowires. This method was proposed by Wacaser et al. [26], which is based on preferential nucleation at the interface (PIN) between the deposited material and a crystalline solid (substrate). In Fig. 3.2 schematic diagram of growth dynamics proposed for partially/non-aligned nanowires has been shown [21].
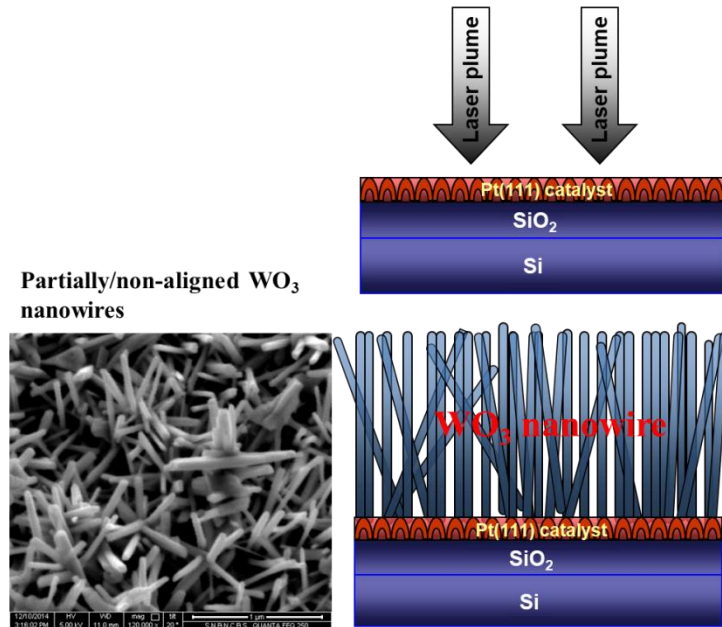
Figure 3.2: Schematic diagram of growth dynamics of partially/non-aligned WO₃ nanowires (Inset:FESEM image of partially/non-aligned WO₃ nanowires on Pt/Si).

Now, the growth mechanism for vertically aligned nanowires required modification of substrates with the help of laser fluence or laser parameters in PLD. Hence this proposition made us to rethink about the growth mechanism of the vertically aligned nanowires. This can be made possible by using spatially resolved technique of X-TEM analysis.

In the next sections 3.2.1 there is a discussion on how the cross-section lamella (lamella) of the WO₃ nanowires and substrate (nanowires/substrate) interface was prepared, and High Resolution TEM (HRTEM) analysis on the cross-section nanowires/substrate interface will be provided in section 3.2.2. Finally in section 3.2.3 underlying physics behind the growth of vertically aligned WO₃ nanowires has been discussed.

3.2.1. Lamella preparation of WO$_3$ thin film and nanowires on Pt/Si

The role of nanowires/substrate interface was investigated on cross sectional lamella (lamella), which was prepared in Helios 600 (FIB-FESEM) along with Gas Injection Source (GIS), Omniprobe accessories (discussed in Chapter 2, section 2.3.1.3). The lamella of WO$_3$/Pt/Si (lamella) preparation was carried out on thin film, partially/non-aligned and vertically aligned nanowires of WO$_3$ on Pt/Si (WO$_3$/Pt/Si sample) using the FIB-FESEM which is the most advanced equipment in the field of SEM for imaging and lamella preparation.

Before starting the lamella preparation region of interest (ROI) needs to be chosen to place it at a eucentric height (focal plane of electron and ion source) so that it remains focused for both Ion Beam and Electron Beam during lamella preparation.

While preparing the lamella of WO$_3$/Pt/Si, five crucial steps, as explained below, had been followed. Also the standardization to avoid possible damage and implantation of Gallium (Ga) ions on the nanowires has been discussed. The procedure for lamella preparation has been described as follows:

i. *Protective layer deposition on WO$_3$/Pt/Si*

In the ROI of WO$_3$/Pt/Si a platinum layer was deposited using FIB and GIS. Typical dimension (X $\times$ Y $\times$Z) of the protective layer made on WO$_3$/Pt/Si sample was (15μm $\times$2μm $\times$ 2μm), shown in Fig. 3.3(a).
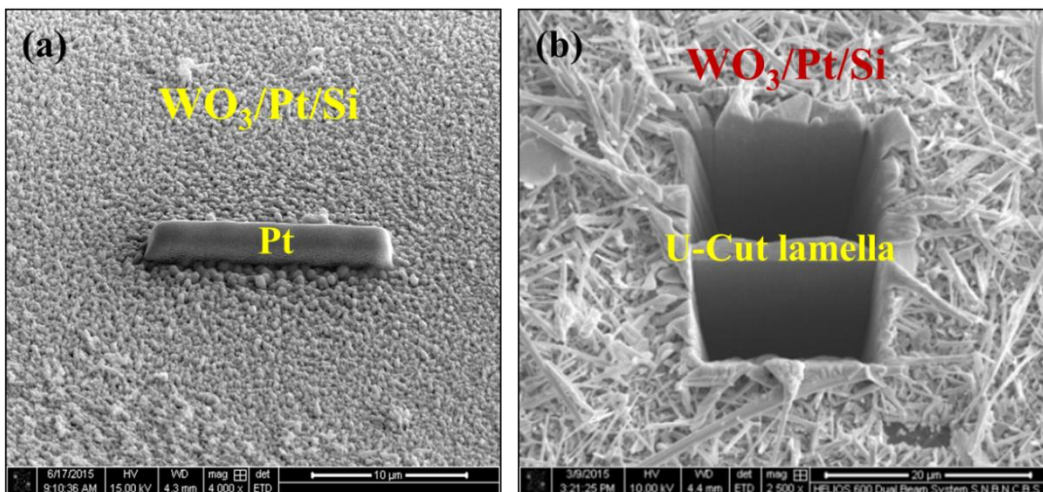
Figure 3.3: *(a) Protective Pt layer deposited on top of the WO$_3$/Pt/Si sample, (b) After regular cross sectional cut in lamella of WO$_3$/Pt/Si by FIB.*

ii.   *Bulk milling, intermediate milling and U-Shape cut*

Once the protective layer was formed, milling and cross sectional cutting of lamella from the WO_3/Pt/Si sample was carried out. In this process standardization was made to minimize Gallium (Ga) deposition (only 4% in this work has been achieved) and the lamella was prepared for X-TEM analysis. The steps involved in this process are:

a.   *Bulk milling to separate the lamella from the bulk sample*

In this step the FIB regular cross sectional cut was done just below the lamella with Pt-layer on both side of the WO_3/Pt/Si sample. During this process the stage was tilted at to face the ion beam directly. Typical parameters for bulk milling of WO_3/Pt/Si samples are provided in table 3.2. In Fig. 3.3(b) the lamella after the bulk or regular milling has been shown and it is standing like a nanowall inside the WO_3/Pt/Si sample.

Table 3.2: *FIB parameters for bulk milling of lamella*

FIB current	Lamella size	Stage tilt	kV
9.3-21nA	X= 15μm, Y= 2Z, Z= 5μm	52°	20kV

b.   *Intermediate milling*

This process reduces the lamella thickness from micrometer (μm) to hundreds of nanometer (nm) using cleaning cross section (CCS) mode at half depth of the bulk mill to clean the lower and upper exposed portion of the lamella. The details parameters for intermediate milling of WO_3/Pt/Si are provided in table 3.3 below.

Table 3.3: *FIB parameters for intermediate milling of lamella*

FIB current	Initial lamella thickness	Stage tilt	kV	Final lamella thickness
2.4nA	5-10μm	53.5°	10-20kV	1μm-800nm

c.   *U-Shape cut*

The lamella was taken out from the bulk sample by U-shape cut. In U-Shape cut, regular cutting was carried out at low ion current (2.4nA) at three side of the lamella and one side was half cut to keep the lamella hanging from the bulk WO_3/Pt/Si until it is welded with omniprobe for lifting out. Fig. 3.4 shows the lamella hanging from one end of WO_3/Pt/Si sample.
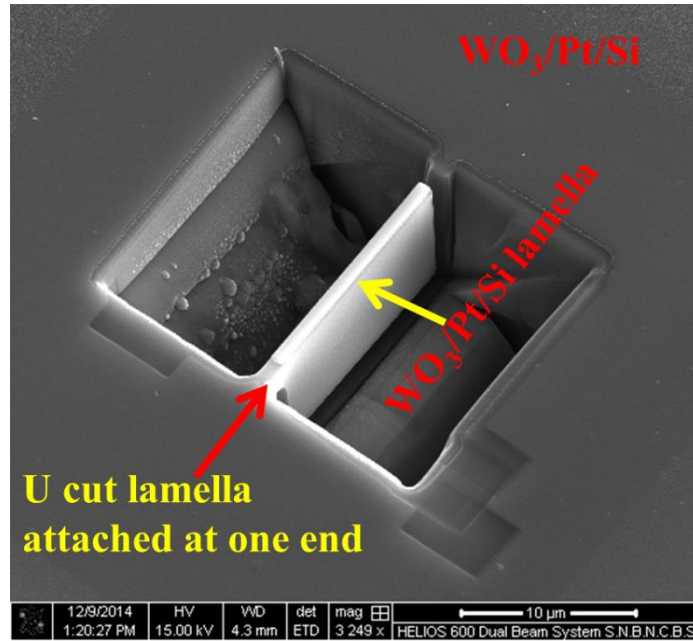
Figure 3.4: *U-Shape cut lamella attached at one end of WO₃/Pt/Si sample.*

iii.   Lamella lift out

One of the most difficult and sensitive part of cross sectional sample preparation was the lamella lift out. The omniprobe and GIS were inserted at very low magnification and 0° stage tilt of the FIB-FESEM.

Omniprobe was used to lift out the lamella from the bulk WO₃/Pt/Si and attaching it to the TEM grid. Initially it was moved and welded with the lamella surface using Pt-deposition. Afterwards the attached left portion of the lamella (Fig. 3.4) was cut from the WO₃/Pt/Si sample and omniprobe needle was moved away from the WO₃/Pt/Si sample position shown in Fig. 3.5(a).

iv.   Transfer and welding of lamella to TEM grid

The lamella of WO₃/Pt/Si needs to be attached to the specially designed omniprobe TEM grid (Fig. 3.5(a) inset) to perform microscopic analysis. Initially the position of the TEM grid was chosen and the lamella surface placed close to TEM grid followed by welding using GIS-Pt deposition. Then, the lamella was attached to omniprobe and TEM grid shown in Fig. 3.5(b). Afterwards omniprobe was detached from the lamella using FIB milling.
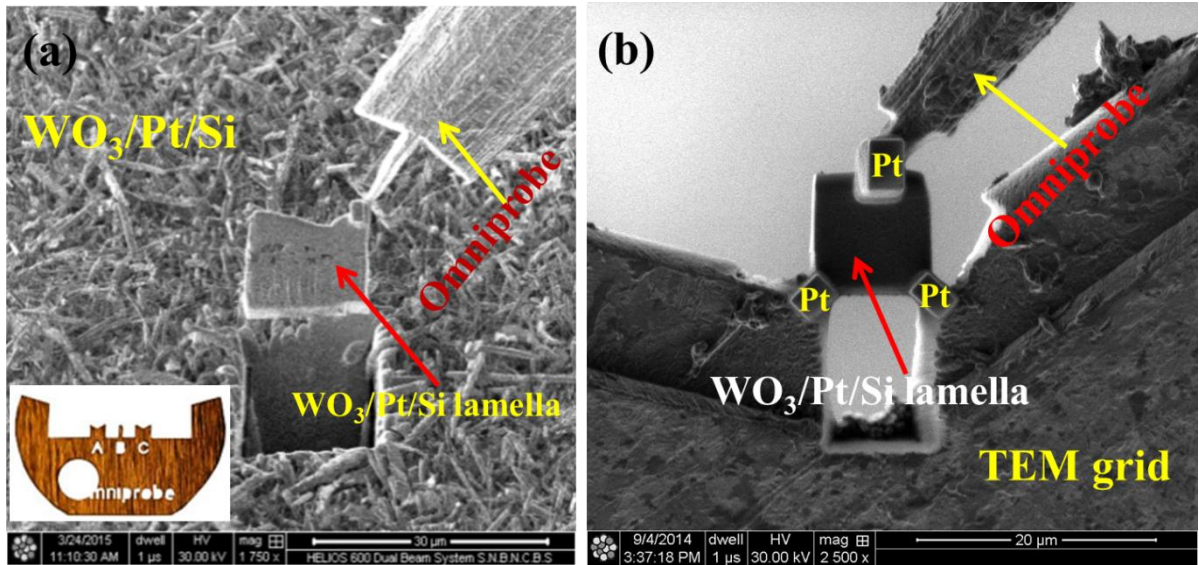
Figure 3.5: *(a) Lamella attached to Omniprobe needle (Inset: Omniprobe TEM grid), (b) Lamella attached on TEM grid and with Omniprobe needle.*

v.   *Final thinning of the lamella*

The last and most crucial part of cross sectional sample preparation is final thinning of the WO_3/Pt/Si lamella as it needs special caring of the lamella else the whole process would have damaged the thin lamella. The FIB parameters for final thinning are provided in Table 3.4 below. The final thinning was performed at low kV and low beam current to avoid possible damage of the lamella. Afterwards fast scan imaging with electron beam was performed to remove remittent residue material/ions on the surface of the thin lamella. Fig. 3.6(a) shows WO_3/Pt/Si lamella image after thinning down to 200-300nm and Fig. 3.6(b) shows the thin (<100nm) portion of the WO_3/Pt/Si lamella which is ready for HRTEM analysis.

Table 3.4: *FIB parameters for lamella final thinning*

Initial lamella thickness	kV	FIB Current	Final lamella thickness
(a) 1μm-800nm	10-20kV	2.4nA	300-200nm
(b) 300-200nm	2-5kV	0.24nA	<100nm
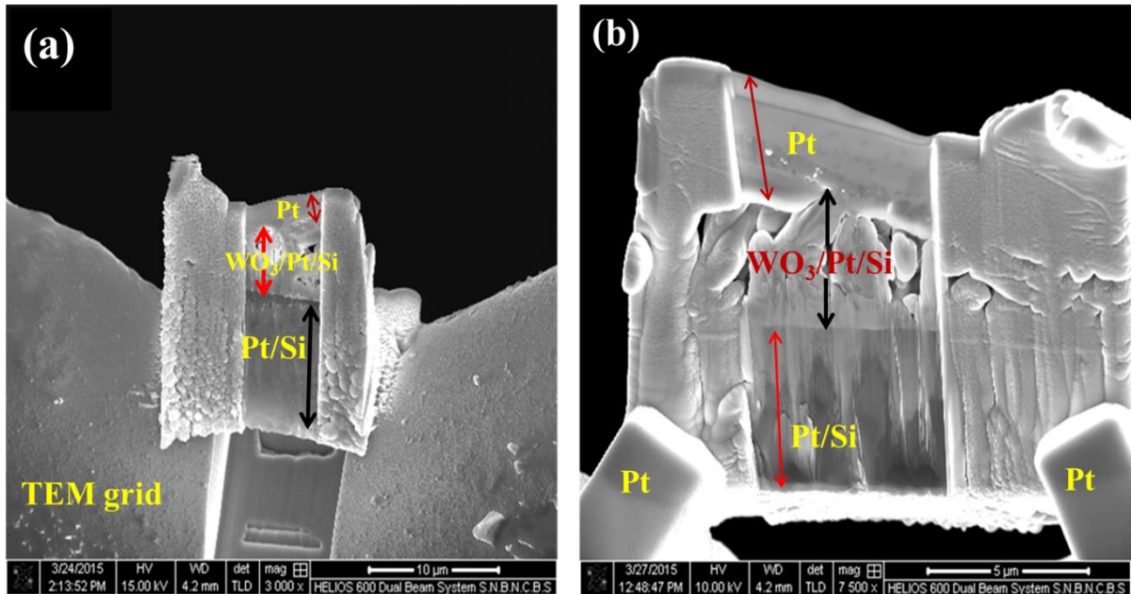
Figure 3.6: *(a) Lamella after initial thinning, (b) Lamella after final thinning*

The FESEM images of all three lamellas after final thinning (thin film, partially/non-aligned nanowires, and vertically aligned nanowires) in dual beam FIB-FESEM are shown in Fig. 3.7 [21].
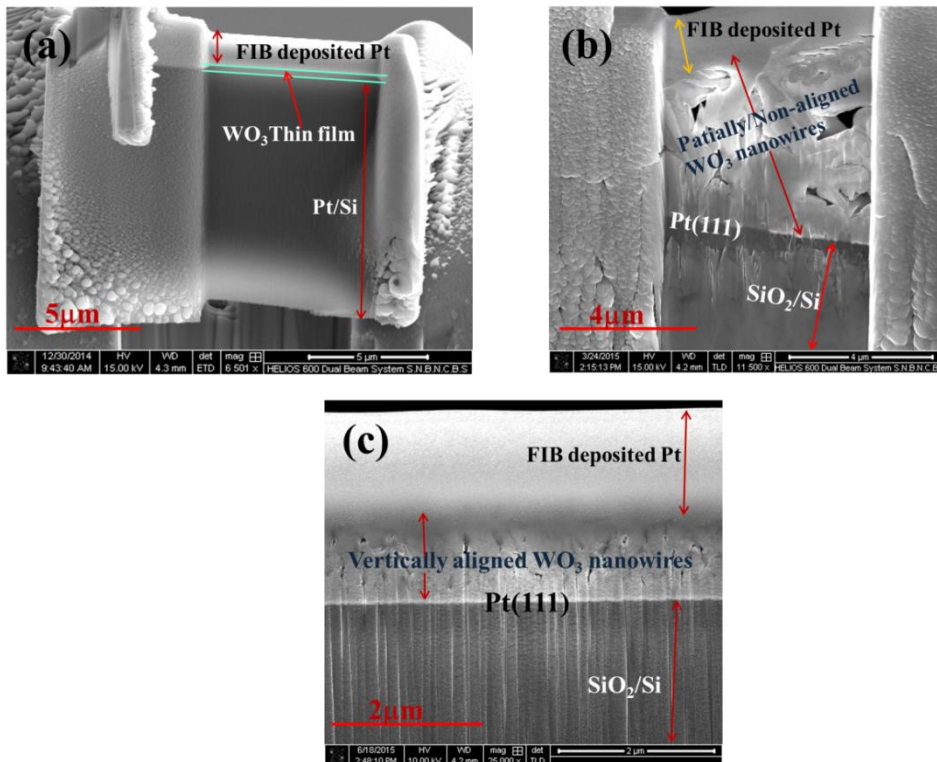
Figure 3.7: *FESEM images of lamella of (a) WO₃ thin film, (b) partially/nonaligned and (c) vertically aligned nanowires prepared by FIB-FESEM.*

3.2.2. Microstructural and chemical analysis using HRTEM and EDX

Microstructural analysis on WO_3/Pt/Si lamellas for thin film, Partially/non-aligned and vertically aligned nanowires were studied using High Resolution (HR) TEM and STEM mode (described in chapter 2, section 2.3.1.4). Also STEM mode with EDX Spectrometry (described in Chapter 2, section 2.3.2.1) line and area mapping analysis on WO_3/Pt/Si lamellas (thin film, partially/nonaligned and vertically aligned nanowires) were performed to understand the microstructure, chemical composition at the interface of WO_3 nanowires and Pt/Si substrate.

FEI Tecnai G^2 TF20 ST, 200kV TEM along with EDAX detector was used for the elemental mapping of the lamella. Elemental mapping of elements like Tungsten (W) and Platinum (Pt) and Oxygen (O) has been discussed below in sections 3.2.2 (b) and (c).

a) *HRTEM analysis on WO_3/Pt/Si thin film, partially/non-aligned and vertically aligned nanowires*

Before analyzing the interface physics and growth mechanism a brief microstructural analysis has been provided in this section. In fig 3.8 (a-c) Selective Area Electron Diffraction (SAED) patterns (discussed in chapter 2 section 2.3.1.3) of thin film, nonaligned nanowire, vertically aligned nanowire show change in crystal structure from monoclinic (Fig. 3.8 (a) to orthorhombic (Fig. 3.8(b, c) respectively due to change in laser energy [21].
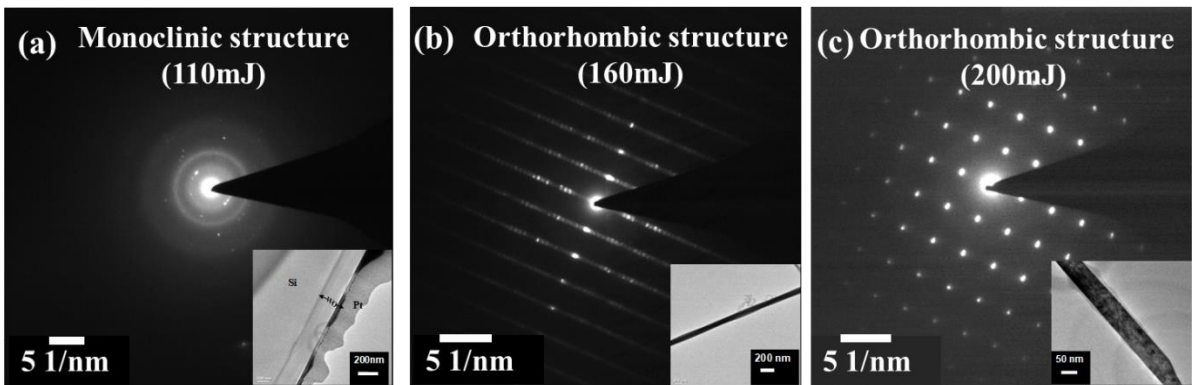
Figure 3.8: *Selected area electron diffraction pattern of (a) thin film lamella (Inset: TEM image of thin film lamella), (b) partially/non-aligned aligned nanowire (Inset: TEM image of a partially/non-aligned nanowires) and (c) vertically aligned nanowire (Inset: image of a vertically aligned nanowire).*

HRTEM image in Fig. 3.9(a) of thin film lamella shows lattice fringes having spacing of about 0.32 nm, which corresponds to the (220) plane of the monoclinic cell having unit cell parameters a= 0.7297 nm, b = 0.7539 nm, c = 0.7688 nm. Similar analysis has been performed on partially/nonaligned, vertically aligned nanowires show single crystallinity and corresponds to the (002) plane with lattice fringe spacing 0.3828nm (Fig. 3.9(b, c)) [21].
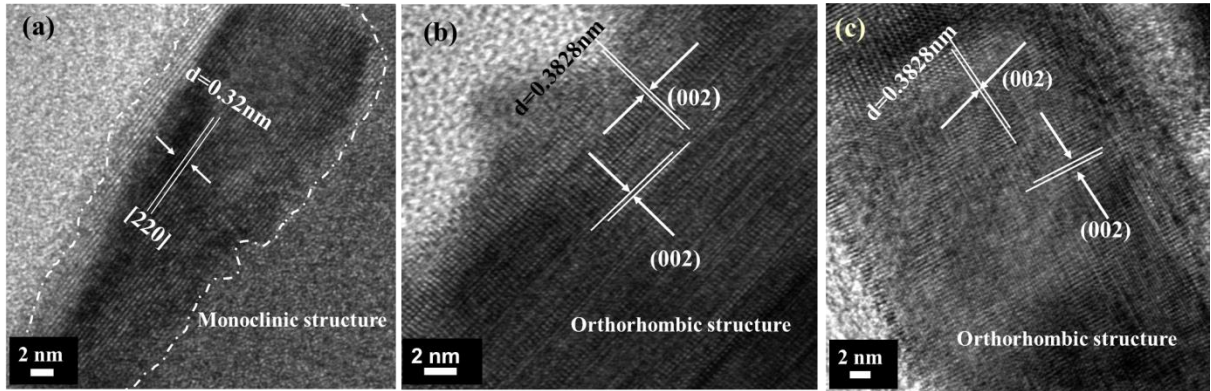
Figure 3.9: HRTEM micrographs showing lattice fringes of (a) thin film lamella, (b) partially/non-aligned nanowire, (c) vertically aligned nanowire.

b) <u>STEM-EDX mapping analysis on WO$_3$/Pt/Si lamella of partially/non-aligned WO$_3$ nanowires</u>

HADDF-STEM image provides information about the interface of WO$_3$ nanowires with the Pt/Si substrate. Fig. 3.10(a) shows the STEM image of the lamella and the substrate nanowires (WO$_3$/Pt/Si) interface are clearly distinguishable from the image. In Fig. 3.10(b) STEM-EDX line mapping (red arrow line shows direction and position of line mapping in Fig. 3.10(a)) shows accumulation of Pt (which comes from the protective layer) at the interface during lamella preparation of the partially/non-aligned nanowires due to the gaps in between the nanowires [21]. The diffusion of platinum inside the nanowires array during final thinning was confirmed from Fig. 3.10(b). As the nanowires are partially/non-aligned so diffusion of Pt from the top protective layer is obvious. The interface also contains very small amount of tungsten oxide with excess amount of oxygen, which suggests that during PLD deposition at lower laser energy (160mJ) tungsten gets impinged into the substrate at the interface before the growth of the nanowires. During the growth process, the impinged tungsten gets oxidized and formation of WO$_x$ might have occurred at the interface [21].

To confirm the presence of non-stoichiometric tungsten oxide at the Pt/Si and nanowire interface of the lamella STEM-EDX area mapping has been performed (Yellow marked area in Fig 3.10(a) is position of mapping). The analysis shows that the diffusion of tungsten (W)

and oxygen (O) was low at the interface and it was unable to modify the whole Pt layer of the substrate hence, the growth of the partially/non-aligned nanowires are governed by the PLD parameters and the Pt/Si substrate itself, following VS mode growth (Fig. 3.11). This analysis suggests that the growth takes place with less area of favourable nucleation site at the interface and promotes partially/non-aligned nanowire growth [21].
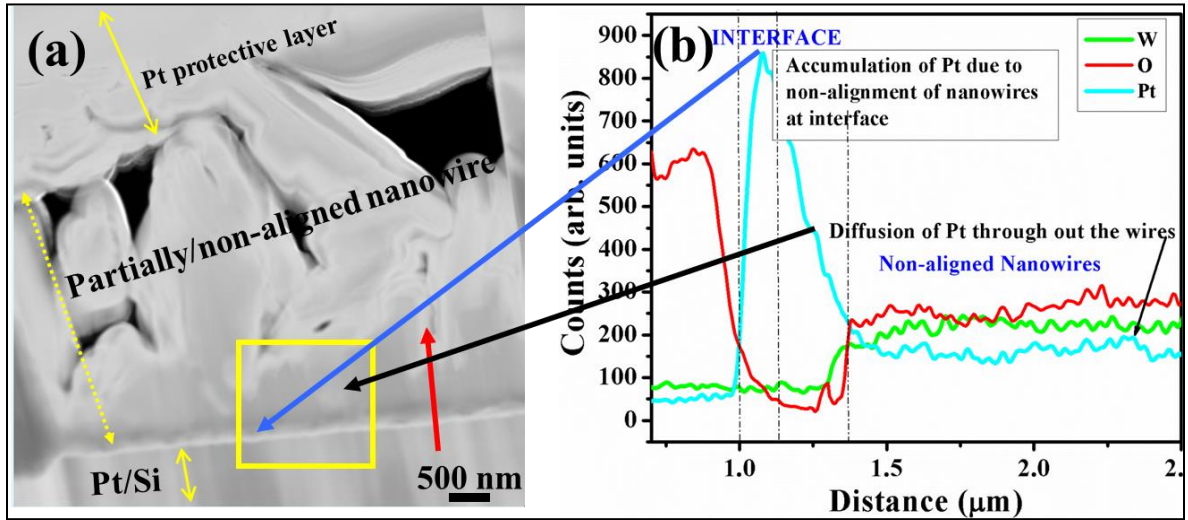
Figure 3.10: *(a) HAADF-STEM image of partially/non-aligned* WO_3*nanowires/Pt/Si lamella and Pt/Si, nanowires interface, (b) STEM-EDX line mapping from Pt/Si to nanowires through the interface.*
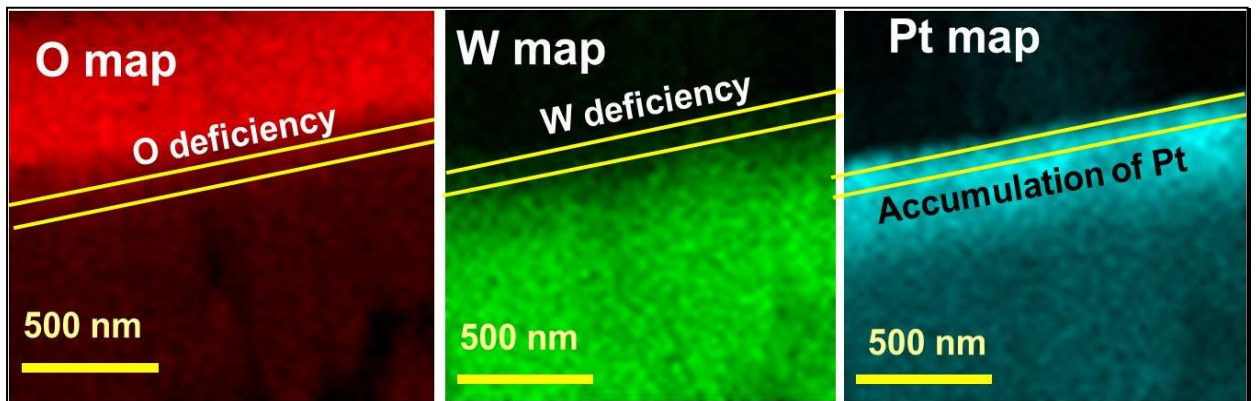
Figure 3.11: *STEM-EDX area mapping of the partially/non-aligned* WO_3*nanowires/Pt/Si lamella at nanowires and Pt/Si interface.*

c) <u>*STEM-EDX mapping analysis on* WO_3/Pt/Si *lamella of vertically aligned* WO_3 *nanowires*</u>

The HAADF-STEM image of the vertically aligned WO_3 nanowires/Pt/Si lamella in Fig. 3.12(a) is much more compact and due to very less amount of space in between nanowires there is no diffusion of Pt from the top protective Pt layer inside the array and at the interface

as shown in the STEM-EDX line mapping in Fig. 3.12(b) (taken at red arrow region of Fig. 3.12(a)). STEM-EDX line mapping also provides information about the diffusion of Tungsten (W) and Oxygen (O) in a higher amount compared to partially/non-aligned nanowires deposition [21].
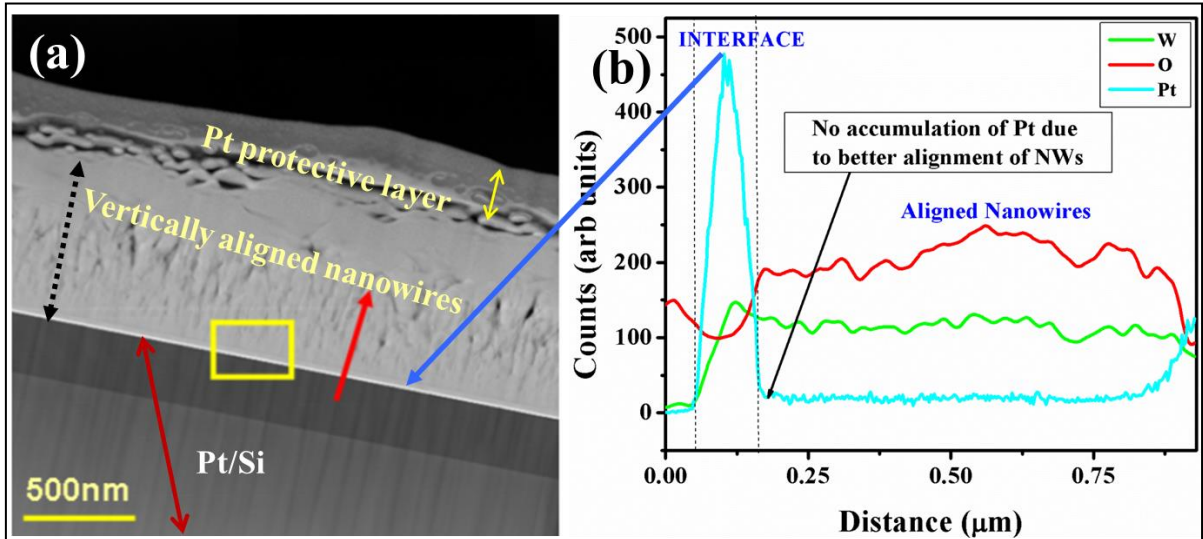
Figure 3.12: (a) HAADF-STEM image of vertically aligned WO$_3$nanowires/Pt/Si *lamella and Pt/Si, nanowires interface, (b) STEM-EDX line mapping from Pt/Si to nanowires through the interface.*

The higher laser energy might have an impact on the formation of nucleation just before the growth of the nanowires which can be confirmed from area mapping. From STEM-EDX area mapping (taken at yellow box region of Fig. 3.12(a)) shows higher impingement of W and O as well as a tiny layer formation of tungsten oxide with deficit oxygen (Fig. 3.13). The above observation clearly shows that the overall Pt in the substrate gets modified due to the formation of WO$_x$ (~70nm) at the interface which reduces the nucleation barrier at the interface and acts as a nucleation centre/layer to support the growth of vertically aligned nanowires (Fig. 3.13) [21].

This analysis provides a platform to explain the possible growth mechanism behind the different growth under PLD technique and aids the understanding of the important role played by the nanowires/substrate interface.

It also provides information about how a PVD technique like PLD can be used to grow vertically aligned nanowires, which is generally used for thin film growth. It also gives information about the condition where a thin film formation is hindered and vertically aligned

nanowire formation occurs. The possible mechanism and understanding of the same has been discussed in next section 3.2.3.
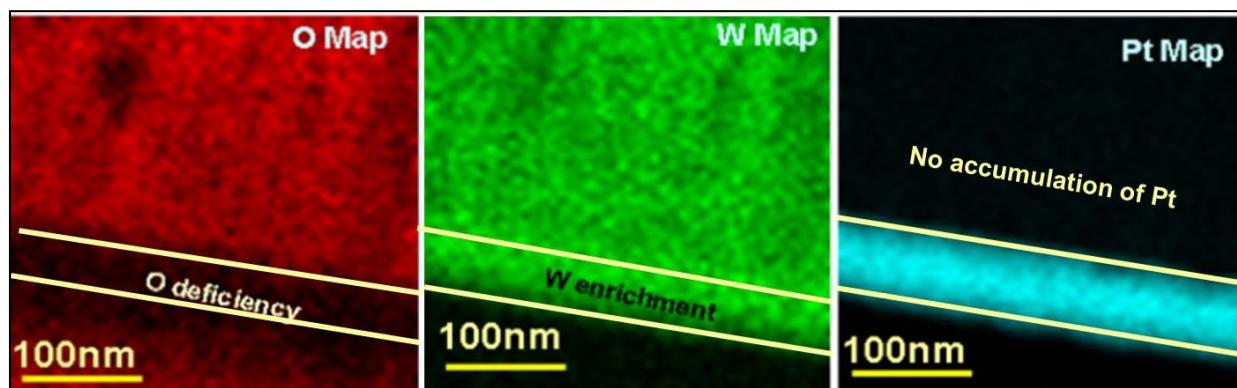
Figure 3.13: STEM-EDX area mapping of the vertically aligned WO₃nanowires/Pt/Si *lamella at nanowires and Pt/Si interface.*

3.2.3. Understanding of role of Interface: Growth mechanism for the formation of vertically aligned WO₃ nanowires

From the above observation it can be inferred that higher laser energy (200 mJ) helps to increase R and consequently D_s (equation 3.1). It is known that in case of pulsed laser assisted growth at higher laser energy, the laser induced diffusion of ablated materials may occur. This has already been observed and confirmed by FESEM and STEM-EDS analysis, that diffusion of W and O adatoms within Pt catalyst forms a mixed layer of 70 nm at the interface. Hence the interfacial region which is formed by the modification of the Pt layer acts as favorable nucleation site for the growth of vertically aligned WO₃ nanowires by reducing the overall contribution of the energies provided by surface energies of the substrate and the growing crystal as well as the interface energy between the two. Thus in case of vertically aligned nanowires (200mJ), growth mode may be assigned to PIN as shown in schematic diagram in Fig. 3.14 [21].

In previous section we provided the information about growth and interface physics study of WO₃ nanostructures grown by PLD method. In the next section 3.3, discussions on growth and surface chemistry study of TiO₂ nanorods array grown by wet chemistry route has been provided.
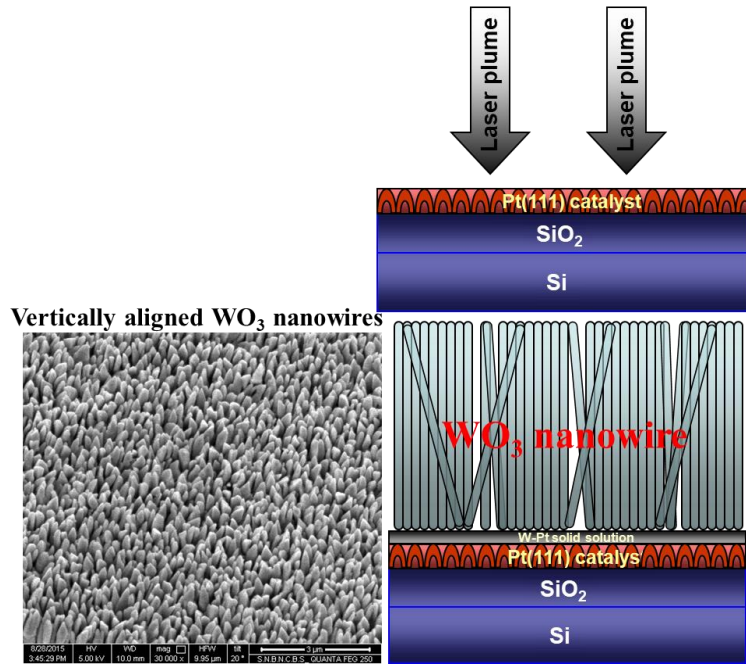
Figure 3.14: *Schematic diagram of growth dynamics (PIN mode) for vertically aligned WO₃ nanowires on Pt/Si grown in PLD (Inset: FESEM image of vertically aligned WO₃ nanowires on Pt/Si).*

3.3. Microstructure, surface chemistry and substrate effect analysis for vertically aligned TiO₂ nanorods growth

In section 3.2 analysis vertically aligned nanowires of WO_3 grown by PLD technique has been provided in details. In this section a discussion on microstructure, surface chemistry and substrate effect on growth of vertically aligned TiO_2 nanorods has been provided. TiO_2 nanorods were grown on TiO_2seeded/FTO and TiO_2seeded/Pt(111)/Si/SiO₂ (Pt(111)/Si) substrate by using hydrothermal method (details discussed in Chapter 2 section 2.2.3.1) [27]. This section of the thesis chapter also presents a simple and a general strategy to improve the growth of highly oriented rutile-TiO_2 nanorods at a low temperature, which in turn provides an opportunity to integrate them in devices. This section also provides information about the influence of different substrates which are the basis of integration of these nanorods in devices and are not really explored.

Mechanisms of phase transformations, reasons for nucleation of materials and explanations for the development of polytypic intergrowths are some of the basic questions in the area of material science. Thus it is very necessary to understand the relationships among crystal size,

crystal morphology, and stability to determine the primary mechanisms controlling crystallization. In this regard, this study will also provide a precise mechanism which might help in the understanding of different growth on different substrates. This understanding has been provided by an in-depth electron microscopic and chemical analysis in TEM. Surface morphology, phase formation analysis has been provided in chapter 2 section 2.2.3.1.

3.3.1. Microstructural analysis on a single TiO$_2$ nanorod

Fig. 3.15 shows TEM Bright Field, SAED pattern and HRTEM images of a TiO$_2$ NR grown on TiO$_2$seeded/FTO (Fig. 3a, b, c) and TiO$_2$ seeded/Pt(111)/Si (Fig. 3d, e, f) respectively, and confirms that the nanorods are single-crystalline in nature. In case of NR (diameter~100 nm), grown on TiO$_2$seeded/FTO, has growth direction along the (110) crystal plane with a preferred orientation along (001) (Fig. 3.15(b)), free from crystal defect and the lattice fringes (d$_{110}$ ~ 3.2 Å) confirms tetragonal rutile phase (JCPDS card no. 21-1276) (Fig. 3.15(c)). Fig. 3.15(e) SAED pattern confirms the rutile structure of the NR (diameter~ 150 nm) grown on TiO$_2$seeded/Pt(111)/Si and Fig. 3.15(f) shows the presence of crystal defects and a small shift in lattice spacing (d$_{110}$ ~ 3.3 Å) [27].
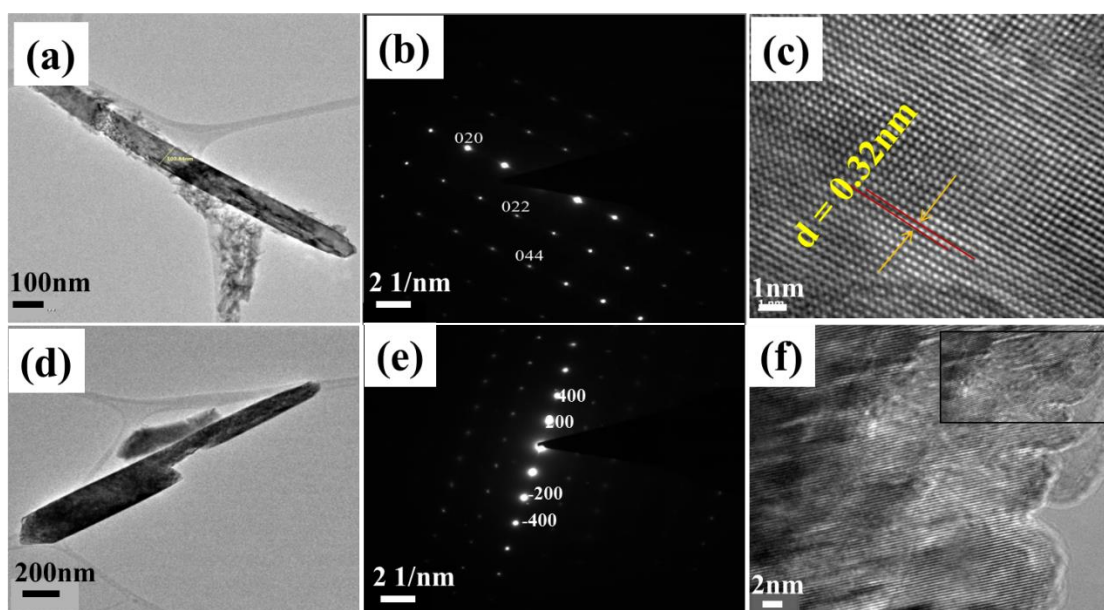
Figure 3.15: *TiO$_2$ NR grown on TiO$_2$seeded/FTO (a) TEM Bright Field image showing a single nanorod (b) SAED pattern (c) HRTEM image; TiO$_2$ NR grown on TiO$_2$seeded/Pt(111)/Si (d) TEM bright field image of a single NR, (e) SAED pattern and (f) HRTEM image (Inset: crystal defects).*

3.3.2. Surface chemistry analysis on a single TiO_2 nanorod using Gatan Imaging Filter (GIF)

The chemical analysis was performed on a single nanowire level, which requires a more spatially resolved tool. Gatan Imaging Filter (GIF) is used here as it is more precise, and as in this method region of interested could be small down to few tens of nm for chemical or elemental analysis. As this study entails an inclination towards a small portion of the nanowire, the use of GIF will provide far better access to chemical information in those smaller dimensions.

In EFTEM mode information about the stoichiometry of the nanorod elements was observed and in EELS mode the oxygen deficiency was studied and the effect behind the same was also analyzed.

The chemical analysis of a single TiO_2 nanorod (NR) under GIF provides very interesting information on the surface chemistry at a single nanorod level. Fig. 3.16 shows the EFTEM mapping for Ti L shell and Oxygen K shell of TiO_2 NR grown on TiO_2seeded /FTO and TiO_2seeded/Pt(111)/Si, respectively. The EFTEM mapping on a portion of a single nanorod depicts the distribution of the elements (Titanium (Ti) and Oxygen (O)) throughout the nanorod [27]. Fig 3.16(a, b) shows homogeneous distribution of Ti and O respectively, in NR grown on TiO_2seeded/FTO whereas; Fig. 3.16(a, b) shows inhomogeneous distribution of the Ti and O respectively, in NR grown on TiO_2seeded/Pt(111)/Si. In Fig 3.16(d) oxygen K shell mapping shows the concentration of O is higher at tip of the NR and lesser all along the length. Hence distribution of oxygen throughout the NR is inhomogeneous. This analysis also confirms that the NRs grown on TiO_2seeded/Pt/Si have oxygen deficiency, hence mixed anatase and rutile phases are present. [27]
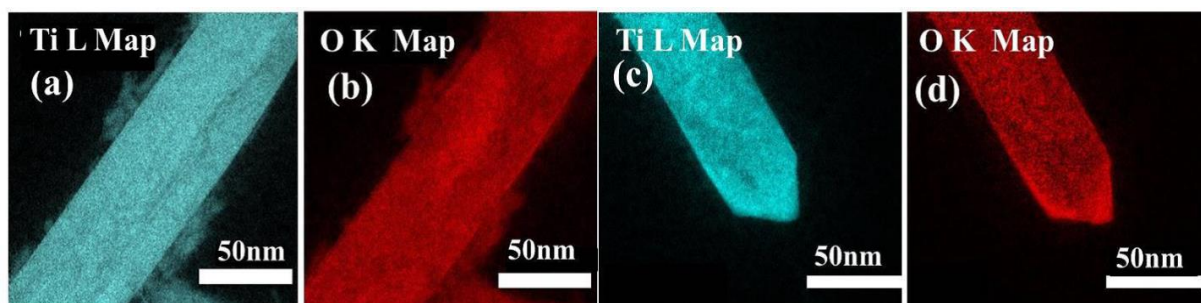
Figure 3.16: *EFTEM mapping on TiO_2 nanorod grown on TiO_2seeded/FTO substrate (a) Ti L Mapping, (b) O K mapping; EFTEM mapping on TiO_2 nanorod grown on TiO_2seeded/Pt(111)/Si substrate (c) Ti L mapping and (d) O K Mapping.*

In Fig. 3.17 (a) and (b) Electron Energy Loss Spectrometry (EELS) study shows core-loss spectra of Ti L2, L3 edge and O K edge taken on a single NR grown on TiO_2seeded/FTO and TiO_2seeded/Pt(111)/Si substrates respectively. It is clear from the spectrum (Fig.3.17 (a) and (b)) that there is a chemical shift in the Ti L-edge and O K-edge in case of Pt(111)/Si substrates [27]. Hence the change in the stoichiometry of the nanorods, as well as the change in the valence state of both Ti and O has been confirmed.
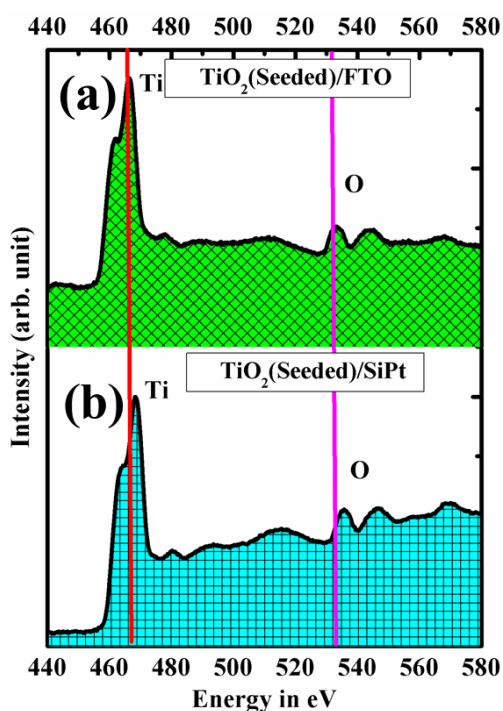
Figure 3.17: EELS spectrum showing chemical shift in the Titanium L edge (red line) and Oxygen K edge (pink line) of TiO_2 nanorod on (a) TiO_2seeded/FTO (b) TiO_2seeded/Pt(111)/Si Substrates, respectively.

The core loss spectrum for Ti L edge and O K edge on single NR grown on TiO_2seeded /FTO substrate is shown in Fig. 3.18(a) and (c) respectively. The core loss spectrum of Ti L edge and O K edge for single NR grown on TiO_2seeded/Pt(111)/Si substrate is shown in Fig. 3.18(b) and (d) respectively. Fig. 3.18(a) and (b) core loss spectrum of Ti L edge shows transition of Ti 2P to 3d. The spectrums were fitted using standard Lorentzian fitting, which shows Spin-orbit splitting into $2p^{3/2}$ (L3) and $2p^{1/2}$ (L2) levels, with a separation of 5.1eV and 4.8eV respectively for both Ti Spectrum [27]. The separation in the binding energy and peak shift confirmed that there is a difference between the chemical states of Ti of the NRs grown on both the substrates. This chemical shift is related to the reduction of the Ti according to several reports [28, 29]. Hence in case of NRs grown on TiO_2seeded/Pt(111)/Si presence of a

mixed phase is clearly justified from the chemical shift. Earlier reports on experiments and DFT calculations from different groups confirmed that the Ti Ledge and O K edge of TiO_x (x<2) shifts toward a higher energy-loss position as compared with that of TiO_2 [28, 29]. Fig. 3.18 (c) and (d) shows O K edge spectra corresponding to the transition of O1s to 2p of the NRs grown on TiO_2seeded/FTO and TiO_2seeded/Pt(111)/Si respectively.

For the NRs grown on two substrates splitting can be observed in the O K edge corresponding to transition to O 2p-Ti 3d hybridized states. Two distinctive features at 532eV and 535eV for TiO_2seeded/FTO and 534 and 536eV for TiO_2seeded/Pt(111)/Si has been observed for these spectra. The oxygen (O^{2-}) attached to Ti^{4+} in TiO_2 related to the peaks at 532eV and the surface adsorbed oxygen species associated with the peak at 532eV [30, 31]. The number of oxygen defects on both the (002) and (100) facets corresponds to area under the curve and the intensity of the overall oxygen peak.
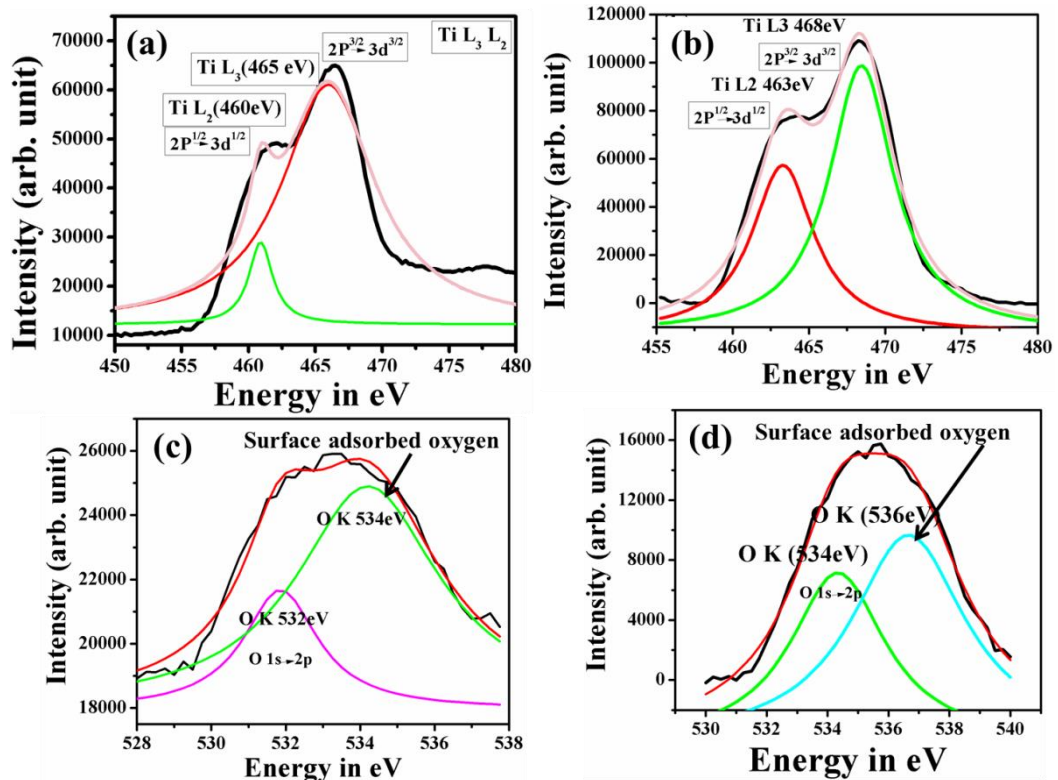
Figure 3.18: *EELS spectrum (deconvoluted) of Titanium L3 and L2 edge (black line) with Lorentzian fitting curves (pink, red and green lines) on (a) TiO₂ nanorod/TiO₂seeded/FTO, (b) TiO₂nanorod/Pt(111)/Si; EELS spectrum (deconvoluted) of Oxygen K edge (black line) with Lorentzian fitting curves (red, green and pink lines) on (c) TiO₂nanorod/TiO₂seeded/FTO and (d) (red, green and blue lines) on TiO₂nanorod/TiO₂seeded/Pt(111)/Si.*

In Fig. 3.18 (c) and (d)) from the O1s overall curves for both the substrates respectively it can be concluded that there are abundant surface oxygen defects in the TiO_2 NRs in case of TiO_2seeded/Pt(111)/Si substrates. It has been observed that the ratios of surface oxygen defects play a role in the photocatalytic activity of TiO_2 NRs [32, 33].

It can be concluded from EELS analysis that the type of substrate which enables the growth of TiO_2 NRs with a high ratio of (002) facets on FTO substrates regulates the photocatalytic activity (controlling the oxygen stoichiometry) of the TiO_2 NRs.

3.3.3. Understanding of Growth mechanism of TiO_2 nanorods synthesized by hydrothermal route

The nanorods synthesized on plain glass or tin doped indium oxide (ITO) coated glass substrates, were polycrystalline in nature and randomly oriented with respect to the substrate specified in earlier report [34].

Reports confirmed that the "oriented attachment growth mechanism" is followed during the aggregation of TiO_2 nanoparticles [35]. The adjacent particles are self-attached instantly to share a common crystallographic orientation in case of oriented attachment and get connected at a planar interface. For Particles which nucleate on a substrate and coalesce during growth also follows this mechanism [35]. Attachment always takes place at the high energy surfaces in order to reduce the surface energy by eliminating high energy facets. TiO_2 seed on FTO can effectively act as a nucleation layer for growth of TiO_2 nanorods on FTO substrate [36]. Growth of TiO_2 crystal occurs instantly along (002) plane to minimize the surface energy, as both the rutile TiO_2 and FTO have tetragonal structure and the surface energy of (002) plane is much higher than (110) plane. Thus the growth direction of the nanorods in this case is perpendicular to the (002) plane which also was according this analysis found to be [100]. The high lattice mismatch and difference in structure of Pt(111)/Si (Cubic, a = 3.9Å) and TiO_2 (Rutile, a=b=4.593Å) TiO_2seeded Pt(111)/Si substrate does not provide similar nucleation sites thus the probability of the growth of (002) plane is reduced i.e the growth direction of the nanorods are parallel to the (002) plane i.e, [001] [27]. The nucleation and growth of rutile TiO_2 is thermodynamically and kinetically controlled by the enhanced corner shared bonding of $[TiO(OH_2)_5]^{2+}$nuclei in case of acidic solution. Also, the selective adsorption of anions on (002) surface occurs due to the presence of large number of five-fold co-ordinated Ti^{4+} atoms, two-fold coordinated O^{2-} atoms and oxygen vacancies and a

'screening layer' is formed on surface which restrict further oxidation of $[TiO(OH_2)_5]^{2+}$ complex on surface [27].

On the contrary, $[TiO(OH_2)_5]^{2+}$ complex has been adsorbed to decrease the surface energy due to presence of two cusps of rods consist of other higher energy surface. Thus in case of TiO_2seeded/Pt(111)/Si substrate the nanorods grow anisotropically (Fig. 3.19). The shape controlled chemistry where Cl^- ions are selectively adsorbed onto the (110) crystal plane of rutile TiO_2, suppressing further growth of that plane and resulting in the formation of nanorods or nanoflowers also can explain the anisotropic growth of the nanorods (Fig. 3.19).

The preferential growth of (002) facet of TiO_2 nanorods on TiO_2seeded/FTO substrates has also been proposed considering the surface energy of (002) plane is much higher than (110) plane. According to Donnay Harker rules, {001} faces has about 1.4 times higher surface energy than {110} faces. During the time of crystal growth higher energy surfaces usually diminish very fast [37, 38]. It has been observed that TiO_2 seeding layer on FTO substrate efficiently provides nucleation sites during the growth of TiO_2 nanorods on FTO [36]. The epitaxial growth of TiO_2 nanorods on FTO substrate was only possible due to a very small lattice mismatch of rutile TiO_2 (a=b= 4.953Å) and FTO (a=b= 4.687Å) substrate [20].
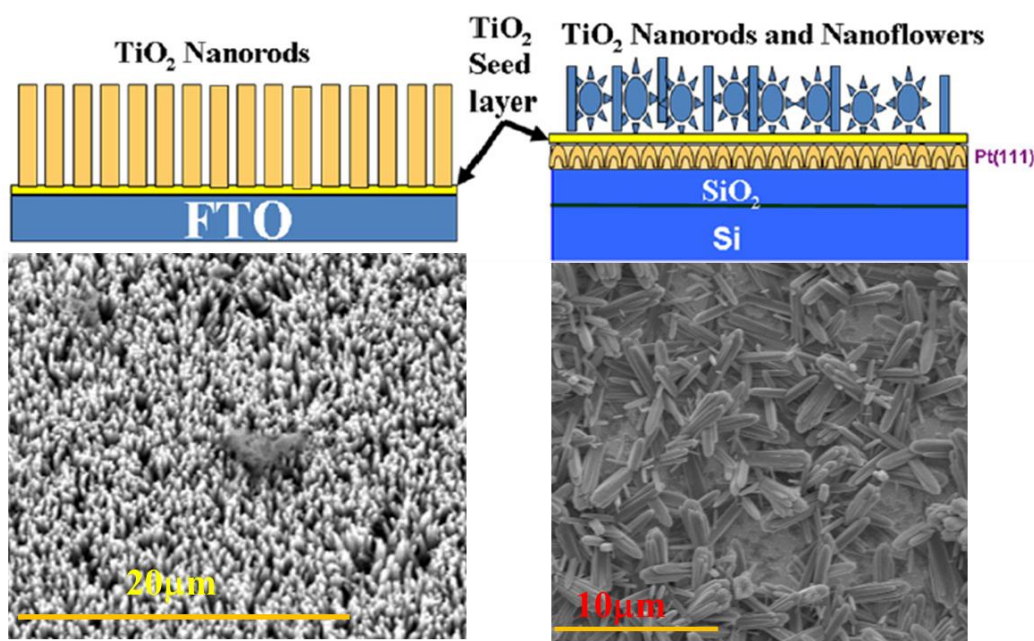
Figure 3.19: *Schematic diagram showing the substrate dependent anisotropic growth of TiO_2 NRs and corresponding FESEM images.*

3.4. Conclusion

This chapter has thus provides information about the analysis of nanostructures and substrate interface physics by preparing cross sectional lamella using Dual beam FIB-FESEM and surface chemistry using advanced chemical analysis technique (EELS/EFTEM).

Growth of vertically aligned WO_3 nanowires using PLD is very rare and non–trivial technique. The growth of nanostructures of WO_3 using PLD and the study of nanowires/substrate interface using cross sectional X-TEM study performed, was not reported before. The influence of laser energy on the growth morphology has been studied in details. The laser energy used for the ablation controls, the plume, the energy and flux of the ablated material then reaches the substrate on which growth occurs. This ablation parameter in PLD can be controlled which in turn leads to the control of growth morphology, to grow the dense vertically aligned single crystalline nanowires. Lamella preparation parameter was standardized to minimize the effect of gallium ions depositing on samples, which reduced gallium implantation to as low as 4%. The STEM-EDS analysis explores the role of nanowire and substrate interface and growth parameters during synthesis process and how one can tune the growth and grow desirable nanostructures of binary oxides. These will help to have a control over nanowires' size and their distribution density, which is one of the critical problems for their effective integration in practical devices.

Also, in the surface chemistry analysis using GIF, the processing-structure–property relationships in highly oriented TiO_2 nanostructures along with the influence of different substrates (cubic and tetragonal), which are the basis of integration of these nanorods in devices, have been explored. The growth mechanism and dependence of morphology of TiO_2 nanorods on the surface chemistry of substrate has been provided from this analysis. It has been found that TiO_2 nanorods and anisotropic nanoflowers together can be grown on different planes if the material property, surface chemistry of the substrate can be changed from rutile to cubic. Further, the growth of polycrystalline TiO_2 nanoflowers using Pt(111)/Si as a substrate has been also demonstrated in detail.

Bibliography

1. C. G. Granqvist, *"Handbook of Inorganic Electrochromic Materials"*, Elsevier, NewYork, 1995.

2. C. Santato, M. Odziemkowski, M. Ulmann and J. Augustynski, J. Am. Chem. Soc., 123, 10639–10649, 2001.

3. L. Zhao, Caiting Li , J. Zhang, X. Zhang, F. Zhan, J. Ma, Y. Xie, G. Zeng, Fuel, 153, 361–369, 2015.

4. F. Huguenin, E. R. Gonzalez and O. N. Oliveira Jr, J. Phys. Chem. B, 109, 12837–12844, 2005.

5. S. H. Lee, H. M. Choeng, J. G. Zhang, A. Mascarenhas, D. K. Benson and S. K. Deb, Appl. Phys. Lett., 74, 242–244, 1999.

6. C. B. Trasferetti, F. P. Rouxinol, R. V. Gelamo, M. A. Bica de Moraes, C. U. Davanzo and D. L. de Faria, J. Phys. Chem. B, 108, 12333–12338, 2004.

7. M. Satnkova, X. Vilanova, E. Llobet, J. Calderer, C. Bittencourt, J. J. Pireaux , X. Correig, Sens. Act., B, 105, 271–277, 2005.

8. A. I. Gavrilyuk, Electrochim. Acta., 44, 3027–3037, 1999.

9. M. Li, W. Gao, A. Posadas, C. H. Ahn, E. I. Altman, J. Phys. Chem. B, 108, 15259–15265, 2004.

10. G. Soto, W. D. L. Cruz, J. A. Diaz, F. F. Castillon, M. H. Farias, Appl. Surf. Sci., 218, 282–290, 2003.

11. S. Ma and B. G. Frederick, J. Phys. Chem. B, 107, 11960–11969, 2003.

12. C. B. Trasferetti, F. P. Rouxinol, R. V. Gelamo, M. A. Bica de Moraes, C. U. Davanzo and D. L. de Faria, J. Phys. Chem. B, 108, 12333–12338, 2004.

13. Y. Djaoued, S. Balaji and R. Bruning, J. Nanomater. 7, 674168, 2012.

14. S. Roy Moulik, S. Samanta, B. Ghosh, App. phys. Lett., 104, 232107, 2014.

15. M. Satnkova, X. Vilanova, E. Llobet, J. Calderer, C. Bittencourt, J. J. Pireaux and X. Correig, Sens. Act., B, 105, 271–277, 2005.

16. B. K. Mutuma, G. N. Shao, W. DuckKim, H. TaikKim, J. Colloid and interface science, 442, 1-7, 2015

17. Y. Baek, and K. Yong, J. Phys. Chem. C, 111, 3, 1213–1218, 2007.

18. J. Nian, H. Teng J. Phys. Chem. B, 110, 9, 4193–4198, 2006.

19. J. Ha, P. Muralidharan, D. K. Kim, J. Alloys and Comp., 475, 446–451, 2009.

20. B. Liu and E. S. Aydil, J. Am. Chem. Soc., 131, 11, 3985–3990, 2009.

21. A. Ghatak, S. Roy Moulik, B. Ghosh, RSC Adv., 6, 31705–31716, 2016.

22. J. Lai, L. Chen, X. Fu, J. Sun, Z. Ying, J. Wu and N. Xu, Appl. Phys. A: Mater. Sci. Process., 102, 477–483, 2011.

23. L. Chen, X. Fu, J. Lai, J. Sun, Z. Ying, J. Wu and N. Xu, J. Electron. Mater., 41, 1941–1947, 2012.

24. R. S. Wagner and W. C. Ellis, Appl. Phys. Lett., 4, 89, 1964.

25. T. I. Kamins, R. S. Williams, D. P. Basile, T. Hesjedal and J. S. Harris, J. Appl. Phys., 89, 1008–1016, 2001.

26. B. A. Wacaser, K. A. Dick, J. Johansson, M. T. Borgstrom, K. Deppert and L. Samuelson, Adv. Mater., 21, 153–165, 2008.

27. S. Roy Moulik, A. Ghatak, B. Ghosh, Surf. Sci., 651, 175–181, 2016.

28. C.M.Wang, Z.G. Yang, S. Thevuthasan, J. Liu, D.R. Baer, D. Choi, D.H. Wang, J.G. Zhang, L.V. Saraf, Z.M. Nie, Appl. Phys. Lett. 94, 233116, 2009.

29. N. Brun, C. Colliex, J. Rivory, K.Y. Zhang, Microsc. Microanal. Microstruct., 7, 161, 1996.

30. J.H. Zheng, Q. Jiang, J.S. Lian, Appl. Surf. Sci., 257, 5083, 2011.

31. T. Rakshit, S.P. Mondal, I. Manna, S.K. Ray, ACS Appl. Mater. Interface., 4, 6085, 2012.

32. S. M. Prokes, J. L. Gole, X. Chen, C. Burda, W. E. Carlos, Adv. Funct. Mat, 15, 1, 161-167, 2005.

33. J. Yan, G. Wu, N. Guan,a Landong Li, Zhuoxin Lib and Xingzhong Cao, Phys. Chem. Chem. Phys.,2013, 15, 10978.

34. A. Kumar, A.R. Madaria, C.W. Zhou, J. Phys. Chem., C 114, 7787, 2010.

35. R.L. Penn, J.F. Banfield, Science 281, 969, 1998.

36. H. E. Wang, Z.H. Chen, Y.H. Leung, C.Y. Luan, C.P. Liu, Y.B. Tang, C. Yan, W.J. Zhang, J.A. Zapien, I. Bello, S.T. Lee, Appl. Phys. Lett., 96, 263104, 2010.

37. P.D. Cozzoli, A. Kornowski, H. Weller, J. Am. Chem. Soc., 125, 14539, 2003.

38. Y.W. Jun, M.F. Casula, J.H. Sim, S.Y. Kim, J. Cheon, A.P. Alivisatos, J. Am. Chem. Soc., 125, 15981, 2003.

Chapter 4

Opto-electrical property study on Tungsten Oxide (WO$_3$) thin film and nanostructures

In this chapter, the opto-electrical response of metal binary oxide (e.g Tungsten oxide (WO$_3$) thin films and nanostructured film having different surface topology/morphology grown by Pulse Laser Deposition technique (PLD) has been studied. The PLD growth parameters are tuned in such a way that the thin films of different and desired surface morphologies like nanocrystalline film on SiO$_2$/Si (SO) and needle like structured film on SrTiO$_3$ (STO) (100) substrates were obtained. The two films show completely different photoreponse behavior; nanocrystalline film having ON/OFF states of photocurrent in presence/absence of light with 27% current enhancement and needle like nanostructured film showed persistent photocurrent (PPC) even after removal of light with 50% current enhancement at room temperature at a nominal bias voltage of 0.1V at 360nm wavelength. These phenomena strongly depend on surface morphology, presence of light as well as the surface area exposed to light. An explanation has been proposed for this modification of photoresponse behaviour in consideration of different surface morphology, surface defects, and adsorption/desorption of oxygen along with effect of light.

4.1   Introduction

Tungsten Oxide (WO_3) bulk, thin film and nanostructures are extensively studied materials as it is possible to synthesize in different size, shape and morphology [1-10]. WO_3 nanostructures are capable of providing wide range of properties e.g. optical, gasochromic, optoelectrical [11-15], which makes it a popular candidate for applications in wide angle high contrast display, gas and temperature sensor and other optical field. Studies from the last decade confirm that these properties were also dependent on material size, shape, crystallinity, texture, structure and effect of quantum confinement at low dimension [1, 16-19].

Optical property and optical response of WO_3 on different nanostructures, thin films are less explored and very few reports are available on the luminescence response of WO_3 nanostructures, due to its low emission efficiency and indirect band gap electronic structure. Though, some characterization on optical behaviour on different WO_3 nanostructures had been reported but detail study remains unexplored [17, 20-21].

Wavelength dependent photoresponse of opto-electrical device using binary oxide nanostructures was not studied earlier. In this chapter photoresponses on WO_3 nanocrystalline film and needle like structured film with different surface morphology have been studied extensively. Photoresponse study on single NW level was reported almost a decade earlier [16], but surface morphology dependent photoresponse study has not been highlighted afterwards. Also, physical properties (e.g. optical) on different WO_3 nanostructures had been reported but the science behind the possible mechanism remains unexplored [17, 20-21].

In this thesis chapter, the effect of size, shape and morphology tailoring on physical properties of binary oxide (WO_3) has been emphasized. It had been observed interestingly that the modification or tuning of surface morphology from nanocrystalline film to needle like structured film tuned the photoresponse. The possible physics behind this modification in respect of surface morphology and chemical stoichiometry have been explained in details in this chapter.

4.2   Principle behind photoreponse/opto-electrical response

The recent advancement of application in the field of semiconductor material created interest for the study of semiconductor device application. The popular advanced optical semiconductor devices are p-n junction device with optoelectronic property (eg: Laser diode, light emitting diode, photodiode) [23-25]. This advancement in the application attracts more research knowledge for semiconductor device with optical properties. The optical and optoelectrical property of this semiconductor device mainly depend upon the p-n junction type and the material used as semiconductor. The basic semiconductor material has conduction and the valance band separated by a gap known as the energy band gap (E_g). The recent advancement of these semiconductor materials provided information about presence of some level in between conduction and valance band known as impurity/defect levels created due to the defects or the impurities of the material during synthesis.
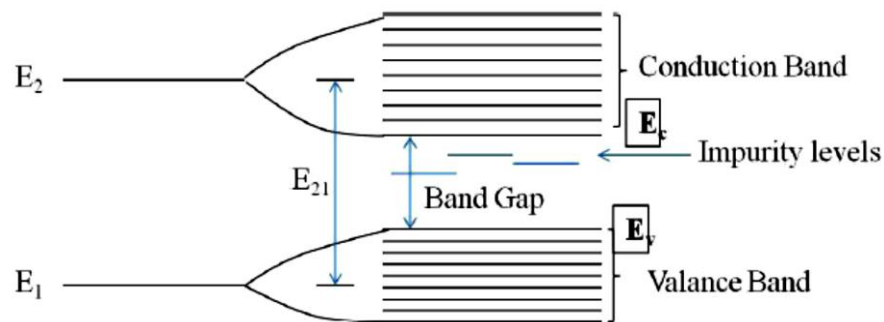
Figure 4.1: *Schematic view of Band Diagram of Semiconductor. Source ref. [26]*

Fig. 4.1 shows the schematic band diagram of a semiconductor and the intermediate impurity levels. The photoconduction phenomena observed in the photo sensitive semiconductor material can be easily explained using the basic concept of electron transport in semiconductor. These processes involve photon absorption, generation of free carries, electrical transport by free carriers and finally recombination or trapping of those carriers. The photoconduction terminologies described below are illustrated using Fig. 4.2.

4.2.1   Intrinsic optical absorption

In this process/mechanism semiconductor material transport electron form valance band to conduction band by absorbing photon energy Fig. 4.2(a)

4.2.2   Extrinsic optical absorption

In this process/mechanism of semiconductor material, transport of electron from impurity level to conduction band and valance band to impurity level takes place by absorbing photon energy, Fig. 4.2(b) and (c) respectively. The electrons present in the impurity level are capable of (i) recombining with free carrier of opposite type Fig. 4.2(d) and (e), or (ii) they will be excited by other sources (e.g thermal energy) for recombining in the nearest band. This involves capturing/trapping and releasing/detrapping of the electrons. Fig. 4.2(f) depicts this process and defines the dynamics of photoconduction as well as the time dependency of the photocurrent.
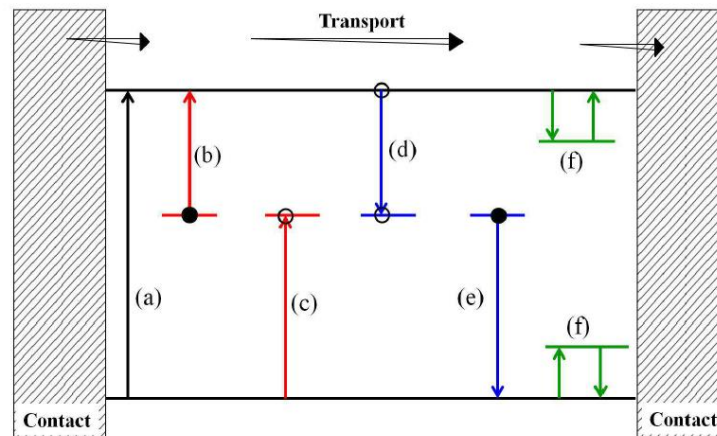
Figure 4.2: *Major transitions and phenomena associated with opto-electronic effects in homogeneous semiconductors (a) Intrinsic absorption, (b) and (c) extrinsic absorption, (d) and (e) capture and recombination, (f) trapping and detrapping. Source ref. [27].*

4.3   Physics behind electrical contacts

The opto-electrical response from a device can be measured once the electrical contacts (metal contacts) on both ends of the device were fabricated. The contact also controls the flow of electron (electrical current flow) in the metal and semiconductor junction. There are two types of contacts:

4.3.1 Ohmic contact

This type of contact is capable of filling the carrier deficiency created by photo excitation of the material in presence of applied electric field and the current-voltage (I-V) curve is linear.

4.3.2 Schottky/non-ohomic contact

This type of contact is unable to fill the carrier deficiency created due to photo excitation of the material in presence of applied electric field and I-V curve shows non linearity. To give more insight about the schottky contact behaviour, we have defined few terminologies considering the schematic of schottky contact barrier in Fig. 4.3.
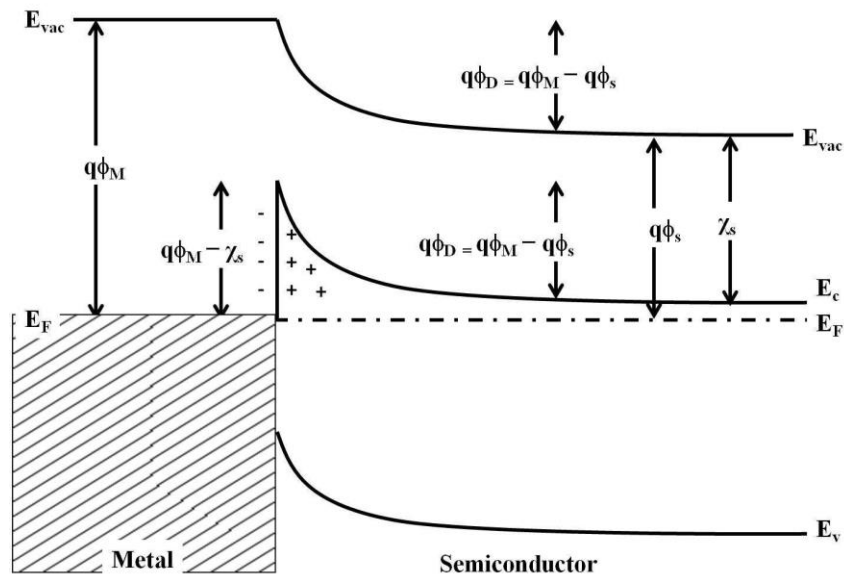
***Figure 4.3:** A Schottky barrier blocking contact between a metal and n-type semiconductor formed when work function of metal is larger than that of the semiconductor. Source ref. [27].*

In Fig 4.3 $q\phi_D$ is the difference of the energy of work function of metal ($q\phi_M$) and semiconductor ($q\phi_s$), diffusion potential is ϕ_D. The barrier height required to cross for a metal-semiconductor for opto-electrical conduction is defined as $\phi = q\phi_M - \chi_S$, χ_S =electron affinity of semiconductor. Now, in case of schottky contact the barrier height becomes larger than $q\phi_D$ by an amount *(E_c -E_F)*, where E_c= energy of the bottom conduction band and E_F= energy of the Fermi level.

For a typical schottky contact with positive metal electrode, current will flow form metal to semiconductor due to rising of the energy level and the expression for the current flow in device is given by equation 4.1 [28]:

$$I(V) = I_0 exp\left(\frac{qV'}{\eta kT}-1\right)\frac{exp\left(\frac{-q(\phi_1-\phi_2)}{kT}\right)}{exp\left(\frac{-q\varphi_2}{kT}\right)+exp\left(\frac{-q\phi_1}{kT}\right)exp\left(\frac{qV'}{\eta kT}\right)}\dots\dots\dots\dots(4.1)$$

where, $V' = V-IR$, R being the series resistance, ϕ_1 and ϕ_2 are the barrier heights for two end contacts of the device in forward and reverse bias respectively, k being the Boltzmann constant and η is the ideality factor of a diode semiconductor, I_0 is current flow across the metal-semiconductor interface by thermionic emission in both direction given by equation 4.2.:

$$I_0 = A*T^2 exp\ (-\phi/k\ T)\dots\dots\dots\dots\dots\dots\dots\dots\dots\dots(4.2)$$

ϕ =barrier height in the metal-semiconductor interface and T = temperature. Illumination can reduce barrier height (ϕ'_s) by carrier generation and enhance photo-current.

In this thesis, measurement on both ohomic contact and non-ohomic contact device was performed. The nano-crystalline film shows ohomic contact whereas needlelike structure film shows schottky contact behaviour.

4.4   Photoconductive Gain

The Photoconductive gain (G) is defined as the number of photons incident on the sample to the number of carriers generated [29]. G is directly related to photo-generated carrier lifetime and transit time given by equation 4.3.

$$G = (N_{carrier}/N_{photon}\ ) = (\tau/\tau_t)= (\mu V/l^2)\tau \dots\dots\dots\dots\dots\dots\dots\dots (4.3)$$

Where, τ= generated carrier life time, τ_t = photo-generated carrier transit time, μ = carrier mobility V = applied bias across the sample and l = sample length.

4.5   Types of photoresponse

Photoresponse study was concentrated on two different types of photoresponse behaviour in oxide thin film. Those are:

4.5.1   Switching (ON/OFF) photoresponse

In this type of photoresponse the current remains low as and when the light/photon is not falling on the sample. This response is described in Fig. 4.4(a), where the minimum current defined as the dark current or OFF state current and the ON state current is defined as Photo current (PC).
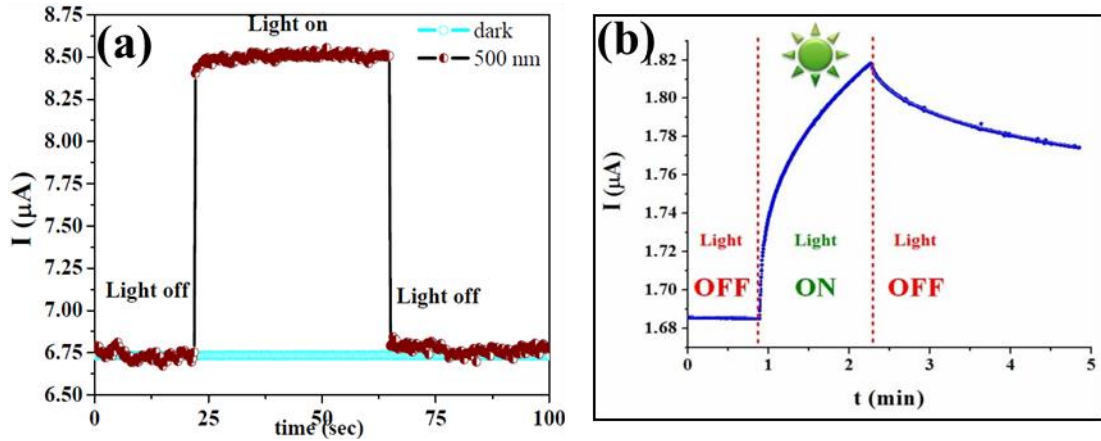
Figure 4.4: *(a) Switching (ON/OFF) response of photocurrent, (b) Persistent Photocurrent response.*

4.5.2   Persistent Photo current (PPC) response

When sample PC raises to its maximum value in presence of light but the current does not go to dark current value upon removal of light, rather it decays exponentially with a higher life time, is called Persistent Photo current (PPC). In Fig. 4.4(b) describe as an example the nature of the PPC with time.

4.6   Opto-electrical property analysis of binary oxide (WO_3): thin film and nanostructures

To study the photo response behavior on WO_3 nanostructures, and to investigate whether there is any effect of surface morphology on opto-electrical behavior, it has been grown on different substrates. Two different substrates SiO_2/Si (SO) (d = 5.4Å) and single crystalline $SrTiO_3$ (STO) (d= 3.905Å) (100) with different lattice parameter has been taken. Growth of WO_3 on SiO_2/Si (SO) and $SrTiO_3$ (STO) (100) substrate using PLD technique, phase and morphology characterizations has been discussed in detail in Chapter 2 Section 2.2.2.1. The

typical PLD parameters both nanocrystalline and needle like structured film is shown in table 4.1.

Table 4.1: _PLD parameters for WO₃ films deposition_

Substrates	*SO*	*STO*
Laser Fluence	*$2J/cm^2$*	*$4J/Cm^2$*
Oxygen Partial Pressure	*30Pa*	*30Pa*
Laser Frequency	*1Hz*	*3Hz*
Deposition Time	*30min*	*30min*
Post deposition annealing	*30min*	*No annealing*

The two WO₃ films grown have different surface morphology as shown in FESEM image (Fig. 4.5 (a-b)). The film on SO shows nanocrystalline nature with grain size 20-30nm (Fig. 4.5(a)), whereas film on STO shows highly oriented (100) needle like structure (Fig. 4.5 (a-b)).
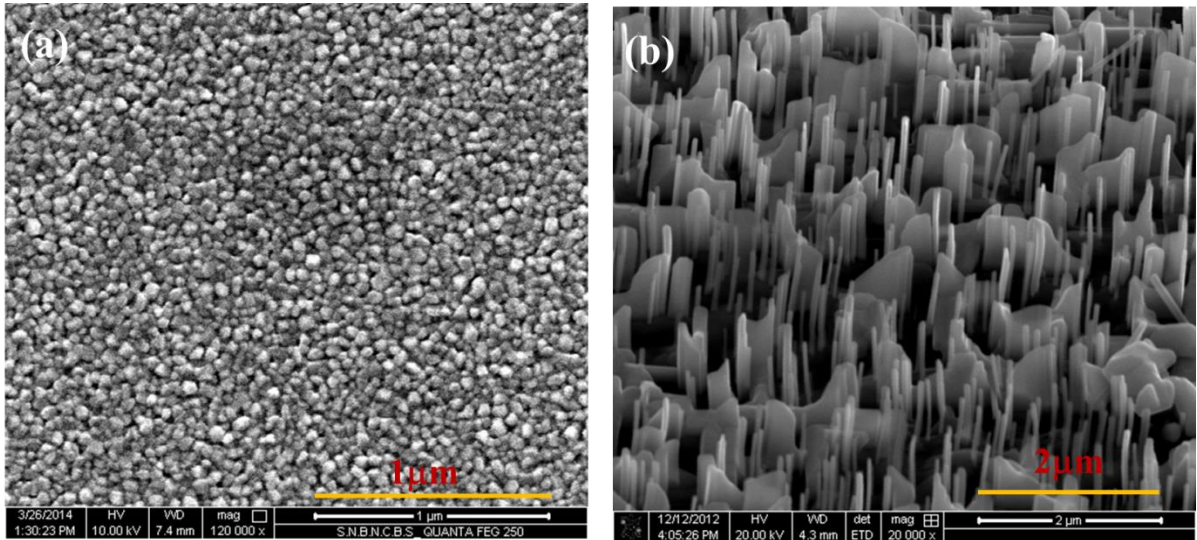
Figure 4.5: *FESEM images (a) nanocrystalline film on SO, (b) needle like structured film on STO*

The microstructural analysis and interesting effect of size, shape, morphology tailoring on photoreponse property of and possible physics behind the response will be discussed in sections 4.6.1 to 4.6.4 and 4.7.

4.6.1   Microstructural and chemical analysis of WO₃ nanocrystalline film

The microstructural and chemical analysis was performed in TEM with GIF (energy filter TEM (EFTEM)) (discussed in chapter 2 section 2.3.1.4). The HRTEM image and selective area diffraction pattern shows crystalline nature of the films and lattice spacing is 3.8Å which is well matched with WO_3 monoclinic structure in Fig. 4.6(a,b) [22]. Chemical analysis of the film using EFTEM mode in GIF confirms the homogeneity of chemical composition of Tungsten (W) and Oxygen (O) of the film using EFTEM Fig. 4.6(c,d) [22].
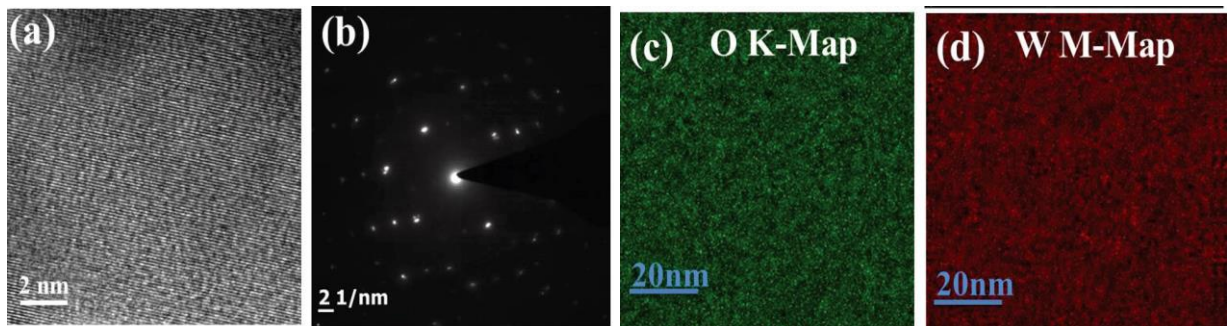
Figure 4.6: *(a) HRTEM image, (b) SAED pattern and (c, d) EFTEM mapping of WO₃ film grown on SO shows Oxygen (O) and Tungsten (W) map.*

4.6.2   Device fabrication and experimental setup for photoresponse measurement

The opto-electrical response was studied on both the WO_3 films. The WO_3 films were deposited in dimension (3mm × 300 μm × 100 nm) on both SO and STO using a metal mask. for fabricating the device and contact pads. The contact pads were made by depositing Cr/Au (10/150nm) using the high vacuum thermal evaporation technique. In Fig. 4.7(a) schematic diagram, of the device and in Fig. 4.7(b) actual image of the device with electrical contacts have been shown.

Schematic diagram of experimental setup using a white light source with monochromator with variable wavelength along with Kithley source meter (Kithley 2400) as a current source has been shown in Fig. 4.8, for the photoresponse measurement. All the measurement was performed at room temperature under different wavelength of light from 300-700nm range using the optical setup with monochromator.
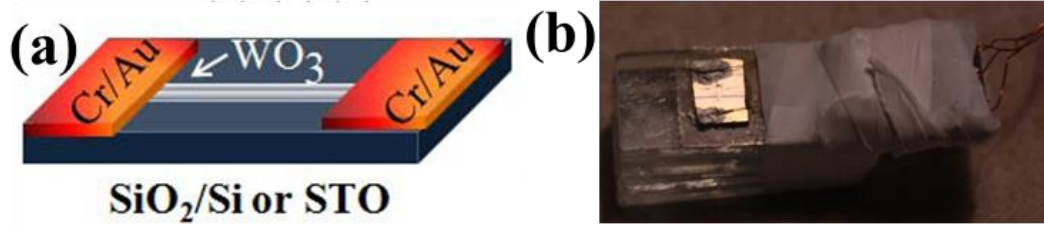
Figure 4.7: *(a) Schematic diagram of the device, (b) Image of the device with electrical contacts*
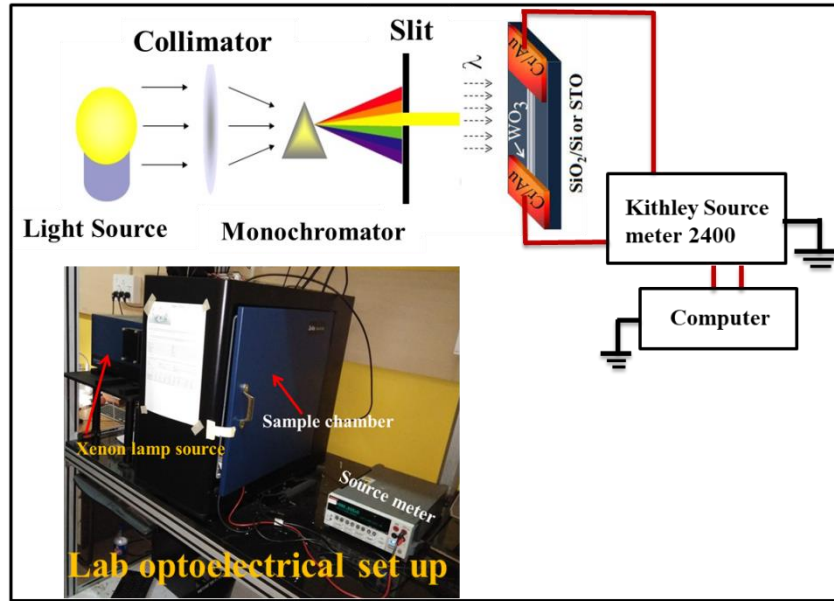
Figure 4.8: *Schematic diagram of experimental setup for photoresponse measurement (Inset: image of our lab opto-electrical setup).*

4.6.3   *Photoresponse measurement on nanocrystalline WO₃ film on SO*

Photoresponse of the WO_3/SO film, current (I)-voltage (V) response at dark (no light) condition as well as at visible wavelength (500nm) were measured. In Fig. 4.9(a) the I-V curve depicts that the contacts are non ohmic in nature (discussed in section 4.2.2 (b)) as the curve has nonlinearity and asymmetry.

The resistivity of the film is 0.04 Ω-cm is calculated from the curve. To study the wavelength dependent electrical response of the film a nominal bias voltage of 0.05V was applied and current (I)-time (t) has been measured starting from light OFF to light ON then again light OFF condition under different wavelengths. In Fig. 4.9(b) the current increases to a maximum value and saturates till the light is ON and goes down to base level (dark current) as light turned OFF, which shows a distinct switching (ON/OFF) response of the device [22].

The wavelength dependent study confirmed that maximum PC is at wavelength 500nm which is actually close to the absorption peak (band to band transition) of WO_3 [22].
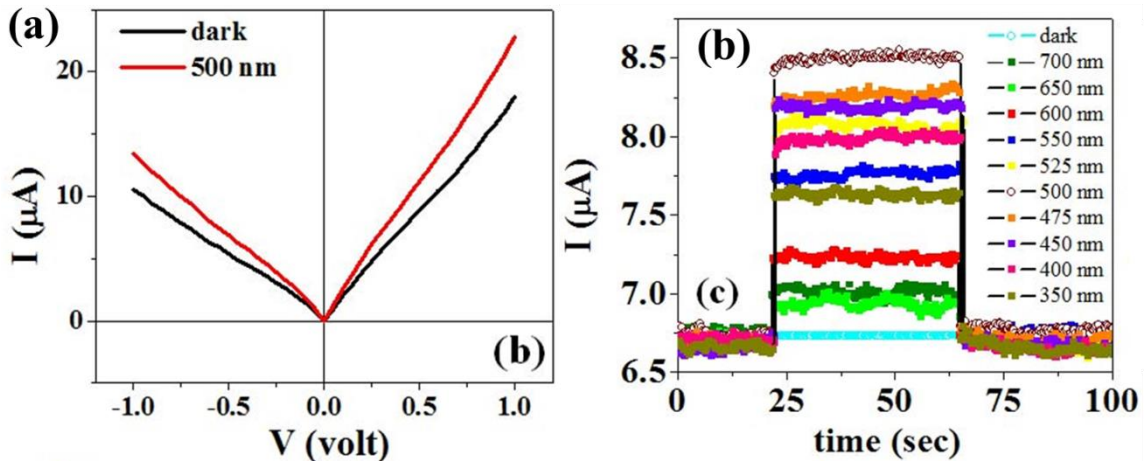
Figure 4.9: *Photoresponse data of nanocrystalline WO_3 film on SO (a) I–V data in dark and under light ($\lambda = 500$ nm), (b) Time dependent photoresponse (I-t) at different wavelengths.*

4.6.4 *Photoresponse measurement on needle like structured WO_3 film on STO*

The above wavelength dependent measurement was also carried out on the needle like structured film, and from the I-V curve (Fig. 4.10(a)) it was observed that the contacts were ohmic in nature (discussed in section 4.2.2 a) as it was linear and symmetric. The resistivity calculated from the I-V data was 0.2 Ω-cm. The photo response measurement showed that film was much more sensitive to light with a nominal 0.1V bias. The sample had a sharp response to light and the current rises very fast and does not go down to dark current value even after the light was turned OFF.

The PC retained for long hours (after turning OFF light) i.e. Persistent Photo current (PPC), has been shown in the Fig. 4.10(b). Time dependent photoresponse curve showed an exponential rise and decay during light ON and OFF respectively [22], which was observed earlier only on a single WO_3 nanowire [16] and other binary oxides [30, 31]. To get more insight about this interesting photoresponse, the curves were fitted using the stretched exponential model. In this model the raising part of the curve follows the equation 4.4 and the decay part follows the equation 4.5 [32]:

$$I = I_{dark} + I_{PC}\left[1 - e^{-(t/\tau_r)^{\beta r}}\right]\ldots\ldots\ldots\ldots\ldots\ldots\ldots..(4.4)$$

$$I = I_{dark}^{\infty} + [I_{max} - I_{dark}]e^{-(t/\tau_d)^{\beta_d}} \ldots\ldots\ldots\ldots\ldots(4.5)$$

Where I_{dark} is the dark current, I_{PC} is the PC, τ_r is the raising time constant, and β_r is the stretched exponential constants. Where I_{dark}^{∞} is the dark current a long time after the removal of illumination and I_{max} is the maximum PC just before the removal of illumination, τ_d is the time constant for decay, and β_d is the decay constant. The equation fitted with photoresponse curve (Fig. 4.10(b)) to estimate the two time constants. Those time constants are plotted with wavelengths as shown in Fig. 4.10(c). The plot showed $\tau_r \sim$ 100 - 200 sec; $\tau_d \sim$ 3000 - 10000s; $\beta_r \sim$ 0:5 - 1, and $\beta_d \sim$ 0:40 -0:50 which comply with the experimentally obtained photoreponse [23].
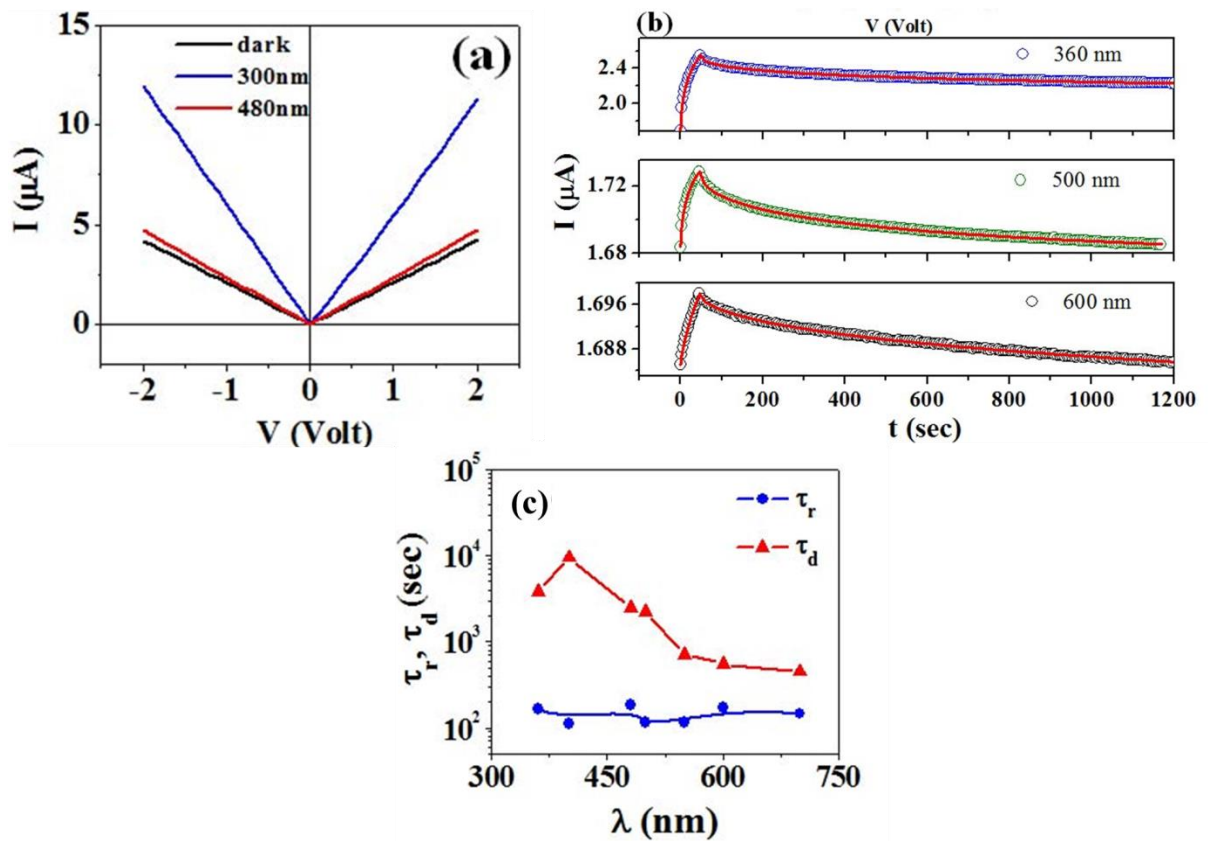
Figure 4.10: *(a) I–V data in dark and under illumination with few representatives λ for bneedle like structured WO₃ film on STO. (b) I-t curve and PPC with and without illumination, respectively, at different wavelengths (λ) represented by symbols, the continuous line represents the fitted curve. (c) The λ dependent raising time constant τ_r and decay time constant τ_d with and without illumination, respectively, as obtained from fitting.*

4.7 Understanding of effect of morphology tuning of WO_3 on photoresponse

Till date the optical/ luminescence study of nanostructured WO_3 showed blue emission response and Near Ultraviolet (NUV) response [17]. Also as an indirect band gap semiconductor luminescence response was very low in case of WO_3 bulk or nanostructures so it was less studied. Very recent investigation on WO_3 nanostructures under different growth temperature provides information about the two different luminescence/optical responses [17]. The band to band transition from typical WO_3 nanostructure was responsible for blue emission whereas, the NUV emission corresponds to oxygen vacancies and surface state defects as well as increase in surface to volume ratio (needle, wire, brunch like structure) [12-13, 17, 33-34]. The surface state defects comes due to the growth parameters, as WO_3 nanostructures possess more defects when grown at comparatively lower temperatures (500-700°C) [35].

In this PLD grown nanostructures it has been observed that the nature of photoresponse was different for two nanostructures.

In Fig. 4.11 wavelength dependent photocurrent gain $[(I_{max}-I_{dark})/_{Idark}]\%$ was plotted, which showed that photoresponse was maximum at 525nm with 27% gain and 360nm with 50% gain for nanocrystalline film and needle like structured film, respectively. As 525nm is near blue emission and at 360nm is near UV emission so the photoresponse for nanocrystalline film corresponds to blue emission and needle like structured film NUV emission.
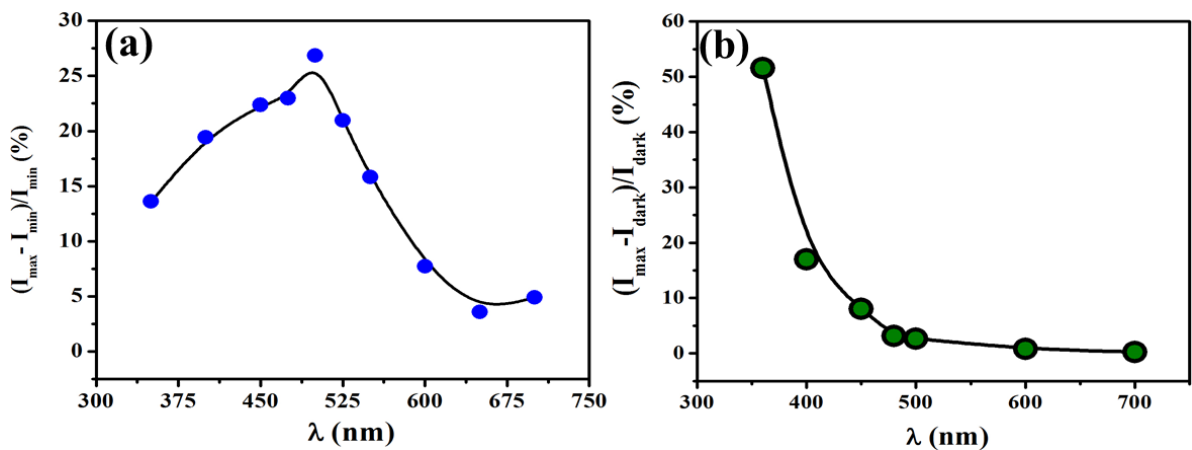
Figure 4.11: *Gain in Photoresponse (a) nanocrystalline film on SO, (b) needle like structured film on STO*

As discussed earlier that the blue emission was due to band to band transition and incase of nanocrystalline film the response was also ON/OFF type, so it validates the swtiching photoresponse behavior. The PPC of WO_3 needle like structured film was due to the surface morphology effect, as increases in surface to volume ratio (needle like structured) also shifts the emission response towards UV region [13, 17, 34]. The surface defect due to oxygen vacancies present in the nanostructures for the low temperature (600°C) growth [35] supports adsorption of oxygen in ambient condition. This may takes place as chemisorption process [22], where chemisorbed oxygen (O_2) which was either adsorbs in the system or desorbs on the WO_3 needle like structured film. The adsorption process is define as the trapping of electron on the film surface by molecular $O_2(g)$ as $O_2(g) + e = O_2^-$ and the release of $O_2(g)$ leaving the electron is desorption process given by $O_2^- + h^+ = O_2(g)$. Considering, WO_3 as an indirect band gap semiconductor another possible reason for this photoresponse/photocurrent may be the generation-recombination process of electron –hole pairs [22].

Now, in case of the film on STO due to needle like structured, the effective surface area was more compared to the nanocrystalline film on SO, so it possesses more chemisorbed O_2 than film on SO. This chemisorbed O_2 prevents the charge carrier recombination and prolonged the photo-carrier life time, hence the persistent photo current (PPC) (discussed in section 4.6.4). Also, the thickness of the film plays an important role, as film on STO had more material compared to film on SO, so it was virtually thicker. Thus, because of the different thickness the PC can be limited in thickest film (on STO) because of charge carrier diffusion length, carrier transport within the film and slow response of the same. It also may be noted that, under light illumination, the photoresponse of a thin film is much rapid than the thicker one due to short optical path length for harvesting photons. This can happen because the thicker film takes longer time to reach an equilibrium state of electron transformation when the illumination state is changed [36, 37].

4.8 Conclusion

In conclusion, WO_3 film and nanostructured film was synthesized using PLD method. It has been observed from the experimental results that photoresponse behaviour is dependent on surface morphology. Here Two morphologically different films (nanocrystalline film and needle like structured film), were obtained. The opto-elctrical behavior was different under light illumination (on/off); the thin film (on SO) showed distinct photocurrent ON/OFF

states, whereas, the nanostructured film (on STO) showed enhanced photocurrent and substantial part of enhanced PC retained over a long period of time as PPC even the illumination was removed. The understanding of possible mechanism behind the response had been discussed in detail.

Bibliography:

1. H. Zheng, J. Zhen Ou, M. S. Strano, R. B. Kaner, A. Mitchell, and K. Kalantar-zadeh Adv. Funct. Mater., 21, 2175–2196, 2011.

2. H. Long, W. Zeng, H. Zhang, J. Mater Sci: Mater Electron, 26, 4698–4707, 2015.

3. M. Yang, N. K. Shrestha, P. Schmuki, Electrochem. Com., 11, 1908–1911, 2009.

4. F. Mitsugi, E. Hiraiwa, T. Ikegami, K. Ebihara and R. Kumar Thareja, Jpn. J. Appl. Phys., 41, 5372–5375, 2002.

5. C. V. Ramana, S. Utsunomiya, R. C. Ewing, C. M. Julien, and U. Becker, J. Phys. Chem. B, 110, 10430-10435, 2006.

6. A. Watcharenwong, W. Chanmanee, N. R. de Tacconi, C. R. Chenthamarakshan, P. Kajitvichyanukul, K. Rajeshwar, J. Electroanalyt. Chem., 612, 112–120, 2008.

7. O. M. Hussain, A. S. Swapnasmitha, J. John, R. Pinto, Appl. Phys. A, 81, 1291–1297, 2005.

8. M. H. Cho, S. A. Park, K.-D. Yang, I. W. Lyo, K. Jeong, S. K. Kang and D. H. Ko, K. W. Kwon, J. H. Ku, and S. Y. Choi H. J. Shin, J. Vac. Sci. Technol. B, 22, 1084, 2004.

9. H. G. Choi, Y. H. Jung, D. K. Kim, J. Am. Ceram., Soc., 88, 6, 1684–1686, 2005.

10. M. Deepa, A. K. Srivastava, S. A. Agnihotry, Acta Mat., 54, 4583–4595, 2006.

11. Z. He, Q. Liu, H. Hou, F. Gao, B. Tang, and W. Yang, ACS Appl. Mater. Interf., 7, 10878−10885, 2015.

12. S. Rajagopal, D. Nataraj, D. Mangalaraj, Y. Djaoued , J. Robichaud, O. Y. Khyzhun, Nanoscale Res. Lett., 4, 1335–1342, 2009.

13. M. Feng, A. L. Pan, H. R. Zhang, Z. A. Li, F. Liu, H. W. Liu, D. X. Shi, B. S. Zou, and H. J. Gao, Appl. Phys. Lett., 86, 141901, 2005.

14. M. D'Arienzo, L. Armelao, C. Maria Mari, S. Polizzi, R. Ruffo, R. Scotti, and F. Morazzoni, J. Am. Chem. Soc., 133, 5296–5304, 2011.

15. E. K. Heidari, E. Marzbanrad, C. Zamani, B. Raissi, Nanoscale Res. Lett., 5, 370–373, 2010.

16. K. Huang and Q. Zhang Nanoscale Res. Lett., 6, 52, 2011.

17. S. Park, H. Kim, C. Jin and C. Lee, Nanoscale Res. Lett., 6, 451, 2011.

18. S. K. Gullapalli, R. S. Vemuri, and C. V. Ramana, Appl. Phys. Lett., 96, 171903, 2010.

19. M. C. Rao, J. Optoelectron. Biomed. Mat., 3, 2, 45–50, 2011.

20. L. Li, Y. Zhang, X. Fang, T. Zhai, M. Liao, X. Sun, Y. Koide, Y. Bandoa and D. Golberg, J. Mater. Chem., 21, 6525, 2011.

21. G. Fang, Z. Liu and K. L. Yao J. Phys. D: Appl. Phys., 34, 2260–2266, 2001.

22. S. Roy Moulik, S. Samanta, and B. Ghosh, Appl. Phys. Lett., 104, 232107, 2014.

23. Semiconductor Laser Diode Technology and Applications, Edited by D. S. Patil, InTech, 2012.

24. E. Fred Schubert, "Light-Emitting Diodes", Cambridge University Press, 2006.

25. I. Yun (Edt.), "Photodiodes-From Fundamentals to Applications", InTech, 2012.

26. R. Basori, *Investigation of Growth, Electrical and Opto-electronic Transport in Nanowires of Charge Transfer Complexes"*, thesis submitted to University of Calcutta, 2015.

27. R. H. Bube, "Photoelectronic Properties of Semiconductors", Cambridge University Press, 1992.

28. H. Norde; J. Appl. Phys., 50, 5052, 1979.

29. J. S. Jie,W. J. Zhang, Y. Jiang, X. M. Meng, Y. Q. Li, and S. T. Lee; Nano Lett., 6, 9, 1887-1892, 2006.

30. S. Mondal, R. R. Ghimire, and A. K. Raychaudhuri, Appl. Phys. Lett., 103, 231105, 2013.

31. R. R. Ghimire, S. Mondal, and A. K. Raychaudhuri, J. Appl. Phys., 117, 105705, 2015.

32. S. Mondal, A. K. Raychaudhuri, Appl. Phys. Lett., 98, 023501, 2011.

33. M. Niederberger, M. H. Bartl, and G. D. Stucky, J. Am. Chem. Soc., 124, 13642-13643, 2002.

34. J. Y. Luo, F. L. Zhao, L. Gong, H. J. Chen, J. Zhou, Z. L. Li, S. Z. Deng, and N. S. Xu, Appl. Phys. Lett., 91, 093124, 2007.

35. K. Lee, W. S. Seo, and J. T. Park, J. Am. Chem. Soc., 125, 3408-3409, 2003.

36. F. Amano, D. Lib, and B. Ohtani, Chem. Commun., 46, 2769, 2010.

37. S. Mridha and D. Basak, Chem. Phys. Lett., 427, 62, 2006.

Chapter 5

Analysis of transport of gas in one dimensional (1D) porous binary oxide nanostructures using Cavity Enhanced Absorption Spectroscopy (CEAS)

In this chapter, the diffusion or transport of gases in one dimensional (1D) porous metal binary oxide (e.g. Tungsten oxide (WO_3) nanostructure grown by hydrothermal synthesis has been studied. The growth parameters are controlled to grow such porous and large aspect ratio (length: diameter) nanostructure. This 1D nanostructure are able to show isotope selective diffusion of gases, like for CO_2, it preferentially allow only one of the stable isotopes, $^{12}CO_2$ to diffuse through it and does not allow the other isotope,$^{13}CO_2$. These phenomena strongly depend on surface morphology, effective surface area and large aspect ratio. The diffusion process has been explained as a physical process following Knudsen diffusion in porous medium. This is completely a new phenomenon which has been explored in this thesis chapter in detail.

5.1. Introduction

One dimensional (1D) nanostructure has fascinated considerable attention in recent years due to their special properties, which make them important in basic scientific research and also in potential technological applications. Binary oxides, like WO_3 is one of the interesting materials because of its potential applications in display devices, optical shutters, nano-electronics and catalysis [1-3]. Furthermore, over the past decades, metal oxides were being used for detection of several gases [4-6]. Studies of these oxide nanostructures were aimed at the formation of high surface to volume ratio as their physical properties were significantly affected by the shape, size, texture and surface morphology. Investigation of opto-electrical properties of nanostructures of WO_3 showed significant variation in photoresponse behavior on modification of surface morphology and surface area [7-8]. However, the transport or diffusion of gases through the large aspect ratio nanostructures of WO_3 is one of the interesting and less understood areas. Directly or indirectly it has an impact on a large class of problems in modern day material sciences. Several reports have been found supporting the gas sensing aspect, and possible origin of this process were generally being described by chemisorption, in last few decades. They were being explained by considering role of adsorbed oxygen [9], Schottky barrier mechanism [10], chemical effects [11] etc. It had to be noted, that one important observation by Sakai et.al reported on the gas diffusion controlled sensitivity using thin film semiconductors was explained on the basis of Knudsen diffusion and a possible theoretical approach had been made about the mechanism [12].

Another more recent application of oxide nanostructures was the diffusion and transport of a gas through large aspect ratio nanowires and nanotubes that leads to isotope selectivity. The process appeared to be guided by physical processes that arise when gas transport through such nanostructures (e.g. WO_3) instead of chemical activities which often claimed before [13].

In last part of this thesis work, the aim was to show how the 1D large aspect ratio binary oxide nanostructures (e.g. nanotubes) with the large surface area and porous surface morphology provided platform for enhancing the diffusion as well as isotopic separation of carbon dioxide (CO_2) gas when it diffused through it.

In this thesis work, it has been observed that, when atmospheric CO_2 gas diffuses through the 1D porous binary oxide nanostructure (e.g. WO_3), it allows only one isotope $^{12}CO_2$ of CO_2, among the two major stable isotopes ($^{12}CO_2$ and $^{13}CO_2$). This process of isotope selective

diffusion of a gas through the nanostructure has been explained as surface sensitive physical processes and not due to chemical activity, as considered before. Generally the surface sensitive physical processes like Knudsen diffusion, laminar flow and surface diffusion are used to describe the transport mechanisms, when a gas passes through some porous mediums [12, 14]. Few reports on transport of mixture of gases through microporous composite membrane were available where gas transport through pores (~2-4 nm diameter) was used to separate out gases from mixture of gases, like mixture of H_2, CO_2 etc. (having different molecular weight) and was also explained using above mentioned physical process [15]. Generally, gas diffusion through porous structures has been explained by chemical activity [14]. But no such report exists where the isotopic separation or fractionation of a gas occur during the transport or diffusion through a porous and large aspect ratio nanostructures of a binary oxide (e.g. WO_3).

In this research work Cavity Enhanced Absorption Spectroscopy (CEAS) [16-18], a spatially resolved tool and technique, have been used for precision measurement of diffused CO_2 isotopes ($^{12}CO_2$ and $^{13}CO_2$) concentration within the material. CEAS along with conventional surface area analysis (Brunauer–Emmett–Teller (BET) analysis) has been carried out in this work, which added a new dimension to this work. It may be noted that such a combination of the above techniques for isotopic gas separation analysis is completely a new approach in this area.

This is the first time such physical processes have been observed for a gas with isotopic enrichment. Also, isotopic gas separation using metal oxides like WO_3 has not been explored or investigated before. Understanding of isotopic gas separation process is also important from the application point of view, as this isotopic fractionation in gases generally has been utilized in geochemistry using the complicated chemical process like mass spectroscopy etc. [19]. Knowledge based on isotope selective diffusion and isotopic fractionation using nanostructures through a physical process will open up an important application potential. Here, how the surface morphology of WO_3 nanostructures (nanotubes, nanowires) facilitates diffusion of CO_2 isotopically from environment has been investigated.

It has also been shown here that use of specific surface morphology of WO_3 nanostructures allows transport of only one of the two major stable isotope of carbon dioxide following some physical process and hence in turn can control isotopic fractionation of CO_2, ($^{12}CO_2$, $^{13}CO_2$) i.e. ratio of $^{13}CO_2$ and $^{12}CO_2$ or $\delta^{13}C$ in gases. It needs to be pointed out that, the aspect of physical process of preferential diffusion of only one isotope ($^{12}CO_2$) of CO_2

through the porous surface of the 1D nanostructures (e.g. WO_3) from a given environment yet not explored. Our experiment thus opens up a new dimension to control isotope ratio in gases which can be used in isotope separation of gases.

5.2. Brief background about isotope and isotopic fractionation

Isotopes of any element have only difference in their number of neutron and no difference in electronic configuration hence having same chemical property. In this thesis work, isotope of carbon has been considered for Carbon dioxide (CO_2) gas. CO_2 gas is a greenhouse gas and in recent time its concentration in environment increasing due to increased pollution level.

CO_2 in environment contain mainly two stable isotopes ($^{12}CO_2$, $^{13}CO_2$). The natural abundance of those isotopes is 98.5% and 1.105% respectively. The analysis on isotope provides information about distribution of stable isotope in a material which may be used for direct inferences regarding diet, trophic level, and subsistence about food available in different climate.

Isotope analysis also provides information about another crucial aspect i.e. isotopic fractionation, which is ratio of non-radiogenic stable isotopes, stable radiogenic isotopes or unstable radioactive isotopes of a material, e.g. in case of CO_2 two stable isotopes are $^{12}CO_2$, $^{13}CO_2$, then isotopic fractionation denoted by $\delta^{13}C$ is an isotopic signature, a measure of the ratio of those stable isotopes i.e. **^{13}C:^{12}C** in parts per thousand (per mil, ‰). Similarly**: δ^{18}O** is ^{18}O: ^{16}O, **δ^{15}N** is ^{15}N : ^{14}N etc. $\delta^{13}C$ has been expressed in following form below:

$$\delta^{13}C_{Sample} = \left(\frac{^{13}C/_{^{12}C \, Sample}}{^{13}C/_{^{12}C \, Standard}} - 1 \right) \times 1000 \, ^0/_{00}$$

$$^{13}C/^{12}C_{standard} = 0.0112372 \, ^0/_{00}$$

The isotope analysis was usually done by Isotope-Ratio Mass Spectrometry (IRMS), to separate different element isotopes on the basis of their mass-to-charge ratios.

5.3. Analysis of transport of gas in 1D binary oxide (WO$_3$) nanostructures

Analysis of transport of gas has been performed in 1D porous WO$_3$ nanostructures (e.g. nanotubes). It has been synthesized in hydrothermal route to achieve porous, large aspect ratio (length: diameter >1). Growth of 1D porous WO$_3$ nanotubes in hydrothermal route, phase and morphology characterizations has been discussed in detail in Chapter 2 Section 2.2.3.2. Microstructural analysis, transport of gas analysis and understanding of possible mechanism are provided in next sections from 5.3.1 to 5.3.3.

5.3.1 Microstructural analysis of 1D WO$_3$ nanostructures

The single crystallinity and presence of pores and average diameter of those nanotubes have been confirmed from the high resolution TEM images shown in Fig. 5.1(a, b). The elemental homogeneity of the constituent elements throughout the individual nanotubes has been confirmed using the Energy Filtered TEM technique and it indicates homogeneous distribution of elements inside the grown nanowires (Fig. 5.1(c, d)). 200kV TECNAI G^2 TF20-ST TEM along with GATAN Quantum 963 electron energy loss spectrometer was used for this analysis.
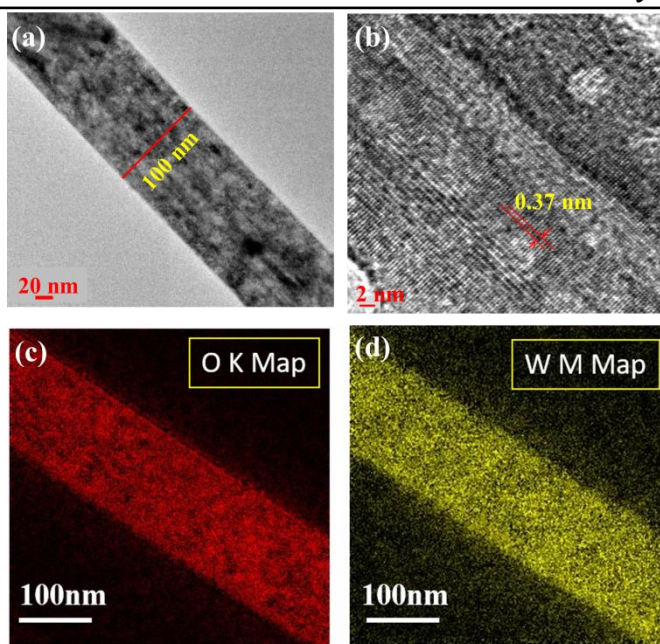
Figure 5.1: *HRTEM images (a) TEM Bright Field image, (b) HRTEM, (c & d) EFTEM mapping of WO₃ nanotubes show homogeneous distribution of constituent elements Tungsten (W) and Oxygen (O) in the nanotubes.*

5.3.2 Transport of gas (CO_2) measurement setup and procedures

WO_3 nanotubes were initially kept in a vacuum sealed cylindrical glass tube at room temperature which was incorporated into a PID controlled heater with a sensor, the typical schematic diagram of experimental setup shown in Fig. 5.2. The experiment was carried out at ambient pressure and in the temperature range between 25-250°C. Initially, the chamber was evacuated to reach a minimum base vacuum then, different concentrations of CO_2 (Mixture of $^{12}CO_2$ (98.42%) and $^{13}CO_2$ (1.105%) natural abundance) were injected into the glass tube through a vacuum-tight septum as fed gas.
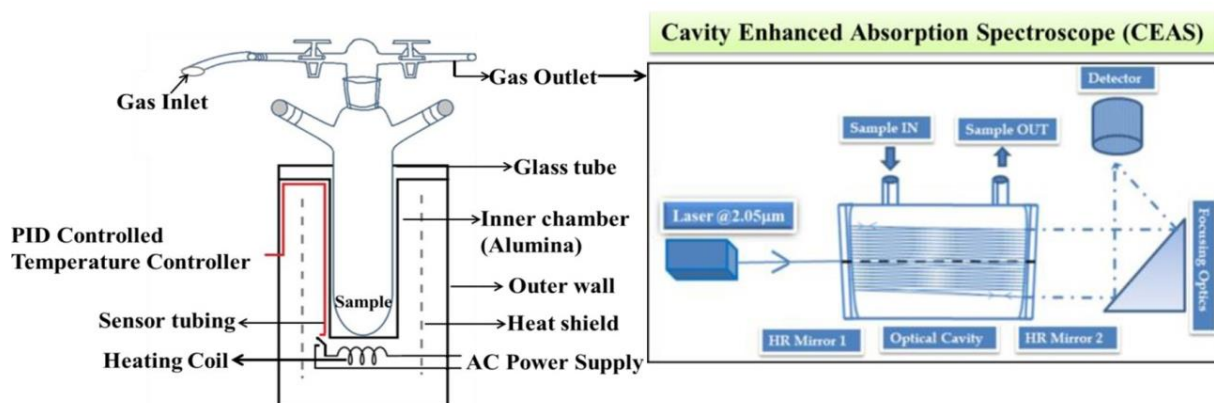
Figure 5.2: *Schematic diagram of experimental set up for CO_2 concentration measurement along with CEAS.*

The sample was heated to the desired temperature and kept to equilibrate. Once the equilibrium is reached, gas samples were collected from the flask at a regular interval with simultaneous heating of nanotubes up to 250°C. Subsequently, collected gas samples were analyzed and isotope specific (i.e. $^{12}CO_2$ and $^{13}CO_2$) concentrations of CO_2 were measured by a high-precision and ultra-sensitive CEAS system (discussed in next section).

5.3.3 Measurement of isotopic CO_2 concentration using CEAS

(a) <u>Cavity Enhanced Absorption Spectroscopy (CEAS)</u>

A laser-based carbon dioxide isotope analyzer (CCIA 36EP, Los Gatos Research) exploiting Cavity Enhanced Absorption Spectroscopy (CEAS) technique for high precision measurements of CO_2 isotopes in gas samples shown in Fig. 5.2 has been utilized [16-18]. A high-finesse optical cavity, comprised of two high reflective mirrors (R≥99.98%) at a distance of ~59 cm, traps the laser intensity inside the cavity coupling laser and cavity modes and thereby providing an effective optical path length of around several kilometers (~3.5 km). A temperature controlled distributed-feedback diode laser (DFB) is employed to scan over 20 GHz around the centre wavelength of 2.05 μm to cover the absorption lines of $^{12}CO_2$ and $^{13}CO_2$ isotopes at the wavenumbers of 4874.448 cm^{-1} and 4874.086 cm^{-1}, respectively in a single laser sweep. The selected absorption features of $^{12}CO_2$ and $^{13}CO_2$ isotopes are the r$_o$-vibrational lines arising from the R(28) and P(16) rotational transitions of the $(2v_1 + v_3)$

vibrational combination band of CO_2 molecule, respectively in this spectral region. The high-resolution absorption spectra were fitted with Voigt line-shape function in real-time to calculate the absolute concentration of $^{12}CO_2$ and $^{13}CO_2$ isotopes in accordance with Beer-Lambert law.

The temperature of the cavity is controlled at around 46°C by a resistive heater and feedback control system whereas pressure of 30 Torr is maintained inside the optical cavity through a diaphragm pump. Mass flow controllers (MFC) connected with solenoid valve is utilized to control the flow of gas samples inside the cavity. The accuracy and precision of the CO_2 spectrometer were examined by utilizing different calibration standards from CIL (Cambridge Isotope Laboratory, USA), measured by Isotope-Ratio Mass Spectrometry (IRMS) with known concentrations of $^{12}CO_2$ and $^{13}CO_2$ isotopes provided in Table 5.1

Table 5.1: _Calibration of $\delta^{13}C$ (‰) measurements: Comparisons of the $\delta^{13}C$‰ values measured by CEAS method (CO_2 isotope analyzer) with the certified calibration standards (Cambridge Isotope Laboratory, USA). 1SD represents the one standard deviation of five successive measurements_.

Certified $\delta^{13}C$ ‰ calibration standards analyzed by IRMS	$\delta^{13}C$ ‰ (±1SD) measured by CEAS
-22.71	-22.69 ± 0.05
-15.5	-15.50 ± 0.05
-9.69	-9.71 ± 0.05

(b) _Analysis of CO_2 diffusion concentration in 1D WO_3 nanostructures using CEAS_

High precision estimation of concentration of CO_2 and its isotopes inside WO_3 nanostructures was done exploiting CEAS. In Fig 5.3(a) CEAS measurements show diffusion (decrease of CO_2 concentration from the initial value) of CO_2 in WO_3 nanotubes with large aspect ratio (length: diameter) as a function temperature at various initial concentrations of CO_2 (Case I-IV), in the vacuum sealed chamber. The Case I-IV represents the different initial concentrations of CO_2 ranging from 270 ppm to 530 ppm. In Fig. 5.3(a) (black curve) no

change in CO_2 concentration i.e. no diffusion occurs when initial concentration (case I) of CO_2 is well below 300 ppm (here 270 ppm). As the initial concentration increases (Case II-IV), diffusion of CO_2 increases (Fig 5.43(a)). The maximum diffusion occurs at 200 °C (Case I-IV). Thereafter, the diffusion of individual isotopes of CO_2 has been studied. The isotope specific diffusion of CO_2 has been plotted in Fig. 5.3(b) and the solid curve represents the change in concentration of $^{12}CO_2$ isotope and dotted curve for $^{13}CO_2$ isotope. For different initial concentrations (ppm) of CO_2 (case II-IV), it has been observed from Fig. 5.3(b) that the porous WO_3 nanotubes allows the diffusion of $^{12}CO_2$ isotope only and it does not allow $^{13}CO_2$ isotope (dotted curve) to diffuse through it. Thus two isotopes of carbon dioxide gas become separated by this isotope selective diffusion process via porous large aspect ratio nanotubes of WO_3.
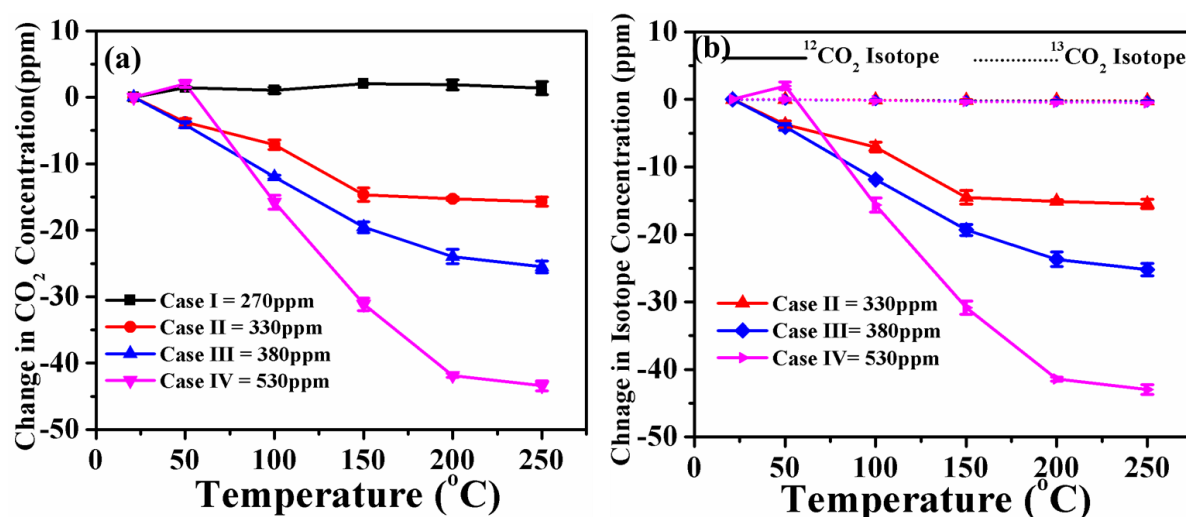
Figure 5.3*: (a) CO_2 diffusion in WO_3 nanotubes under different CO_2 concetration and temperature, (b) $^{12}CO_2$ and $^{13}CO_2$ diffusion concentraion in WO_3 nanotubes.*

The isotope selective diffusion of CO_2 through the nanostructured WO_3 has not been reported before. In natural abundance the concentration of $^{13}CO_2$ is very low (1.105%) so to validate the isotope selective diffusion through WO_3 nanostructures, experiments were done in enriched $^{13}CO_2$ conditions. The enrichment was done up to 65% in the environment of experimental vessel and the concentration of $^{13}CO_2$ has been plotted in Fig 5.4(a) for different enriched concentrations of $^{13}CO_2$ ranging from 1.1-65% (Enrichment I-IV) in total CO_2 ($^{12}CO_2$ and $^{13}CO_2$ mixture). It has been observed that enriched concentration of $^{13}CO_2$ does not show any change from initial value which eventually signifies no diffusion through the WO_3 nanotubes. The repeatability of isotope selective transport nature of WO_3 nanostructures

was checked by performing the experiment for several numbers of cycles. Plot of $^{12}CO_2$ diffusion by the regenerated and recycled nanotubes up to 50 cycles has been shown (Fig 5.4(b)) and found that the porcess is rerevisble and sample has good recycleability.
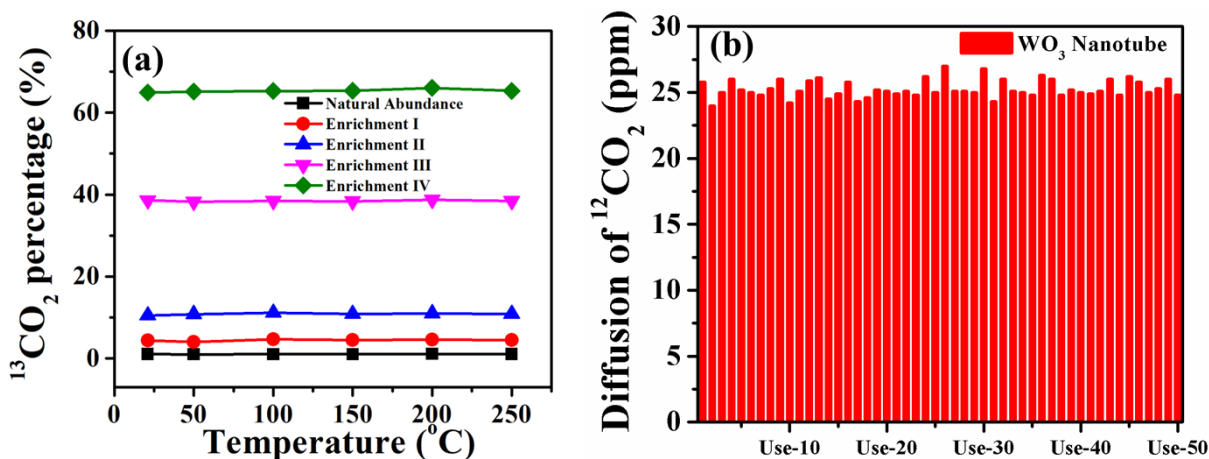
Figure 5.4: *(a) No diffusion of $^{13}CO_2$ under enriched $^{13}CO_2$ condition (enrichment I-IV), (b) Reproducibility of diffusion of $^{12}CO_2$ by reusing the nanotubes 50 times.*

(c) *Role of surface morphology and porosity during diffusion of CO_2 through 1D binary oxide nanostructures*

Surface area and the porosity of the nanostructures of WO_3 were estimated by BET measurement and observed that nanotubes have larger surface area and larger pore volume compared to nanowires WO_3 micro and nano particles (Source: Sigma Aldrich and US research nanomaterial, respectively). However, BET analysis shows that the pore diameter is same in both nanowires and nanotubes (Table 5.1). In Fig. 5.5(a) Schematic diagram of a porous WO_3 nanotube has been shown.

It has been observed from BET analysis (Table 5.2) that surface area is larger in case nanotubes. Also concentration of CO_2 diffusion (change in CO_2 concentration form initial concentration of 400 ppm) within nanotubes of WO_3 is the maximum among the other nanostructures. Diffusion of CO_2, through Bulk WO_3 and nanoparticles was almost zero (Fig. 5.5(b)).

Table 5.2: BET analysis data of WO_3 nanostructures

Sample	Surface area (m^2/g)	Pore Vol (cc/g)	Pore dia (nm)
WO_3 nanowire	39.38	0.169	3.956
WO_3 nanotube	201.227	0.583	3.952
WO_3 bulk	3.11	0.034	57.268
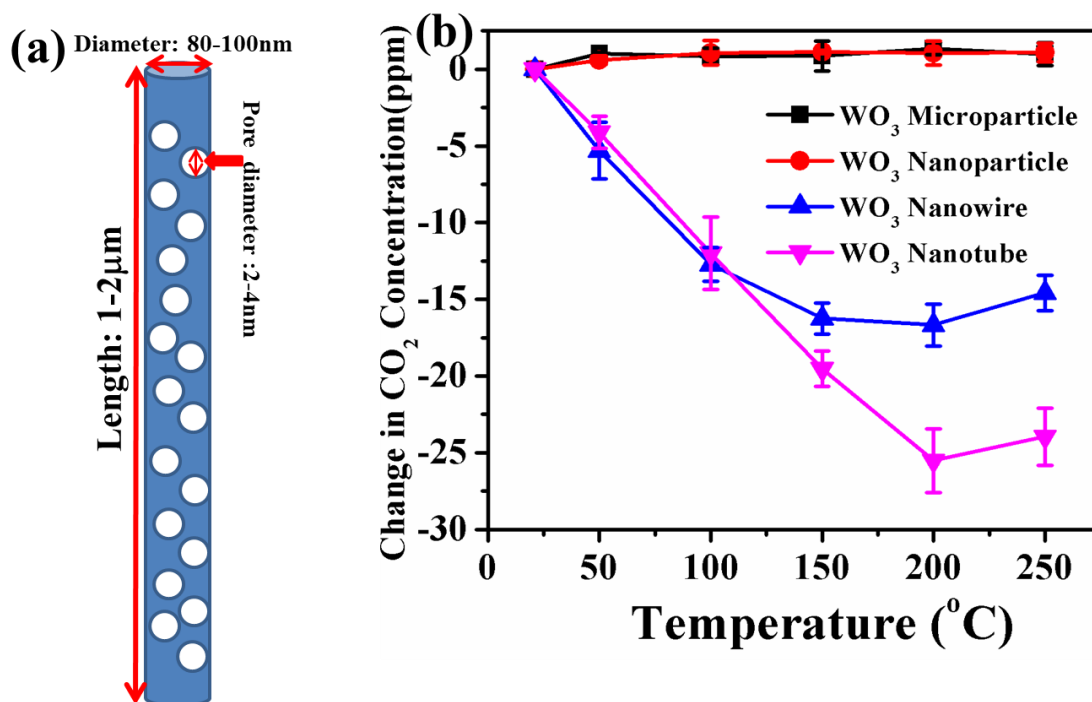
Figure 5.5*: (a) Schematic diagram of porous WO_3 nanotube, (b) Temperature dependent CO_2 diffusion in different WO_3 nanostructures and micron particles (Initial CO_2 concentration = 400 ppm).*

We propose that it is a surface induced phenomena and transport through the surfaces of nanostructures occurs by a physical process only. Bulk WO_3 does not show any diffusion of gas, as the surface area was very less than the other nanostructures (Table 5.1).

The porous 1D nanostructured of WO_3 allowed the gas to diffuse through it, the amount of gas diffused through it, was estimated by using CEAS technique. While analyzing through the laser based spectroscopy, it has been noticed that the system allows to diffuse only one isotope, $^{12}CO_2$ (Fig 5.3b) and does not allow $^{13}CO_2$ to diffuse. In atmosphere as the concentration of $^{13}CO_2$ is very low (1.105%). For confirmation of the novel phenomena, the enrichment of $^{13}CO_2$ was done in the experimental environment and no diffusion of $^{13}CO_2$ observed (Fig. 5.4(a)). Hence, in this process of isotope selective phenomena of porous 1D

nanostructured WO_3, two major stable isotopes ($^{12}CO_2$, $^{13}CO_2$) of CO_2 turn out to be separated.

Hence fractionation of isotopes occurs by the physical process like diffusion. This phenomenon of isotope selective diffusion of $^{12}CO_2$ through pores (□4nm) on the surface of nanostructures of WO_3 has not been observed before. Most of the available methods for isotope fractionation reported earlier, involved different rigorous sample preparation and use of costly apparatus for isotope separation involving laser source, gas chromatography, and mass spectrometry [19-23].

The possible mechanism of isotope selectivity by the nanostructures may be discussed considering it as a physical process. Generally, during transport through porous medium, diffusion of gas molecules may occur in three ways; through pore volume, along pore surfaces and through the solid matrix media of the nanotubes. Several factors are involved in the pathway of diffusion but a large fraction of diffusion occur through pore volume in all the temperature range (ambient to higher temperature), unless the pore volumes and the permeability are very low. For very low pore diameter (~few nm) of a porous medium, part of the total diffusion may follow the Knudsen type [12, 14-15]. If the pore diameter of a porous surface are smaller than the mean free path of the gas molecules, light weight molecules pass faster than the heavy one, according to Knudsen, average velocity of gas molecules is inversely proportional to the square root of the molecular mass following the equation 5.1:

$$V_{avg} = (8RT/\pi M)^{1/2} ....(5.1)$$

Where, V_{avg} is the average velocity of the gas molecules, M is the molecular mass, T is the temperature and R is the gas constant [15].

Few reports on the transport of gases through the porous membranes (pore diameter of ~nm level) where porous membranes were used to separate out gases from mixture of gases of different molecular weight [15, 22] and was explained by some physical process like, Knudsen diffusion, laminar flow and surface diffusion etc. Separation of Uranium isotope through porous membranes was also explained by Knudsen diffusion [24].

The gas separation factor can be influenced by introducing an interaction between the pore walls, which results in an additional transport along the surface. Molecules adsorbed on the solid surfaces can have appreciable mobility and hence additional transport of gases has to be considered as a surface flow. Several reports on surface diffusion along the porous surface were made considering the diffusion of gas [25-28].

In case of gas transport through the nanostructures with large aspect ratio of length: diameter~ 20:1 or more, with porous surface, where, pore diameter are small ~ 2-4 nm, porous surface can act like porous membrane, two types of diffusion may occur as demonstrated above. The part of total transport through the small pore diameter ~2-4 nm can be considered as Knudsen type, and the large surface area of the nanostructures could introduce additional transport via surface diffusion. The larger surface area ($201m^2/g$) of nanotube was responsible for the surface diffusion.

Here, the transport of carbon dioxide through the 1D porous nanostructures of WO_3, where the pores on the surface act as capillary has been focused. One of the two major stable isotopes of carbon-dioxide, $^{12}CO_2$ which is lighter weight passes through the capillary of the nanotubes and as a result, soon a small pressure difference is created which caused an overall back flow and opposes the flow of higher molecular weight $^{13}CO_2$ molecules compare to $^{12}CO_2$ through the nanotubes. As the surface area increases due to large length, the probability of surface diffusion increases, the diffusion of $^{12}CO_2$ through the nanotubes with larger surface area (as estimated from BET analysis) compared to nanowires increases. The increase of temperature increases the flow as well as adsorption through the nanotubes following the normal diffusion process.

5.4. Conclusion:

In conclusion demonstration of isotope selective transport of carbon dioxide in 1D nanostructure (e.g. nanotubes) with porous surface morphology has been provided. The transport of one of the stable isotopes of carbon dioxide, i.e. $^{12}CO_2$, can be explained by Knudsen diffusion along with surface diffusion process. The diffusion strongly depends on the porosity, morphology of the WO_3 and it is not an inherent property of WO_3.This isotope selective capability can be utilized for isotopic fractionation in a gas.

Bibilography

1. S. Hoseinzadeh, R. Ghasemias, A. Bahari, A. H. Ramezani, J Mater Sci., Mater Electron, 28, 14446, 2017.

2. R.M. Fernández-Domene, R. Sánchez-Tovar, B. Lucas-Granados, G. Roselló-Márquez, J. García-Antón, Mat., and Desg., 116, 160–170, 2017.

3. J. Zhoua, S. Lina, Y., Chena, A. M. Gaskovc Appl. Surf. Sci., 403, 274–281, 2017.

4. W. Yan, M. Hu, P. Zeng, S. Ma, M. Li Appl. Surf. Sci., 292, 551–555, 2014.

5. L. Saadia, C. Lambert-Mauriata, V, Oisona, H. Oualib, R. Haynaa Aix, Appl. Surf. Sci., 293, 76–79, 2014.

6. Y. Li, W. Luo, N. Qin, J. Dong, J. Wei, W. Li, S. Feng, J. Chen, J. Xu, A. A. Elzatahry, M. H. Es-Saheb, Y. Deng, and D. Zhao, Angew. Chem. Int. Ed., 53, 9035–9040, 2014

7. S. Roy Moulik, S. Samanta, and B. Ghosh, Appl. Phys. Lett., 104, 232107, 2014.

8. K. Huang and Q. Zhang Nanoscale Res. Lett., 6, 52, 2011

9. N.Yamazoe, J. Fuchigami, M. Kishikawa, T. Seiyama, Surf. Sci., 86, 335-344, 1979

10. K. Ihokura, in: M. Nagayama, E.B. Yeager (Eds.), New Materials and New Process 1. JEC Press Inc., p. 43,1981

11. N. Yamazoe, Y. Kurokawa, T. Seiyama, Catalytic sensitization of SnO_2 sensor, in: T. Seiyama, K Fueki, J Shiokawa, S. Suzuki (Eds.), Proceed of the International Meeting on Chem. Sens., Fukuoka, Japan, September, pp. 35-40, 1983.

12. G. Sakai, N. Matsunaga, K. Shimanoe, N. yamazoe, Sen. Act. B, 80, 125-131, 2001.

13. S. Roy Moulik, A. Maity, M. Pal, M. Pradhan and B. Ghosh, Indian Patent Filed No. 201731017087 dated: 16/05/2017.

14. Y. F. Sun, S. B Liu, F. L. Meng, J.Y. Liu, Z. Jin, L. T Kong. and J. H. Liu, Sensors, 12, 2610-2631, 2012

15. K. Keizer, R. J. R. Uhlhorn, R. J. Van Vuren and A. J. Burggraaf, J. Mem. Sci., 39, 285-300, 1988.

16. E. R. Crosson, K. N. Ricci, B. A. Richman, F. C. Chilese, T. G. Owano, R. A. Provencal, M. W. Todd, J. Glasser, A. A. Kachanov, B. A. Paldus, T. G. Spence, R. N. Zare, Anal Chem.74, 2003–2007, 2002.

17. A. Maity, G. Banik, C. Ghosh, S. Som, S. Chaudhuri, S. Daschakraborty, S. Ghosh, B, Ghosh, A. K. Raychaudhuri, M. Pradhan, J. Breath. Res., 8, 016005, 2014.

18. A. Maity, M. Pal, S. Som, S. Maithani, S. Chaudhuri, M. Pradhan., Anal. Bioanal. Chem., 409, 1, 193-200, 2017.

19. B. Peterson and B. Fry, Ann. Rev. Ecol. st., 18:293-320, 1987.

20. S. Civiš, M. Bouša, A. Zukal, A. Knížek, P. Kubelík, P. Rojík, J. Nováková, and Martin Ferus, J. Phys. Chem. C, 120, 508−516, 2016.

21. C. R. Mckinney, J. M. Mccrea, S. Epstein, H. A. Allen, and H. C. Urey, Rev. Sci. Instr., 21, 724-730 1950.

22. A. W. Hilkert, C. B. Douthitt, H. J. Schluter and W. A. Brand, Rapid Commun. Mass Spectrom., 13, 1226–1230, 1999.

23. W. Meier-Augenstein, J. Chromatogr. A, 842 351–371, 1999.

24. E. van Halle, Gaseous Diffusion, Aerodynamic Separation of Gases and Isotopes, Van Karman Institute for Fluid Dynamics, 1978, 8th lecture series

25. H. H. Li, F. L. Meng, Y. F. Sun, J. Y Liu, Y. T. Wan, B. Sun, J. H. Liu, Procedia Eng., 7, 172-178, 2010.

26. Z. Guo, M. Q. Li, J. H. Liu, Nanotech., 19, 2008, 245611.

27. G. X. Wang, J. S. Park, M. S. Park, X. L. Gou, Sens. Actuat. B, 131, 313-317, 2008.

28. Y. Jia, L. F. He, Z. Guo, X. Chen, F. L. Meng, T. Luo, M. Q. Li, J. H. Liu, J. Phys. Chem. C, 113, 9581-9587, 2009.

Chapter 6

Summary and concluding remarks

In this chapter, summary and important observations of this thesis work have been provided along with scope for future works. The mainfocus of this dissertation is the synthesis of vertically aligned one dimensional (1D) nanostructure of binary oxide and the mechanism governing the growth. In this thesis, we mainly focused on the synthesis, mechanism of growth, detailed characterization and physical property study of binary oxide. This thesis led to definite results as growth of high quality single crystalline binary oxide nanostructures was possible. All the important observations obtained during this thesis work are mentioned below.

6.1. Conclusion

In this thesis, the effect of modification of growth techniques and parameters in tailoring size, shape, morphology, crystallinity, and homogeneity of binary oxide nanostructures has been provided. The main interest to standardize different synthesis techniques for the growth of vertically aligned 1D binary oxide nanostructures, 1D porous binary oxide nanostructure (mainly on WO_3) and understand possible physics behind the growth dynamics have been achieved in this thesis. Further, this thesis establishes the tailoring of size, shape, morphology, and crystallinity of binary oxide nanostructures can tune the physical properties found in bulk counterpart of binary oxides (mainly WO_3). The main observations found in this thesis work were as follows:

(1) In chapter 2, detail growth of WO_3 thin film and nanostructure using Pulse Laser Deposition (PLD) and the hydrothermal synthesis of TiO2 nanorods, has been provided. The growth parameter tuning and effect of tuning upon surface morphology and crystal structure has been performed using different characterization tools (XRD, SEM, and TEM). A brief detail of different instruments and techniques also has been provided for a better understanding of the characterization method.

(2) In chapter 3, the interface physics and surface chemistry of binary oxide nanostructures (nanowires, nanorod) has been provided. The synthesis was done using PLD and hydrothermal route. Spatially resolved tools for developing the cross-sectional sample have been utilized and analysis provides the information lies at the interface about growth dynamics. The X-TEM analysis provides information on the formation of the interfacial layer when laser energy increased above a certain value (>160mJ). This acts as a nucleation site to grow aligned 1D nanostructure array. The mechanism behind this growth has been proposed as preferential interface nucleation (PIN) growth mode. In surface chemistry analysis EELS technique shows the changes in the chemical state of nanorods due to growth in different substrates (FTO, Pt(111)/Si). The analysis also provides interesting information about the anisotropic growth of TiO_2 nanorods and nanoflowers on Pt(111)/Si substrate due to crystal structure mismatch.

(3) In chapter 4, tuning the growth parameters for the WO_3 thin film and nanostructure using pulsed laser deposition (PLD) technique and by changing the substrate, it is possible to modify the surface morphology of the film. The modified morphology helps us to tune the nature of photoresponse. The grown nanocrystalline film and needle-like structure film shows ON/OFF and Persistence photocurrent (PPC) in photoresponse property respectively, which has been observed for the first time. The increase in effective surface area in case of needle-like structure film helps to adsorb higher number of chemisorbed oxygen which prolongs the charge carrier recombination and PPC observed.

(4) In chapter 5 the gas diffusion/transport property of binary oxide nanostructure of WO_3 has been observed. In this chapter we have coupled the high resolution laser spectroscopy tool to understand the gas transport through the porous nanostructures of binary oxides. The analysis in diffusion concentration using cavity-enhanced laser spectroscopy shows isotope selective diffusion of CO_2 inside the nanostructure, i.e $^{12}CO_2$ diffuses through the nanostructure although no diffusion occurs for $^{13}CO_2$. Thus, gas transport property gave us a new direction to control greenhouse gas emission by gas diffusion, a physical process, using 1D porous nanostructure grown by this controlled growth technique, which opens up an advanced phenomenon (isotopic fractionation). This is a new observation and till date, no reports are present in the diffusion property of binary oxides. The diffusion of gas increases with the increase in surface area of the nanostructure (higher in nanotubes then nanowires), has been noted. This mechanism has been proposed as physical process considering famous Knudsen diffusion where diffusion in nanostructures having pore diameter less than mean free path of gases depends inversely on the molecular mass of the gas. This diffusion property opens up new aspect for a different application of 1D porous nanostructure of binary oxides.

6.2. Scope for future works

1. Vertically aligned nanowires of other binary oxides (e.g ZnO, TiO_2) using PLD, different can be grown on different substrates to study role of interface and its effect on physical property.

2. Morphology dependent physical property study like, electrical property and photoresponse property, in vacuum for binary oxide nanostructure can be performed in future scope to explore the modification of those properties.

3. Photocatalytic property study of TiO_2 nanorods arrays grown on FTO for solar cell application can be studied.

4. Hydrothermal growth of binary oxide nanostructures with different morphology and crystal structures can be grown to study the effect of growth parameters.

5. Isotope selective gas diffusion in 1D porous binary oxide nanostructure can be explore to develop application of these unique property in the field of isotopic fractionation, food adulteration, biomedical sciences etc.

Appendix A

Electric Double Layer Field Effect Transistor (EDL-FET) characteristic study of WO$_3$ thin film

In this appendix the Electric Double Layer (EDL) gate dependent Field effect transistor (FET) characteristics of WO$_3$ nanocryatalline film grown by Pulse Laser Deposition (PLD) technique has been discussed. The response of the FET enhanced due to application of EDL gate voltage and at a threshold voltage of 1V the FET goes to its ON state. Presence of defect state in WO$_3$ thin film may be helping the FET to enhance its conductivity due to application of gate bias using polymer electrolyte based EDL gate. Although intercalation property and the electrochromic effect of WO$_3$ and gate dielectric in presence of gate voltage restrict the response due to non-reproducibility of FET characteristics.

A.1 Introduction

In the earlier time Metal oxide FET were used for amplifying or switching signals which has a very low value for magnification. In recent few decades ionic liquid such as DEME-TFSI, DEME-BF$_4$ or solid liquid (PEO-LiCl$_4$, PEO-KCl$_4$) were used as a gate dielectric material to modify or develop physical properties of binary oxides, functional materials etc. [1-4]. These ionic liquid or solid liquid forms Electric Double Layer (EDL) at the solid electrolyte surface which creates a large specific capacitance ($\geq 1\mu Fcm^2$), which in turns produces large charge density ($\geq 10^{13} cm^2$) even with a bias as low as 1V. Oxides have greater electron density compared to semiconductors, thus for conventional gate induced charge density is much less than the electron density. So there is no effect of dielectric based gate insulator on oxide channels. In case of electrolyte gate the induced charge order of magnitude is higher compared to conventional gate insulator (SiO$_2$, SrTiO$_3$ etc.) with same minimal bias (1V). So the electrical transport property in oxides may be controlled by electrolyte gates, as it strongly depends on charge carrier density. Controlling of the carrier density using electrolytes or ionic liquids results in very interesting properties like metal insulator transition [5], superconductivity [6], magnetism in nanoparticles [7] and EDL–Field Effect Transistor (FET) showing modified photoconductivity [4]. Those properties have been studied on different binary oxides ZnO, VO$_2$ [4, 6, 8] and functional oxides such as SrTiO$_3$, KTaO$_3$, La$_{0.75}$Sr$_{0.25}$MnO$_3$, NdNiO$_3$, Ca$_{1-x}$R$_x$MnO$_3$, LaMnO$_3$ [2, 5, 7, 9-11].

In an EDL-FET electrolyte with mobile ions (cations and anaions) are filled in between two electrodes, which act as an EDL capacitor (Fig. A.1). In presence of external electric field double layers are formed between electrolytes and electrodes consisting of the space charge at electrode and ion space charge in the electrolyte. The external voltage charges the EDL-FET, which causes the movement of cations and anaions to the surface of EDL. The absorption and desorption of ions during EDL-FET charging controls the operation for the same. Many theories had been proposed for the explanation of this phenomenon among them the Von Helmholtz, Gouy and Chapman model, Stern model were comprehensive. In Von Helmhotz model (Fig. A.2(a)) charged surface of the electrode adsorb opposite ions form electrolytes and the potential profile is linear inside the EDL. This is much more analogous to a dielectric capacitor separated by a distance H. Afterwards Gouy and Chapman proposed the

diffusion of ions inside electrolytes. The distribution of charges in ions is a function of distance from the metal surface and follows Maxwell-Boltzman statistics (Fig. A.2(b)).
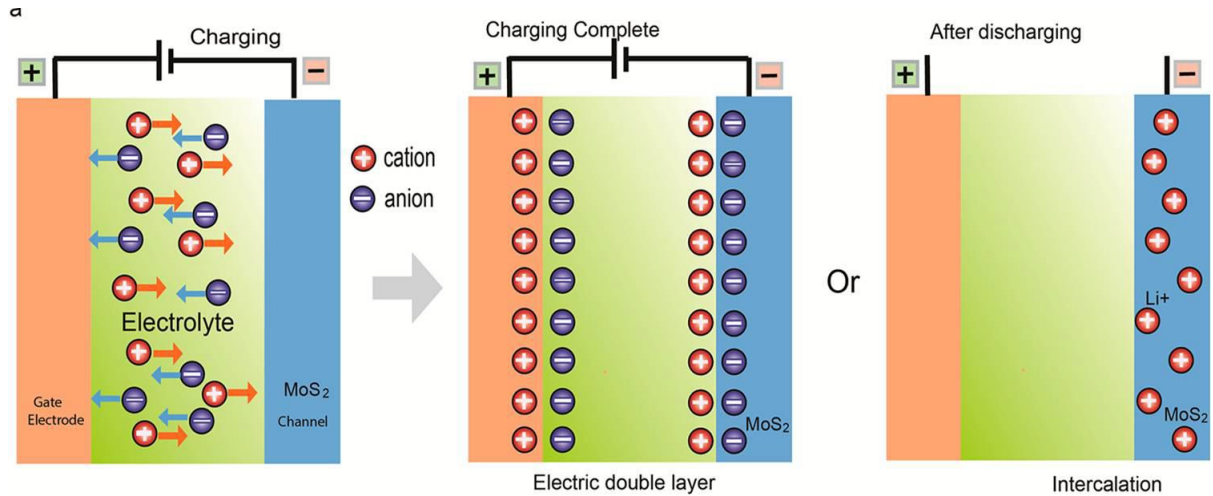
Figure A.1: Charging and discharging of EDL capacitor. Reprinted with permission © 2015, ACS Publication [12]
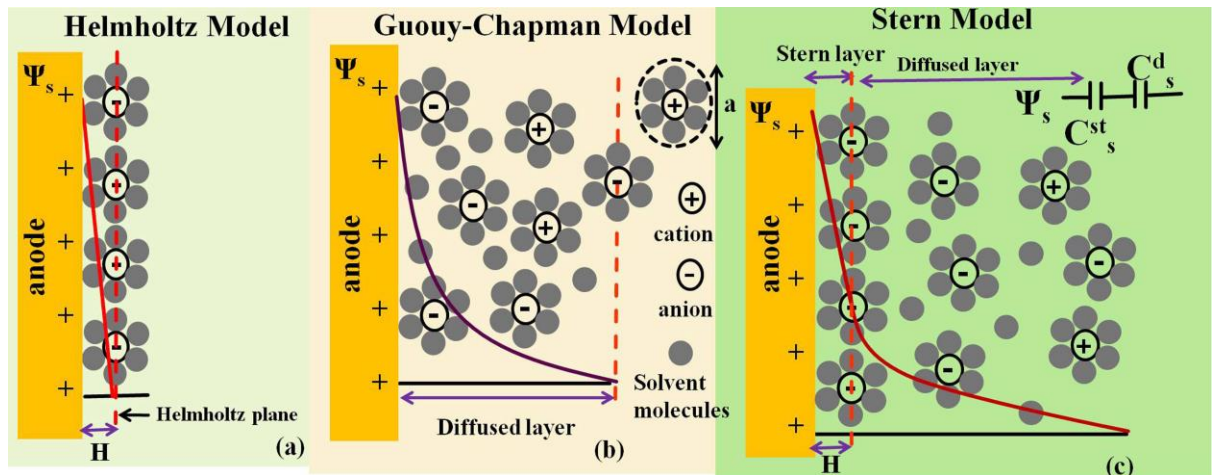
Figure A.2 (a-c): Simplified illustration of the potential development in the area and in the further course of a Helmholtz double layer. Reprinted with permission © 2011, ACS Publication. Source, modified version ref. [13, 14]

Thus the electric potential from the surface of the liquid decreases exponentially.

Lastly the Stern model partially is in good agreement with Helmholtz model (Fig. A 2(c)). In this model Stern defined a layer named Stern Layer which is similar to Helmholtz plane or Layer. The distance between Stern Layer and the diffuse layer is proportional to the concentration of ions. The total EDL capacitance is a sum of Stern layer capacitance (C_S^H or C_S^{st}) and Diffuse layer capacitance (C_S^D) in series. Helmholtz double layer specific capacitance is given by equation A.1 [12]:

$$C_S^H = \frac{\varepsilon_0 \varepsilon_r}{H} \ldots\ldots\ldots\ldots\ldots\ldots\ldots\ldots.(A.1)$$

Where $\varepsilon_0, \varepsilon_r$ are free space and relative permittivity of electrolyte solution respectively and the diffused layer capacitance is as follows (equation A.2)

$$C_S^D = \frac{\varepsilon_0 \varepsilon_r}{\lambda_D}\left(1 + \frac{\lambda_D}{R_0}\right)\dots\dots\dots\dots\dots(A.2)$$

λ_D= Debye length for symmetric electrolytes, defined as $\lambda_D = (\varepsilon_0\varepsilon_r K_B T/2e^2 z^2 N_A c_\infty)^{1/2}$ where, K_B= Boltzmann constant, N_A= Avogadro's number, c_∞= molar concentration of ions.

Then, $\frac{\lambda_D}{R_0} \ll 1$ so equation A.2 reduces to $C_S^D = \frac{\varepsilon_0\varepsilon_r}{\lambda_D}$ and capacitance value is of the order of few μF/cm^2.

In this appendix, electrical property of EDL-FET using Tungsten Oxide (WO₃) channel has been analyzed. WO₃ is a 5d^0 indirect band gap semiconductor. It has been widely used material for electrochromic [15] and gas sensing applications [16-18]. The EDL-FET was fabricated on ZnO based nanostructures, single crystalline films and conductivity and photoconductivity measurement has been done thoroughly on those devices [4, 19]. Very recently a report on WO₃ based EDL-FET has been reported, although the response was very low compared to EDL-FET on ZnO [20].

A.2 Fabrication of EDL-FET device on WO₃ thin film

The WO₃ thin film has been deposited using PLD technique (discussed in chapter 2 Section 2.2.2), keeping substrate (Quartz) temperature at 500^{0}C. The laser fluence was kept at 2 J/cm^2. The oxygen pressure was 30 Pa, repetition rate and deposition time was 2Hz and 25 minutes, respectively. A Metal musk of dimension (3mm X 1mm X 200nm) has been used to grow the thin film channel of that particular size and shape for the EDL-FET device fabrication. In Fig A.3(a) FESEM image shows that the film was nanocrystalline in nature. The device was fabricated using this channel. Thermal evaporation was performed to fabricate Chromium/Gold (Cr/Au) (10 nm/150nm) electrodes as electrical contact pads for drain (D) and source (S) contact on WO₃ thin film. Fig. A.3 (b) shows schematic diagram of the EDL-FET device. Poly (methyl methacrylate) (PMMA) was used to isolate the EDL gate from the Cr/Au contact pads as it acts as an insulator.
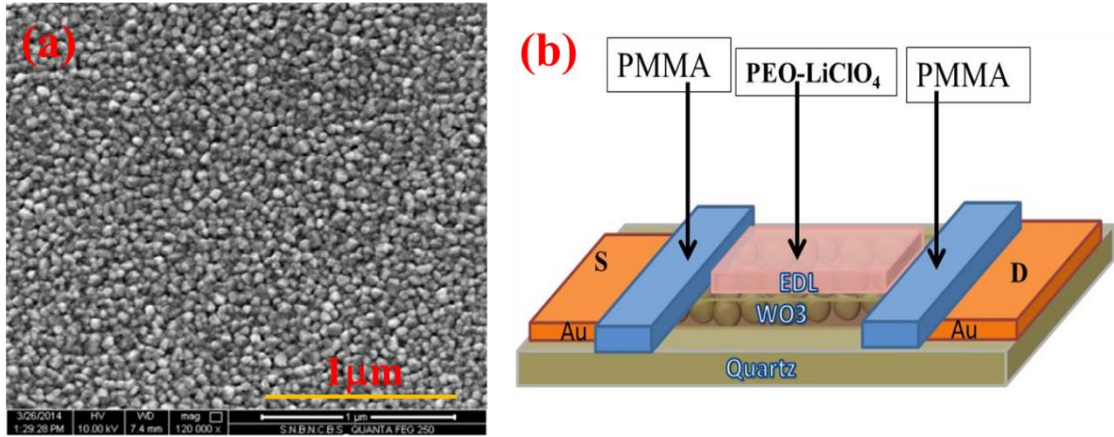
Figure A.3: (a) FESEM image of WO$_3$ thin film (b) Schematic diagram of the EDL-FET device on WO$_3$ thin film.

A.3 FET characteristics of EDL-FET on WO$_3$ thin film

The gate dependent transfer characteristic (i.e Drain source current (I$_{dS}$) as a function of gate voltage (V$_g$) at constant drain to source voltage (V$_{ds}$)) on nanocrystalline WO$_3$ channel has been studied. The gate was formed using polymer-electrolyte which makes electric double layer gate on the film. EDL was fabricated on the film using mixture of Polyethylene oxide (PEO) and Lithium perchlorate (LiClO$_4$) in 1:10 ratio in methyl alcohol. Fig. A.4 (a) shows the schematic diagram of the EDL-FET device with electrical contacts. The transfer characteristics (Fig. A.4(b)) has been measured with V$_{ds}$= 5V, V$_g$= -3 to 6V and V$_g$= 6V to -3V (reverse direction). The I$_{ds}$ increase with the increase in V$_g$ till it saturates at 3.5V with a current value of 0.75µA (Fig. A.4(b)).

The application of positive gate voltage in the electrolyte induces negative charge in the n-type WO$_3$ channel, which enhances the majority carrier density. After reaching the threshold voltage (V$_{th}$ = 1V) for the V$_g$ the I$_{ds}$ obtain its ON condition. Fig. A.5(a) shows output characteristic (I$_{ds}$-V$_{ds}$) of the device at different V$_g$. Initially, with the increase in V$_g$ the I$_{ds}$ increase. I$_{ds}$ reaches maximum value (1.2 µA) at V= 2V is compared to 0.2µA at V$_g$ = 0V. It implies that the EDL gate plays an important role to affect the conductivity of the WO$_3$ thin film channel. The drain current at higher V$_g$ is not saturated although at lower V$_g$ it was found to be saturating after 3-3.5V (Fig. A.5(a)).
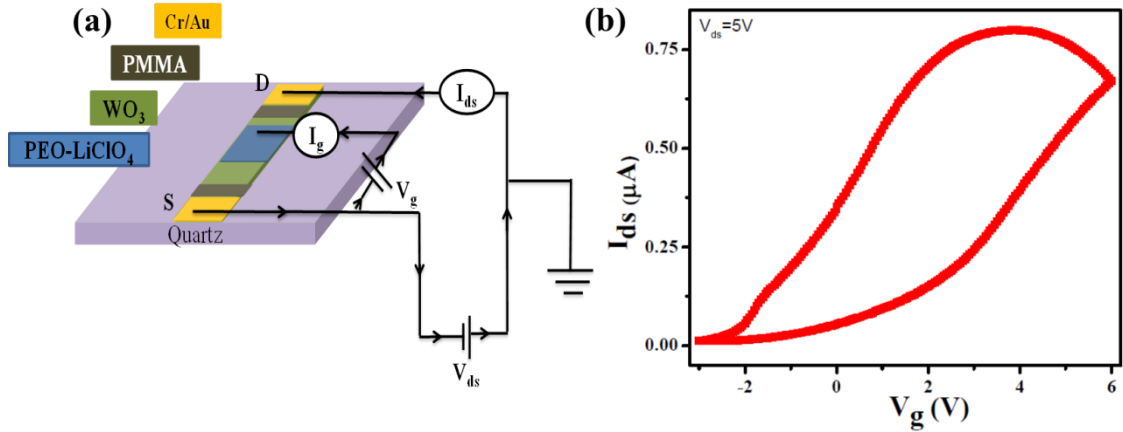
Figure A.4: *(a) Schematic diagram of EDL-FET characteristics measurement set up, (b) Transfer characteristics curve of WO$_3$ EDL-FET device.*

The EDL FET characteristics response was obtained for 1-2 times on a single device and afterwards, a sudden drop to very low I$_{ds}$ in transfer characteristics curve has been observed (Fig. A.5(b)).
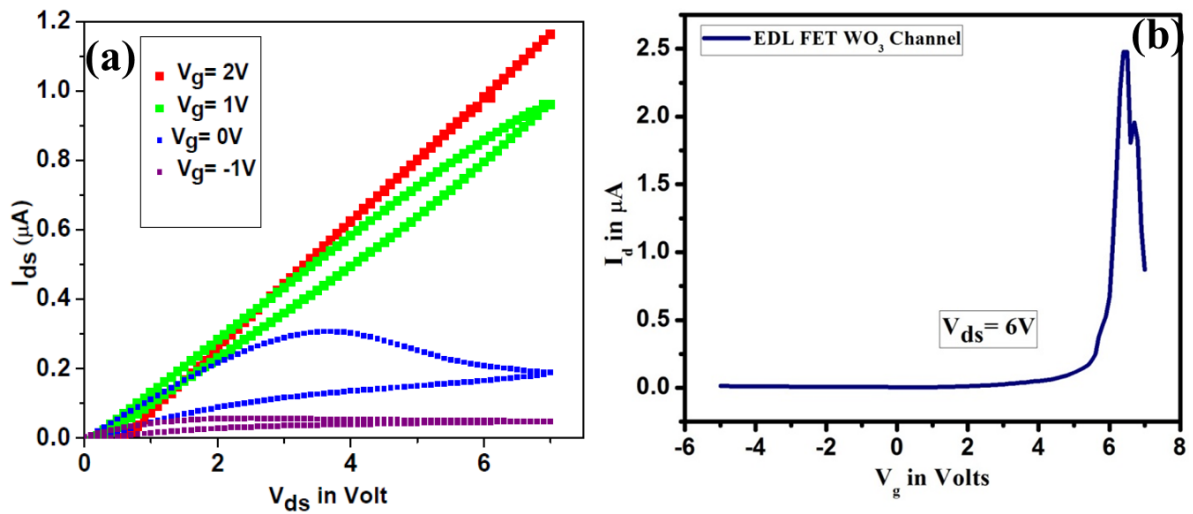
Figure A.5: *(a) Output characteristic of the EDL-FET on WO$_3$ thin film channel, (b) Transfer characteristic curve of EDL-FET device showing sudden drop in the curve during measurement.*

To understand the reason behind it the device WO$_3$ thin film channel was checked before and after the measurement in with digital camera optical zoom. It has been found that the WO$_3$ thin film with contact pad and without contact pad (Fig A.6(a, b)), after the measurement a the film was missing in between the contact pad (Fig. A.6 (c)) and found and no resistance across the channel. It suggests a reaction takes place during the measurement between EDL gate and the WO$_3$ thin film. This has been confirmed form the earlier reports where

intercalation property of WO_3 has been observed for electrochromic response [20-23]. Due this property WO_3 produces Tungsten bronze (MWO_3), where $M = H^+$, Li^+, Na^+ K^+. The typical reaction between EDL gate ($LiClO_4$) and WO_3 is as follows:

$$WO_3 + xLi^+ + xe \longrightarrow Li_xWO_3 \text{ (Lithium tungstate) } (x=0 \text{ to} 1).$$
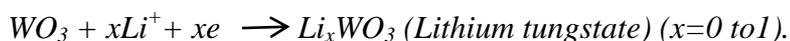
This electrochromic response of WO_3 destroys the WO_3 thin film and further no response was observed for that device.
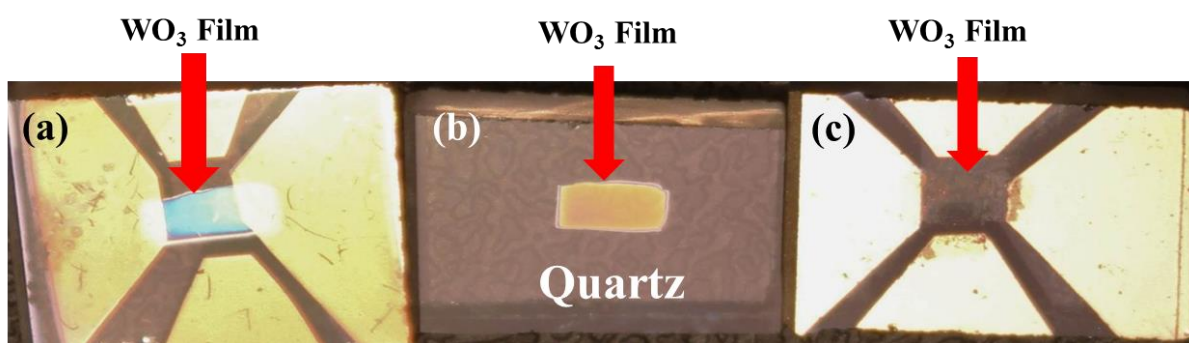
Figure A.6*: Digital camera images of (a) WO₃ film channel with electrical contact pads (Au/Cr) before measurement, (b) PLD grown WO₃ Thin film channel and (c) Damaged WO₃ thin film channel with electrical contact pads after EDL-FET measurement.*

A.4 Conclusion

EDL-FET characteristics have been investigated on WO_3 thin film grown using PLD technique on Quartz substrate. Though there was a response and increase in I_{ds} due to applied V_g but the intercalation property and electrochromic response of WO_3 thin film restricted and finally destroyed the WO_3 thin film producing Li_xWO_3. Hence EDL-FET analyis on WO_3 is not feasible with $LiClO_4$ and PEO as gate dielectric.

Bibliography

1. Y. Zhou and S. Ramanathan, Critl. Rev. Sol. Stat. and Mat. Sci., 38, 286, 2013.

2. M. Lee, J. R. Williams, S. Zhang, C. D. Frisbie, and D. Goldhaber-Gordon, Phys. Rev. Lett., 107, 256601, 2011.

3. Y. Lee, C. Clement, J. Hellerstedt, J. Kinney, L. Kinnischtzke, X. Leng, S. D. Snyder, and A. M. Goldman, Phys. Rev. Lett., 106, 136809, 2011.

4. S. Mondal, R. R. Ghimire, and A. K. Raychaudhuri, Appl. Phys. Lett., 103, 231105, 2013.

5. K. Ueno, S. Nakamura, H. Shimotani, H. T. Yuan, N. Kimura, T. Nojima, H. Aoki, Y. Iwasa, and M. Kawasaki, Nat. Nanotech.,. 6, 408, 2011.

6. H. Shimotani, H. Asanuma, A. Tsukazaki, A. Ohtomo, M. Kawasaki, and Y. Iwasa, Appl. Phys. Lett., 91, 082106, 2007.

7. A. K. Mishra, A. J. Darbandi, P. M. Leufke, R. Kruk, and H. Hahn, J. App. Phys., 113, 033913, 2013.

8. Z. Yang, Y. Zhou, and S. Ramanathan, J.Appl.Phys., 111, 014506, 2012.

9. S. Asanuma, P-H. Xiang, H. Yamada, I. H. Inoue, H. Akoh, A. Sawa, K. Ueno, H. Shimotani, H. Yuan, M. Kawasaki, and Y. Iwasa, Appl. Phys. Lett., 97, 142110, 2010.

10. P-H. Xiang, S. Asanuma, H.Yamada , I. H. Inoue, H. Sato, H. Akoh , A. Sawa, K. Ueno, H. Yuan, H. Shimotani , M. Kawasaki, and Y. Iwasa, Adv. Mater., 23, 5822, 2011.

11. Rajib Nath and A. K. Raychaudhuri, App. Phys. Lett., 104, 083515, 2014.

12. H. Yuan, H. Wang and Y. Cui, Acc. Chem. Res., 48, 81-90, 2015.

13. H. Wang and L. Pilon, J. Phys. Chem., C 115, 16711-16719, 2011.

14. R. Ghimire "Investigation Of Opto-Electronic Phenomena In Nanostructured ZnO With Electric Double Layer Gate", thesis submitted to University of Calcutta, 2016.

15. K. Thummavichai, Y. Xia, Y. Zhu, Prog. Mat. Sci., 88, 281–324, 2017.

16. S. Vallejos, P. Umek, T. Stoycheva, F. Annanouch, E. Llobet, X. Correig, et al., Adv. Funct. Mater., 23, 1313-1322, 2013.

17. S. Kim, S. Park, S. Park, C. Lee, Sens. Actu., B, 209, 180-185, 2015.

18. W. Yan, M. Hu, P. Zeng, S. Ma, M. Li, Appl. Surf. Sci., 292, 551-555, 2014

19. R. R. Ghimire, S. Mondal, A. K. Raychaudhuri, J. App. Phys., 117, 10, 105705, 2015.

20. X. Meng, F. Quenneville, F. Venne, E. Di Mauro, D. Isık, M. Barbosa, Y. Drolet, Marta M. Natile, D. Rochefort, F. Soavi, and C. Santato, J. Phys. Chem. C, 119, 37, 21732-21738, 2015

21. C. G. Granqvist, Appl. Phys. A, Mater. Sci. Process, 57, 3, 1993.

22. H. Zheng, J. Zhen Ou, M. S. Strano, R. B. Kaner, A. Mitchell, and K. Kalantar-zadeh, Adv. Funct. Mater., 21, 2175–2196, 2011.

23. A. Georg, A. Georg, U. O. Kraxovec, Thin Solid Films, 502, 246–251, 2006.